AN IMPROVED UNDERSTANDING OF THE LIFECYCLE OF MIXED-PHASE STRATIFORM CLOUDS THROUGH OBSERVATIONS AND SIMULATION

by

Gijs de Boer

A dissertation submitted in partial fulfillment
of the requirements for the degree of

Doctor of Philosophy

(Atmospheric and Oceanic Science)

at the

UNIVERSITY OF WISCONSIN - MADISON

2009

Abstract

This work explores links between ice crystal nucleation in the immersion mode and the life-cycle of mixed-phase stratiform clouds. A background discussion is included on the general properties of mixed-phase clouds, their influence on climate, observational techniques and numerical studies used to better understand these common cloud layers. Also, an overview of ice nucleation principles and Arctic aerosol characteristics is provided. An observational analysis including thousands of half hour cases of single layer mixed-phase clouds measured using remote sensors at Barrow, Alaska and Eureka, Canada is reviewed. An overview of the techniques used in this effort is provided, including information on the instruments and all implemented retrieval algorithms. These observations show distinct differences between cloud properties at the two locations, as well as clear seasonal patterns in cloud macro- and microphysical properties. This dataset is compared with those obtained in previous studies, and implications of the measurements on numerical simulation and cloud detection using other observational platforms are discussed.

Utilizing results from these observations, as well as measurements made by others, a hypothesis on ice nucleation in these clouds via immersion freezing is formed, in which the concentration of soluble aerosol mass within liquid droplets results in a freezing point depression. Subsequent growth of these droplets dilutes the concentration of soluble mass, allowing the droplet to freeze. In order to test this hypothesis, an advanced numerical model is utilized. Simulation results show that immersion freezing does contribute significantly to

ice production within mixed-phase clouds. Additionally, the soluble mass fraction assumed for the aerosol particles impacts simulated clouds via the effect discussed above. However, unlike suggested in the presented hypothesis, nucleation through the immersion mode was not limited to the regions above updrafts in the completed simulations. Instead, a combination of soluble mass fraction and temperature variations resulted in immersion freezing occurring throughout the top of the simulated cloud layer. Application of information on Arctic aerosols and ice nucleus measurements leads to a realistic simulation maintaining a mixed-phase cloud for over 16 hours. Finally, discussions on model uncertainties, future work and a summary are provided.

Acknowledgments

Drs. Gregory Tripoli and Edwin Eloranta, my mentors throughout this process, have contributed greatly to my development as a scientist. They have supported my goals and ideas, and allowed me to explore the subject matter as I saw it, providing insights and guidance along the way. The members of my PhD committee have also contributed important insight and suggestions throughout this journey. The support and guidance provided by Drs. Ralf Bennartz, Tracey Holloway, Michael Morgan, John Norman and Chris Rutland have been very much appreciated.

Collaboration with scientists both within and outside of the University of Wisconsin has contributed greatly to my development as a scientist as well as to some of the work in this dissertation. Some to be recognized in these efforts include Drs. Tempei Hashino, Hugh Morrison, Matthew Shupe, Taneil Uttal, Jennifer Kay, Steven Klein, Robert Holz, Jean-Pierre Blanchet and Eric Girard.

I would like to express gratitude to the National Science Foundation, United States Department of Energy Atmospheric Radiation Measurement program and the National Aeronautics and Space Administration for providing funding to support my work at the University of Wisconsin.

Finally, I would like to especially thank my friends and family (current and future). Their encouragement, humor and support were absolutely vital to the completion of all of this

work. I can not imagine my time spent in Wisconsin without all of the memories we have shared along the way.

Portions of this dissertation are reprinted from works previously or to be published[1] with permission of the American Meteorological Society and the American Geophysical Union (AGU).

[1] Reprinted text and figures include work from the following articles:

de Boer, G., E.W. Eloranta and M.D. Shupe, 2009: Arctic Mixed-Phase Stratiform Cloud Properties from Multiple Years of Surface-Based Measurements at Two High-Latitude Locations. Journal of Atmospheric Science, accepted for publication.

——, T. Hashino and G.J. Tripoli, 2009: A Theory for Ice Nucleation Through Immersion Freezing in Mixed-Phase Stratiform Clouds. Atmospheric Research, in review.

——, G.J. Tripoli, and E.W. Eloranta, 2008: Preliminary Comparison of CloudSAT-Derived Microphysical Quantities with Ground-Based Measurements for Mixed-Phase Cloud Research in the Arctic. J. Geophys. Res., 113, D00A06, doi:10.1029/2008JD010029.

Shupe, M.D., J.S Daniel, G. de Boer, E.W. Eloranta, P. Kollias, C.N. Long, E.P. Luke, D.D. Turner, and J. Verlinde, 2008: A Focus on Mixed-Phase Clouds: The Status of Observational Methods. Bull. Am. Met. Soc., 89, 1549-1562.

Contents

List of Figures

List of Tables

Chapter 1

Introduction

The Arctic region has experienced numerous long-term changes in climate variables, including rapid variation in temperature and sea-ice extent. Sea-ice extent has shrunk by 2.7% per decade, with larger summertime decreases (7.4%) (IPCC, 2007). These changes, along with others to the region have had a significant impact on animals, people, and the natural environment.

One of the predominant controlling forces behind the surface energy budget of the Arctic is the effect that clouds have on atmospheric radiative fluxes (Pinto, 1998; Shupe and Intrieri, 2004). Previous studies have shown low level clouds to make up over half of the annual cloud fraction. Of these clouds, many have been shown to be the mixed-phase[1], stratiform clouds commonly found at high latitude locations for extended time periods (e.g. Curry et al., 1996; Herman and Goody, 1976; Rogers et al., 2001; Shupe et al., 2006).

Recently completed modeling studies (Klein et al., 2009; Morrison et al., 2009) reveal that

[1]Mixed-phase is defined as a volume containing both liquid and ice particles, and does not include the frozen precipitation below the cloud base. The mixed-phase cloud-base is located at the lowest points containing liquid water. See Figure 3 for an example.

even state-of-the-science numerical models have difficulty replicating the delicate balance between liquid and ice in these clouds. This difficulty is due in part to a poor representation of the mixed-phase in model parameterizations, as well as difficulties with accurate prediction of ice nucleation. Nucleation rates that are too high rapidly deplete cloud liquid through the Bergeron-Findeissen process (Pruppacher and Klett, 1997) while insufficient nucleation will result in a thick liquid layer that is not representative of the observed mixed-phase state. Long-term data sets of liquid and ice properties are helpful to development of these parameterizations.

The goal of this work is to derive an improved understanding of the formation and maintenance of mixed-phase clouds utilizing information from recent Arctic observations, along with high-resolution numerical simulations. Along with observational and modeling results, a theory on ice nucleation through immersion freezing is presented as an important contribution to ice production in these cloud layers.

Chapter 2 presents an overview of the current state of knowledge on low-level mixed-phase Arctic clouds. Included is information on cloud formation and lifetime, climatological importance, measurement capabilities and simulation of the mixed-phase. Chapter 3 presents a description of instruments utilized in gathering measurements for the present study. Chapter 4 presents cloud macro- and microphysical properties as determined from multiple years of observations. Information from Chapter 4 is utilized in combination with results from other studies in the development of a theory for immersion freezing as a primary nucleation mechanism in mixed-phase clouds in the Arctic. This theory is outlined in Chapter 5. In Chapter 6, simulation results, including a numerical sensitivity study investigating the effects of aerosol properties on the immersion freezing process, are reviewed. Finally, Chapter 7 summarizes this document and provides insight into future research pathways.

Chapter 2

Background

2.1 Stratiform mixed-phase clouds in the Arctic

2.1.1 General structure and dynamics

Low-level mixed-phase stratiform clouds contribute significantly to the radiative budget of the Arctic, potentially reducing wintertime net surface cooling by 40-50 Wm-2 (Curry et al., 1996). Herman and Goody (1976), as well as Curry et al. present summaries of cloud climatologies that show low altitude stratus frequency in the Arctic of up to 70% during transitional seasons. High-latitude observations from the Mixed-Phase Arctic Clouds Experiment (MPACE, Verlinde et al., 2007), the Surface Heat Budget of the Arctic experiment (SHEBA, Uttal et al., 2002) and from observations made in Eureka, Canada (de Boer et al., 2009a) reveal long-lived mixed-phase layers, with continuous cloud-coverage lasting up to several days at a time.

These clouds are characterized by a relatively thin (100s of meters) layer of liquid. Within

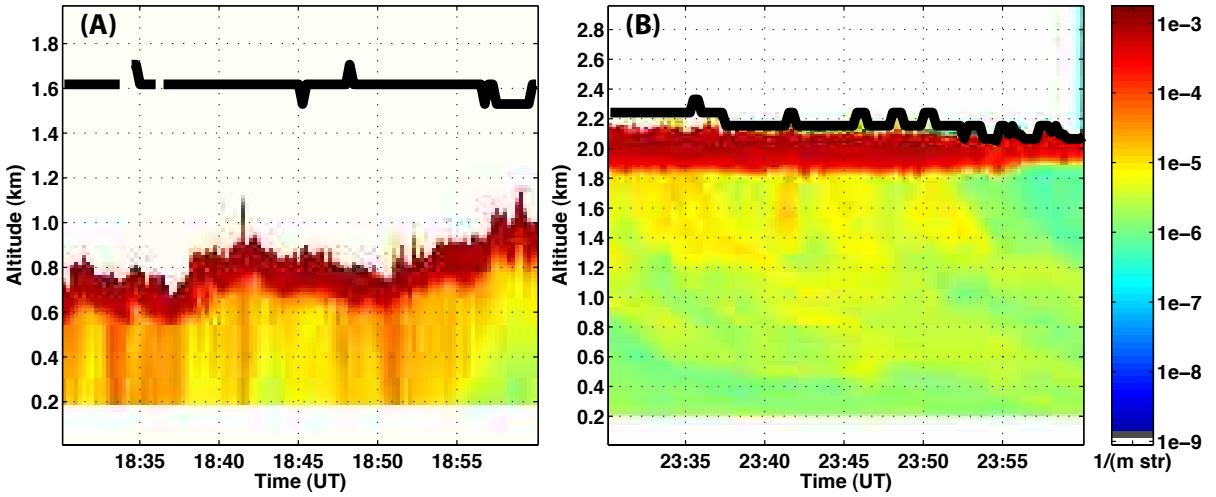

Figure 2.1: Examples of mixed-phase stratiform clouds from Barrow (A), and Eureka (B) as seen with the Arctic High Spectral Resolution Lidar (AHSRL). Cloud top as detected by the cloud radar is indicated by the bold black line. The Barrow cloud is representative of the cold air outbreak variety of mixed-phase cloud, while the Eureka case is representative of the cloud-top cooling driven variety.

this liquid layer, ice particles nucleate and grow to a size at which they precipitate out of the mixed-phase cloud layer. Figure 2.1 shows examples of these cloud layers as observed using the University of Wisconsin Arctic High Spectral Resolution Lidar (AHSRL).

Formation of these layers has generally been explained through two mechanisms. The first involves a moist air layer advecting from a moisture source or from lower latitudes over a cold Arctic surface, such as snow pack or sea-ice. This layer is subsequently cooled radiatively to the point of saturation, at which point cloud droplets nucleate on present cloud condensation nuclei. Once the liquid layer forms, it too radiates to space, and the layer near cloud top is cooled. This creates a local instability, and induces circulations of vertical motion within the layer, with cold air sinking below relatively warmer air underneath it. As will be discussed later, ice mass is found mainly within these updrafts.

The second production mechanism for these stratiform layers occurs over open ocean. In

this scenario, cold air flows off of the sea ice pack or snow-covered surface out over open ocean. The relatively warmer ocean surface provides large fluxes of both moisture and heat, and an unstable boundary layer is formed. Cloud streets, similar to those observed over the Great Lakes during cold-air outbreaks, form at the boundary layer top in regions of upward vertical motion. These clouds are typically thicker and lower in altitude than those maintained predominantly through cloud-top radiative cooling. Additionally, they usually exhibit significantly more variation in cloud-base height and cloud thickness (Figure 2.1).

2.1.2 Effect on climate

Low-level stratiform clouds have substantial impacts on the radiative budget of the Arctic atmosphere. During summer, they reflect solar radiation back to space, preventing it from reaching the surface. At the same time, they act as an insulator, absorbing and re-emitting long wave radiation emitted from the surface. A simplified overview of some of the radiative impacts of these clouds is illustrated in Figure 2.2.

One area in which these cloud effects on atmospheric radiative budget could have significant climatic impacts lies in the changes that these variations impose on sea ice formation and decay. Kay et al. (2008) outline contributions of cloud and radiation anomalies to record sea ice loss witnessed during the 2007 melt season. In that work, reduced cloudiness due to anomalously strong anticyclonic circulation and the associated increase in downwelling shortwave radiation were determined to play important roles in production of the record sea ice minimum.

The feedback mechanisms between low level clouds and sea ice are complicated, and worthy of an entirely separate study. Some examples of these interactions include:

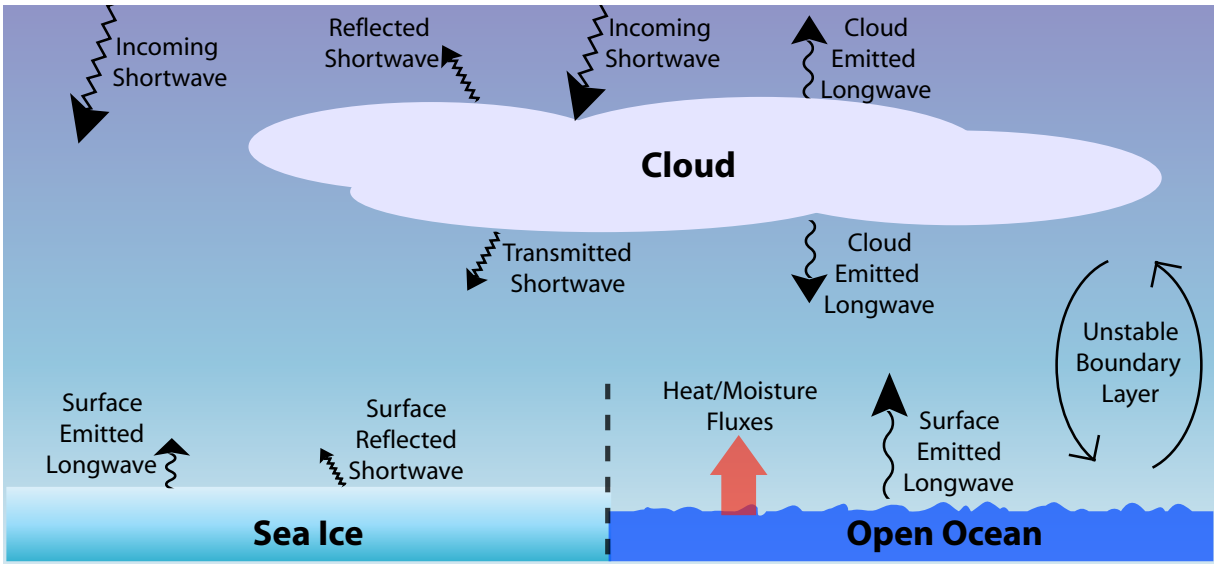

Figure 2.2: A simplified diagram of different modes of interaction between low clouds and ocean/ice surfaces in the Arctic.

- Increases in cloud cover during periods of reduced sea ice due to increased moisture fluxes from the ocean surface
- Increases in cloud cover during periods of reduced sea ice due to a destabilization of the boundary layer because of the presence of the relatively warm ocean surface
- Increases in cloud cover during periods of increased sea ice due to a increased likelihood of cold-air outbreak type situations with air flowing off of the sea-ice and over open ocean
- Increases in cloud cover during periods of decreased sea ice due to greater availability of cloud condensation nuclei through oceanic dimethyl sulfide (DMS) emission
- Decreases in sea ice due to reduced radiative cooling of the surface during periods of enhanced cloud cover
- Decreases in sea ice during periods of reduced cloud cover due to a larger shortwave radiative flux at the ice surface

There are undoubtedly more mechanisms than those mentioned above. Citing these examples, it appears evident that changes in cloud cover will likely result in changes in sea ice extent, and visa versa.

2.1.3 Observations

2.1.3.1 Surface-based

Because of differences between ice and liquid particle properties, ground-based remote sensing of these cloud structures has proven difficult. Instruments operating at shorter wavelengths (e.g. lidar) are easily attenuated by the liquid layer, while longer wavelength instruments (e.g. radar) often do not have enough sensitivity to capture scattering from small liquid particles. Shupe et al. (2008b) present an overview of the current state of ground-based observational methods. The results from this work are summarized here.

Cloud macrophysical properties and cloud phase are among the more reliable measurements using ground-based remote sensing platforms. Active sensing by cloud radar and lidar instruments provide consistent measurements of properties such as cloud base and cloud top (and thereby, cloud thickness). Cloud phase is also reliably retrieved utilizing a combination of phase specific signatures from several different measurements.

Cloud microphysical characteristics are significantly more difficult to obtain from these ground-based sensors. Several different retrieval methods exist for estimating ice particle characteristics such as particle effective size, ice water content and path, and ice-particle number density. An overview of these methods is presented in Table 2.1. The radar does not suffer from significant attenuation in these clouds, and therefore senses ice properties through the entire depth a cloudy column. However, radar-only ice microphysical retrievals are largely based on empirical relationships that have been tuned to fit a specific scenario

Table 2.1: An overview of retrieval methods for mixed-phase cloud properties and the conditions under which they are applicable (Shupe et al. (2008b)).

Property	**Instrument**	**Method**	**Conditions**
Location, boundaries, thickness, persistence	Radar, lidar, ceilometer	Clothiaux et al. (2000)	All
Phase identification	Radar-lidar-MWR-radiosonde	Shupe (2007)	All
	Doppler radar spectra	Luke and Kollias (2007)	All
Ice water content/path	Radar	Shupe et al. (2006) Matrosov et al. (2002)	Ice-containing clouds
	Lidar-radar	Donovan and van Lammeren (2001)	Nonocculted, all-ice
		Wang and Sassen (2002) Hogan et al. (2003a, 2006)	cloud volumes
	AERI	Turner (2005)	τ <6, ice containing clouds
	Near-IR	Daniel et al. (2006)	SZA∼<80 °, ice-containing clouds
Ice particle size	Radar	Shupe et al. (2006)	Ice-containing clouds
	Lidar-radar	Donovan and van Lammeren (2001)	Nonocculted, all-ice
		Wang and Sassen (2002) Hogan et al. (2003a, 2006)	cloud volumes
	AERI	Turner (2005)	τ <6, ice containing clouds
Liquid water content	Radiosonde, adiabatic	Zuidema et al. (2005)	Stratiform, liquid-containing clouds
	Doppler radar spectra	Shupe and Intrieri (2004) Verlinde et al. (2007)	Mixed-phase cases with bimodal Doppler spectra
Liquid water path	MWR	Liljegren (1994) Turner et al. (2007)	Liquid-containing cloud scenes, except rain
	AERI	Turner (2005, 2007) Wang et al. (2004)	LWP <50 gm^{-2}, liquid containing clouds
	Near-IR	Daniel et al. (2006)	SZA∼<80 °, liquid-containing clouds
	Radiosonde, adiabatic	Zuidema et al. (2005)	Stratiform, liquid-containing clouds
Liquid droplet radius	AERI	Turner (2005) Turner and Holz (2005) Wang et al. (2004)	LWP <50 gm^{-2}, liquid containing clouds
	Doppler radar spectra	Shupe and Intrieri (2004) Verlinde et al. (2007)	Mixed-phase cases with bimodal Doppler spectra
Optical depth, liquid	AERI	Turner (2005)	LWP <50 gm^{-2}, liquid containing clouds
	Near-IR	Daniel et al. (2006) Portman et al. (2001)	SZA∼<80 °, liquid-containing clouds
	SW broadband	Bernard and Long (2004)	SZA∼<80 °, liquid-containing clouds
	Radiosonde, adiabatic	$\tau = 1.5LWPR^{-}1_{e}$	Stratiform, liquid-containing clouds
Optical depth, ice	AERI	Turner (2005)	τ <6, ice containing clouds
	Radar	Matrosov et al. (2003) Hogan et al. (2003b)	Ice containing clouds
Optical depth, total	Lidar AERI	Eloranta (2005) Turner (2005)	Nonocculted cloud volumes τ <6,LWP <50 gm^{-2}
Vertical velocity	Doppler radar spectra	Shupe and Intrieri (2004); Shupe et al. (2008a)	Liquid-containing cloud volumes
Turbulent dissipation rate	Radar	Shupe et al. (2008a)	All

(Shupe et al., 2006). This results in significant errors at times.

An alternative approach is utilization of several instruments at different wavelengths to retrieve microphysical information. This technique has been implemented using lidar and radar instruments (Donovan and van Lammeren, 2001), and is discussed more fully later in this work. This technique requires some assumptions to be made regarding the particle size distribution and particle shapes of the hydrometeors sampled, which may result in modest errors. Additionally, this technique is limited to areas sampled simultaneously by both the lidar and radar, and excludes any regions within the mixed-phase region for which the lidar has been attenuated.

Radiatively constrained ice microphysical properties can be retrieved using near-infrared (IR) wavelength instruments. Examples of this include techniques by Daniel et al. (2006), which utilize scattered sunlight between 0.9 and 1.7 μm to compute a column integrated ice water path (IWP), and Turner (2005) which uses IR windows between 800-1200 and 400-600 cm^{-1} observed by the Atmospheric Emitted Radiance Interferometer (AERI) to calculate a layer averaged ice particle size. However, as noted in Table 2.1, these methods can only be applied to specific situations.

Liquid properties are more difficult to obtain. This is because instruments that have short enough wavelengths to detect relatively small liquid droplets are easily attenuated by the large collective scattering cross-sectional area that a large number of these droplets present. On the other hand, radar measurements, which are able to capture the entire depth of the cloud column, are dominated by larger ice crystals. Because of this limitation, the best estimate of mixed-phase cloud liquid properties can currently be obtained using a scaled adiabatic LWC assumption, which can be computed using a temperature profile and radar-lidar derived cloud boundaries (Zuidema et al., 2005).

Lidar-radar combined retrievals for particle size, liquid water content and number density can be obtained for low optical depth clouds that do not attenuate the lidar, and for the regions of thicker clouds which the lidar signal is able to penetrate. Similarly, AERI measurements in IR atmospheric windows can be utilized in optically thin clouds to obtain estimates of LWP and layer averaged effective droplet size, while thicker clouds require microwave radiometer measurements and statistical or physical iterative techniques to determine LWP (Turner et al., 2007).

Cloud radiative properties such as extinction and optical depth can be determined directly using several instruments. First, the Arctic High Spectral Resolution Lidar (AHSRL) measures extinction directly for the mixed-phase volume up to optical depths approaching 5, at which point the signal is fully attenuated. Phase-separated distinction requires different instrumentation. The MMCR can estimate ice phase extinction utilizing ice particle mass-area-size and density-size relationships to relate radar measured reflectivity and extinction (Matrosov et al., 2003). Again, liquid is more difficult due to deficiencies in full column observation, but estimates can be derived using the adiabatic scaling method discussed in preceding paragraphs along with assumptions on liquid particle effective radius.

For these clouds, measured cloud liquid optical depth contributions are typically 1-2 orders of magnitude larger than ice contributions, and are therefore assumed to be the dominant contributor to layer optical depth retrievals. Estimates of liquid optical depth contributions can be obtained using broadband shortwave irradiance measurements (Bernard and Long, 2004), a combination of near-IR liquid water path and particle effective size assumptions (Daniel et al., 2006), and AERI measurements (Turner, 2005).

Finally, cloud dynamical properties such as vertical velocity can be estimated from Doppler radar spectra (Shupe et al., 2008a), based on the assumption that small liquid droplets act as tracers of vertical air motion.

2.1.3.2 Satellite-based

Polar-orbiting satellite platforms allow regular measurements of cloud properties over the Arctic, offering improved spatial coverage over remote regions, such as the expansive Arctic sea ice. As an example of the frequency of overpasses with polar-orbiting instruments, between April 1, 2006 and October 11, 2007 there were nearly 100 overpasses within 10 km of the Eureka weather station. The number of overpasses increases rapidly with increased distance from the site, with approximately 250 overpasses within 30 km and approximately 410 overpasses within 50 km of Eureka. This coverage allows for comprehensive analysis of cloud cover in the Arctic. Unfortunately, the Arctic provides unique challenges in cloud measurements for both passive and active satellite remote-sensing platforms (Kay et al., 2008).

Holz (2005) provides a summary of problems faced by passive remote sensing platforms in cloud-detection in the Arctic environment. The main contributions to these measurement deficiencies include effects of the cold surface, including a reduction in thermal contrast between surface and atmosphere as well as the related strong surface temperature inversions. Because of reduced contrast between clouds and the frozen surface, sensors using visible channels lose sensitivity. Near-IR channels can be used instead, but these also face challenges due to temperature inversions near the surface. Since a large fraction of Arctic clouds are low-level, thin, and mixed-phase, strong temperature inversions result in errors in cloud-height estimates since the cloud level may have a warmer temperature than the surface. A comparison of Moderate Resolution Imaging Spectroradiometer (MODIS) cloud detection algorithms with lidar and radar measurements show a 15-40% reduction in detected clouds using the MODIS algorithms ((Liu et al., 2004)). In addition to these problems, the lack of sunlight during the Arctic winter prevents the use of reflectance measurements.

Some of the problems with the passive techniques described above could be addressed using active remote sensors such as lidar and radar. For example, a cloud radar is easily able to detect precipitation boundaries and altitudes. The CloudSAT and CALIPSO satellites have been taking measurements from space since early 2006. CloudSAT carries the Cloud Profiling Radar (CPR), operating at 94 GHz. This instrument samples an instantaneous footprint of approximately 1.4 km x 1.1 km (along-track) at sea level, with a vertical resolution of approximately 240 m. CALIPSO carries the CALIOP lidar, operating at 532 and 1064 nm, and featuring 30-60 m vertical resolution and 333 m horizontal resolution. A preliminary analysis of the applicability of CloudSAT data to mixed-phase cloud detection and measurement was completed by de Boer et al. (2008, 2009a, hereafter DB08 and DB09a). In this work, comparisons of CloudSAT cloud detection, and cloud microphysical data products with those formulated from ground-based sensors at Eureka were carried out.

Implications of mixed-phase cloud properties on detection by satellite instruments will be discussed further later on in this work. For now, it is sufficient to state that DB09a utilized ground-based measurements to determine that approximately 10% of mixed-phase cloud cases would be missed by the CloudSAT instrument due to their low altitudes and complications with ground-clutter near the surface (lowest 1000 m). In addition, approximately 7% fell below the CloudSAT detection threshold due to the small amount of ice present.

DB08 revealed that variability between CloudSAT retrieved microphysical properties and surface-based estimates for the same cloud was determined to be significant enough to warrant careful evaluation of any apparent results that depend on these retrievals. With regard to cloud detection, the cloud scenario algorithm detected all reviewed cloud layers. Out of the five cases studied, three were determined by the cloud scenario product to be

stratocumulus, while two were labeled to be altocumulus due to their higher altitudes. Precipitation from these cloud structures was falsely identified as a part of the cloud, rather than precipitation. This incorrect assessment of cloud phase was labeled as problematic, since it is used as input for assigning a priori microphysical information to cloudy bins. Because of this issue, a combination of CloudSAT products alone makes automated detection of mixed-phase stratus very challenging.

Assessments of CloudSAT microphysical retrievals were also carried out (Figure 2.3). Concentrations of liquid droplets were approximately an order of magnitude higher than those from ground-based retrievals, and were also shown to be higher than values from previous studies of mixed-phase stratiform clouds. For ice particle concentrations, CloudSAT estimates are 1-2 orders of magnitude higher than ground-based estimates and comparison with previous studies reveals that the CloudSAT estimates are outside of the range of expected values.

Generally, size estimates for liquid particles from CloudSAT were too large. Since CloudSAT likely cannot detect small particles due to its operating frequency, this is not surprising. For ice particles, sizes estimated by CloudSAT were for the most part significantly higher than those from ground-based estimates, and from comparison with previous works these CloudSAT-derived values were determined to likely be too large.

Water content retrievals performed the best of all analyzed data sets. Both for liquid and ice, there was general agreement between space- and ground-based retrievals. Although these comparisons were somewhat promising, it is important to consider scenarios in which the correct water content is derived for the wrong reasons. For example, a small number of large particles could have a similar volume as a large number of smaller particles. Since the CloudSAT product likely is not seeing the smallest liquid particles, and both number density and size are over estimated, it is possible that the water content closely resembles

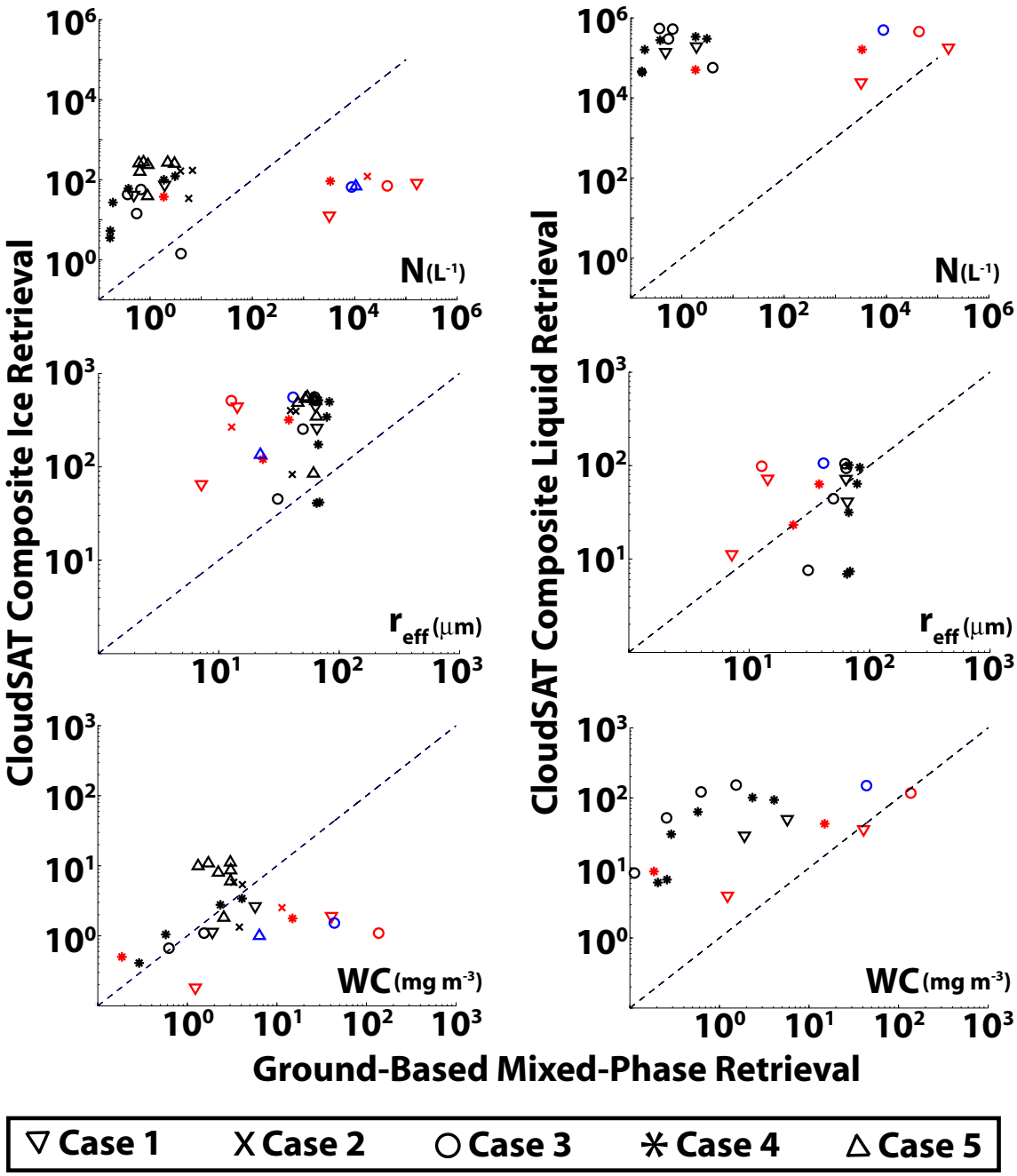

Figure 2.3: Comparisons of the ground and space-based retrievals of microphysical properties after application of the temperature-dependent partitioning scheme. The cases are separated as shown by the legend at the bottom. Additionally, the symbols have been color-coded as follows: red symbols are for comparisons of average quantities at least 50 m above the mean cloud base altitude as determined by the HSRL, black symbols are for comparisons at least 50 m below the mean cloud base, and blue symbols are for averaging intervals that fall within 50 m of cloud base.

that retrieved from the surface observations, but are not a direct result of observation of the many small liquid particles. It is difficult to say whether the algorithm was producing believable values for the correct reasons without evaluation of additional cases.

In the end, it was determined that without improvement of CloudSAT retrieval algorithms to specifically address issues found in mixed-phase clouds, current data products must be used with extreme care and scrutiny when applied to these types of situations.

Data from CALIOP can be used in conjunction with CloudSAT measurements to eliminate some of the CloudSAT deficiencies. Because the CloudSAT CPR will not be able to detect liquid associated with these mixed-phase layers, it is difficult to distinguish between thick diamond-dust layers and mixed-phase stratiform clouds. However, the liquid component of mixed-phase clouds would easily be detected using the CALIOP backscatter measurements. Unfortunately, these clouds are often layered, and upper layers attenuate CALIOP's signal, obscuring the tops of the lower cloud layers. This scene dependent behavior and applicability results in unreliable automated cloud detection with CALIPSO and CloudSAT/CALIPSO combinations.

2.1.4 Simulation

Simulation of the mixed-phase has proven difficult for all scales of atmospheric models. Early linear relationships estimating hydrometeor phase based on temperature, still in use in many climate models, have been shown to be unrealistic (e.g. de Boer et al., 2009a; Shupe et al., 2008a). Because of the scarcity of high-latitude observations, validation sources for simulations of these clouds are very limited. In addition, because we cannot yet fully characterize ice nucleation in these clouds (Fridlind et al., 2007), model inaccuracies are difficult to isolate and correct. As a result of these shortcomings, climate and weather models

have difficulty simulating the observed lifecycle and frequency of high latitude mixed-phase clouds, resulting in biases in surface radiative fluxes (e.g. Curry et al., 2000; Morrison et al., 2003). A brief overview of some efforts to do so is provided in this section.

Utilizing a two-dimensional cloud-resolving model (CRM) and information from the Beaufort Arctic Storms Experiment (BASE, Curry et al., 1997), Jiang et al. (2000) examined how variations in ice crystal concentration resulting from alterations to initial ice nucleus (IN) concentrations affect the stability and structure of low-level Arctic stratus. In order to arrive at a solution that resembled observations for the given case, a 30% IN reduction to that predicted by standard parameterizations, along with an three-fold increase in the large scale advection of heat and moisture was required. Sensitivity studies showed that decreases in IN concentrations had a large effect on structure and phase of the mixed-phase layer, thereby also affecting radiative fluxes.

Harrington and Olsson (2001) used the Regional Atmospheric Modeling System (RAMS, Pielke et al., 1992), to also investigate interactions between ice nuclei concentrations, mixed-phase cloud structure and boundary layer turbulence for clouds over the marginal ice zone. It was shown that ice crystal concentrations had significant impacts upon boundary layer turbulent kinetic energy (TKE), with decreases in TKE with increased ice concentration. Similarly, Harrington et al. (1999) noted the importance of ice crystal concentration in regulation of depositional growth and thereby indirectly, cloud-top radiative cooling through conversion of large numbers of cloud liquid water droplets to a smaller number of ice crystals.

Morrison and Pinto (2005) were able to successfully simulate a mixed-phase stratiform event utilizing a two-moment bulk microphysical scheme integrated into the polar version of the Pennsylvania State University (PSU)-National Center for Atmospheric Research (NCAR) Mesoscale Model (MM5, Bromwich et al., 2001). In this work, the authors describe

uncertainties in ice nucleation, including particle fall speeds and collection efficiencies for riming, and crystal habit which may significantly impact the proper simulation of mixed-phase stratiform cloud structures. Although a detailed sensitivity study was not included, this work brought to light many potential issues with parameterizations of ice nucleation in numerical simulations, particularly in simulations utilizing traditional bulk microphysical schemes. In addition, a need to adequately characterize sub-grid scale vertical velocity was noted, with simulations that did not do so showing weak liquid droplet activation, and thereby shorter lifetimes.

Fridlind et al. (2007) reviewed results from large eddy simulations completed at high resolution (50m horizontal, 20m vertical). These simulations utilized a bin microphysical scheme to investigate hypotheses on ice nucleation for mixed-phase clouds observed during the MPACE campaign. Numerical sensitivity experiments including several ice multiplication and nucleation mechanisms were performed, including drop shattering, ice-ice collision fragmentation, IN formation from residuals of evaporating droplets, and drop freezing during evaporation. It was concluded that measured ice nucleus concentrations were not capable of producing observed ice crystal concentrations through traditional ice formation mechanisms. However, inclusion of newly proposed ice formation mechanisms was shown to be capable of producing measured ice concentrations under IN concentrations provided by observations. The authors also acknowledge that identification of ice nucleation modes through observations remains challenging and that further development of measurement techniques is required to identify sources of presented discrepancies between model-produced ice nucleation and related observations.

Providing reinforcement to some of the above results, Klein et al. (2009) give an overview of a Global Cloud System Study (GCSS) sponsored model intercomparison designed to test abilities of different types of numerical models in simulation of single-layer mixed-phase

clouds. In this effort, simulations of seventeen single-column models (SCMs) and nine cloud-resolving models (CRMs) were compared. Simulations were based on data collected during MPACE. As with previous studies, comparison of simulation results with and without ice microphysics included resulted in the conclusion that interaction between liquid and ice phase microphysics resulted in a general under-prediction of liquid water path from the suite of models. This effort did show that models with more sophisticated microphysics generally produced more accurate predictions of liquid and ice water path.

2.1.5 Ice nucleation and the Arctic aerosol

Traditionally, four primary modes of ice formation have been discussed. These include deposition freezing, condensation freezing, immersion freezing, and contact freezing (Pruppacher and Klett, 1997). In deposition freezing, the atmosphere is required to be supersaturated with respect to ice, and water vapor is deposited directly upon the aerosol particle resulting in the nucleation of an ice crystal. In the case that water saturation has been exceeded, the condensation mode can also nucleate ice. Here, water vapor condenses upon the aerosol particle, and freezes at some point during the condensation stage. In a case where condensation occurs at temperatures above freezing, or if condensation occurs on an aerosol particle containing a large amount of soluble mass, freezing is not possible initially, and a nucleated cloud droplet is formed, containing a fraction of insoluble material which may later initiate nucleation of an ice particle through the immersion freezing mode. In this mode, the droplet experiences changes in either temperature or volume that allow it to freeze. The final primary nucleation mode is contact freezing. In this mode, free ice forming nuclei (IN) collide with existing liquid droplets and initiate droplet freezing.

In addition to the primary nucleation modes mentioned above, there are several secondary

modes of ice nucleation which may enhance crystal number densities. One of the mechanisms through which ice particles can form without IN is through the breakup of individual crystals during ice-ice collisions caused by mechanical mixing (e.g. Hobbs et al., 1972). This has generally been proposed to occur with fragile ice crystals formed at temperatures between -12 to -16 °C. A second mechanism through additional ice particles may be formed is through shattering of large droplets while freezing (e.g. Mossop et al., 1972). However, this behavior was illustrated to contribute only under conditions with droplet diameters exceeding 50 μm (Brownscombe and Thorndike, 1968). A third multiplication mechanism involves the production of ice splinters during riming of droplets onto ice particles. This mechanism, also known as the Hallett-Mossop mechanism (Hallett and Mossop, 1974), depends greatly on factors such as droplet size distribution, impact velocity, air temperature and ice surface temperature. Generally speaking, it is most active at temperatures ranging between -3 to -8 °C.

In order to assess which combination of these mechanisms may be responsible for ice formation in mixed-phase stratiform clouds, additional information describing the associated aerosols must be obtained. Investigations of Arctic aerosol properties (Bigg and Leck, 2001; Leaitch et al., 1984; Zhou et al., 2001) reveal that aerosols are often mixed in nature, consisting of both soluble and insoluble mass. Bigg and Leck (2001) hinted at coating of insoluble particles by soluble materials, usually in the form of sulfuric materials. Because of the soluble nature of material coating these aerosols, these mixed particles are able to act as a cloud condensation nuclei (CCN), despite the presence of insoluble mass. In addition, this coating deactivates the insoluble mass as potential IN (Girard et al., 2005), resulting in a theorized Arctic Dehydration feedback (Blanchet and Girard, 1994). In this feedback, the soluble coating of aerosols associated with Arctic haze prevents prevents ice nucleation, resulting in fewer ice crystals. This reduction of ice crystals leads to production of larger

ice particles through decreased competition for available water vapor, increasing water flux to the surface via precipitation.

Prenni et al. (2007) reviewed the ability of ice-nucleating aerosols to affect the seasonal climate of the Arctic, particularly through the lifecycle of mixed-phase stratiform clouds. In this work, the authors cite several reasons for difficulties in simulating Arctic clouds tied to ice nucleus concentrations. First, Arctic IN concentrations have generally been reported to be one to two orders of magnitude lower than those at lower latitudes. However, models typically utilize parameterizations based upon midlatitude IN measurements to simulate ice nucleation through primary modes (e.g. Meyers et al., 1992). Additionally, transport from mid-latitudes during the winter months results in a very strong seasonal cycle of Arctic aerosol concentration (so-called Arctic Haze), and therefore, timing of measurement campaigns affects the ability of the results to be applied universally to Arctic parameterizations.

Unfortunately, there are several limitations to measurements of IN concentrations that make true characterization of available IN extremely difficult. The instrument typically utilized in making these measurements is the continuous flow diffusion chamber (CFDC), which subjects aerosol particles to controlled temperature and humidity conditions, counting the number of particles producing ice crystals under these conditions. This instrument only captures three of the above mentioned modes of ice crystal nucleation, however, as contact freezing is not well characterized within the chamber. In addition, problems with instrument icing and a size-limiting impactor at the intake prevent full characterization of the immersion freezing mode within supercooled liquid layers. Although it is believed that the time scale required to evolve from mixed aerosol particle to nucleated liquid droplet and finally to ice crystal is shorter than the 6-8 second chamber processing time (Paul DeMott, personal communication), the inability to measure freezing ability of pre-existing

liquid droplets presents a major limitation in assessing activity of IN in ice nucleation as described above. In addition, because there is no information on the activity level of individual nucleation modes, these measurements can not be directly translated to information about how ice particles are forming within these cloud layers.

Chapter 3

Instruments

3.1 Measurement Locations

In order to better understand these cloud structures, a long-term dataset has been acquired. The study presented here utilizes multiple remote sensors operating at Barrow, Alaska and Eureka, Canada measurement stations. Barrow measurements took place between September and November of 2004, and were part of the Atmospheric Radiation Measurement (ARM) programs MPACE campaign. Eureka measurements began in August of 2005, and are ongoing at the time of writing. They are funded through the Study of Environmental Arctic Change (SEARCH), National Oceanographic and Atmospheric Administration (NOAA) Earth System Research Laboratory (ESRL) and the Canadian Network for the Detection of Atmospheric Change (CANDAC). A map showing the locations of Barrow and Eureka is shown in Figure 3.1.

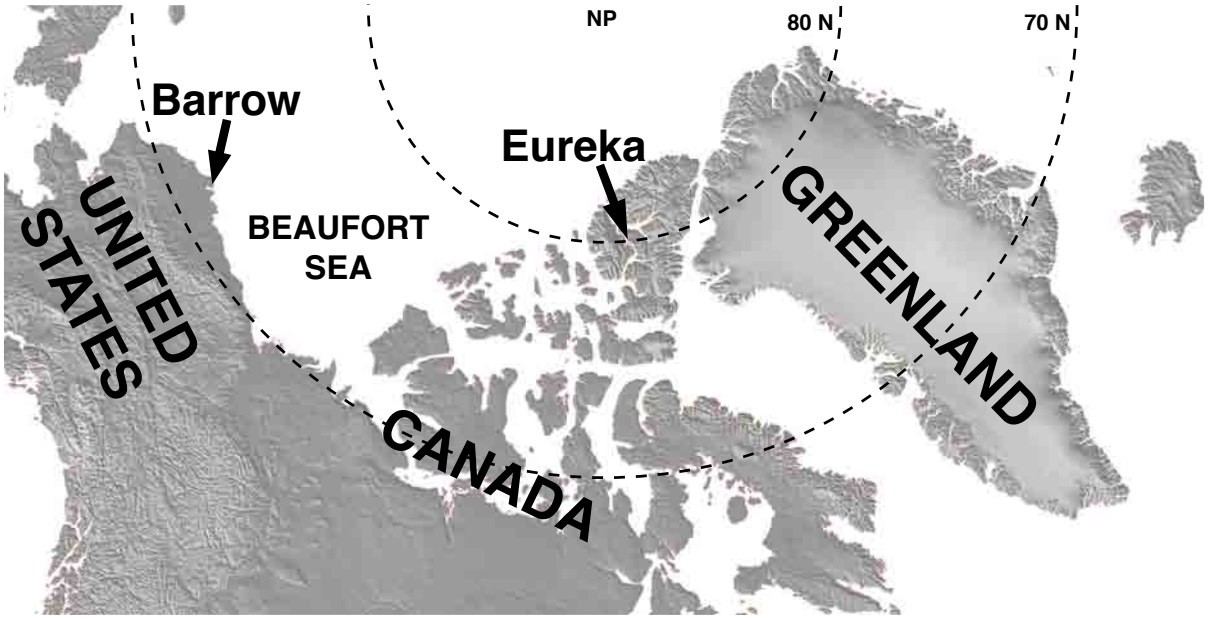

Figure 3.1: A map of the western-Arctic showing the locations of Barrow, AK and Eureka, Canada.

3.2 Arctic High Spectral Resolution Lidar

Operating at 532 nm, the Arctic High Spectral Resolution Lidar (AHSRL, Eloranta, 2005) provides profiles of backscatter cross-section, particle depolarization ratio, and optical depth. Instrument specifications for the AHSRL are in Table 3.1. Unlike traditional lidar systems, the AHSRL does not require assumptions about the ratio of backscatter to extinction. This is because the AHSRL measures two signals, which can be processed to provide profiles of both aerosol and molecular scattering. This separation can be accomplished due to Doppler broadening of the molecular return by thermal motion. Using Rayleigh theory and an independent temperature profile, the molecular scattering cross-section can be obtained. With knowledge of the molecular contribution to the scattering cross-section, absolutely calibrated aerosol measurements can be made.

The depolarization measurement made by the AHSRL is the circular particulate depolar-

Table 3.1: AHSRL (left) and MMCR (right) specifications

AHSRL			**MMCR**	
Specification	**Value**		**Specification**	**Value**
Wavelength	532 nm		Wavelength	8.6 mm
Laser Pulse Width	40 ns		Sensitivity	-50 dBZ
Receiver Field of View	45 μrad		Transmit Power	100 W (peak)
Reciever Aperture	40 cm		Receiver Aperture	1.8 m
Altitude Resolution	7.5 m		Altitude Resolution	45 m
Temporal Resolution	2.5 s			

ization. Spherical particles cause very little depolarization of the lidar signal, while particles with highly varying dimensions cause greater depolarization. Therefore, this measurement allows for discrimination between liquid particles, which are typically spherical, and ice particles, which are rarely spherical.

The AHSRL has been built for continuous unattended operation in remote locations. This allows for the collection of an extended data set in high-latitude locations. The only requirements for operation are power (120V, 30A), some form of internet access for communication and data transfer, and a temperature controlled housing with ceiling- mounted, heated and sloped window.

3.3 Millimeter Cloud Radar

The Millimeter Cloud Radars (MMCR) utilized in this research operate at 35 GHz (8 mm). They provide profiles of reflectivity, and particle Doppler velocity. The Doppler velocity measurement can be utilized to obtain information about particle fall speeds, and spectra of this measurement can be used to estimate vertical air motion (Shupe et al., 2008a). This instrument features very high sensitivity, detecting signals up to -50 dBz. The radar can be run under four different operating modes: Stratus, Cirrus, General and Precipitation.

The Barrow radar alternates between these modes every two seconds, and heavily utilizes the stratus mode in order to focus on boundary layer processes. The mode sequence for this site is:

BL GE BL CI BL GE BL PR

where BL is the Stratus mode, GE is the General Mode, CI is the Cirrus mode and PR is the precipitation mode (Widener and Johnson, 2005). The Instrument specifications for the MMCRs are provided in Table 3.1.

3.4 Combined Retrieval Algorithms

Because the AHSRL and MMCR operate at very different wavelengths, they respond to different hydrometeor properties. The AHSRL is sensitive to cross-sectional area of sampled particles. Therefore, regardless of size, high numbers of particles (i.e. liquid cloud) cause a high backscatter cross-section. The MMCR is sensitive to particle volume squared. Therefore it is very sensitive to large particles, which are typically ice crystals. These contrasting wavelengths complement each other nicely in measuring a mixed-phase environment. The AHSRL also provides a measurement of depolarization ratio. Spherical particles such as liquid droplets result in low depolarization ratios, while non-spherical particles such as ice crystals produce higher depolarization ratios. Information from an on-site microwave radiometer and twice-daily radiosonde launches from Barrow and Eureka weather stations is also utilized.

Figure 3.2 shows combined monthly uptime statistics for the two primary instruments. Since microphysical and cloud-boundary estimates could only be made for cases where

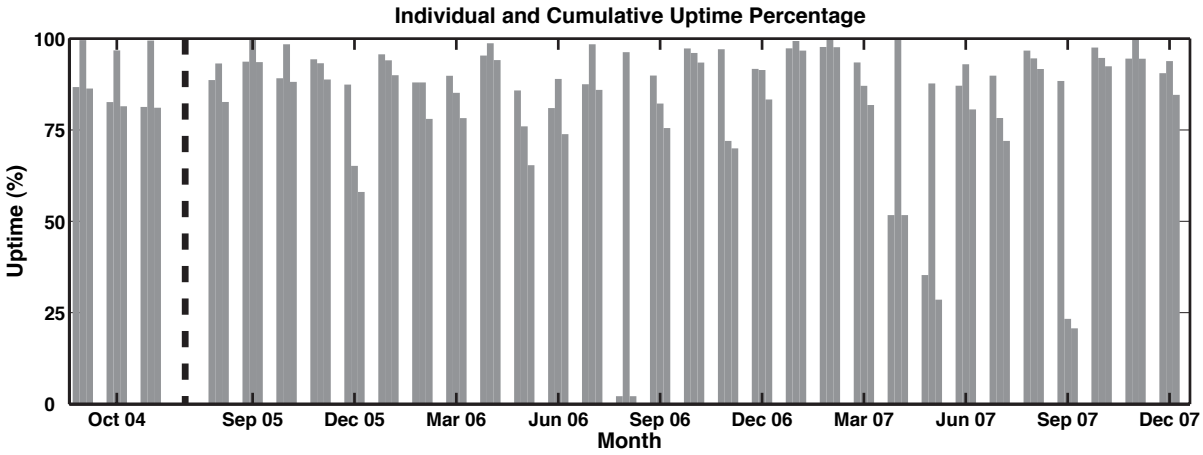

Figure 3.2: Monthly statistics of AHSRL (left bar), MMCR (center bar) and combined (right bar) uptimes from Barrow (left of the dashed line), and Eureka for each month of operation.

both instruments were operating, cases in which one of the two was not operating were removed for this study. Although most months had instrument uptimes of 80% or better, there are some clear exceptions. Most notably, August 2006 had a combined uptime of only 3%. There may be a slight bias in seasonal statistics for cloud occurrence because of these lapses in data.

Using this difference in instrument sensitivities, microphysical information is retrieved using a slightly modified version of algorithms introduced by Donovan and van Lammeren (2001). From a combination of lidar and radar backscatter cross-sections, particle effective size, particle number density, and water content are derived. Use of the AHSRL in this application has several advantages. First, AHSRL measurements are calibrated, meaning a priori assumptions about attenuation are not required. Second, although these retrievals are limited to portions of clouds in which the lidar signal is not attenuated, the AHSRL design allows penetration to optical depths near 5, allowing for deeper penetration into clouds than that provided by most other lidar systems. In short, the ratio of radar backscatter cross-section to that of the lidar results in an expression that can be solved for effective

diameter, where effective diameter is defined as:

$$D_{eff} = \frac{3\overline{V}}{2\overline{A}} \tag{3.1}$$

where $\overline{V}$ is the average volume of particles within the sampled volume, and $\overline{A}$ is the average particle cross-sectional area.

Using this technique, assumptions are required about the particle size distribution and particle shape. We assume a modified gamma distribution (Deirmendjian, 1969):

$$n(D) = aD^{\alpha}exp(-bD^{\gamma}) \tag{3.2}$$

where D is maximum particle dimension, n is number of particles per unit volume per unit length, and a, b, α and γ are size distribution parameters. Additionally, power-law relationships are assumed for particle volume and area. These relationships were modified slightly from those presented by Mitchell (1996) in order to have non-dimensional coefficients:

$$V = \sigma_v \frac{\pi}{6} D_r^{3-\delta_v} D^{\delta_v}) \tag{3.3}$$

$$A = \sigma_a \frac{\pi}{4} D_r^{2-\delta_a} D^{\delta_a}) \tag{3.4}$$

where V and A are volume and area of a particle, respectively, D_r is a habit dependent reference diameter, and D is the maximum dimension of the particle. Here, σ_v and σ_a are

the filled fraction of the volume and projected area, respectively, of a sphere with a diameter D_r. For spherical particles, $\sigma_v = 1$, $\delta_v = 3$, $\sigma_a = 1$, $\delta_a = 2$. Values of these parameters were outlined for varying particle shapes by Mitchell (1996). Since a combined distribution of liquid and ice particles is bimodal, a single gamma distribution cannot be used to represent both phases. In principle, for this retrieval method separate gamma distributions for liquid and ice could be utilized assuming contributions of each phase to measured signals could be separated. Unfortunately, this is currently not possible, and therefore any sampled volume is assumed to consist of either water or ice. Naturally, this assumption fails in mixed-phase cloud volumes, and therefore, microphysical estimates from this region should be analyzed with caution. For areas assumed to be ice, graupel is assumed as the particle type for reasons discussed in de Boer et al. (2008).

With an estimate of particle size, number density and total water content (TWC) can also be retrieved from the lidar/radar combination. In addition, a radar-only estimate of ice water content (IWC) is included. This retrieval is based on a simple reflectivity-IWC relationship:

$$IWC = aZ_e^b \tag{3.5}$$

where a and b are fixed coefficients, and Z_e is the radar reflectivity. These coefficients have been determined for clouds from SHEBA measurements, with a=0.07 (Shupe et al., 2005) and the b= 0.63 (Matrosov, 1999). Unlike combined lidar-radar retrievals, this estimate is strongly indicative of IWC because larger particles strongly dominate the radar signal.

Finally, microwave radiometer (MWR) retrievals of cloud liquid water path (LWP) are performed based on the two-stage process outlined by Turner et al. (2007). First, statistical retrievals are run relating observed downwelling radiation at approximately 23 and 30-31

GHz to LWP and precipitable water vapor using site-specific monthly retrieval coefficients derived from historic radiosonde data. These retrievals are then constrained using more accurate physical microwave retrievals that can only be performed when radiosonde temperature profiles are available (approximately twice per day). A MWR was not installed at Eureka until summer 2006, and was inoperative during much of November and December 2007. All data represented in the MWR analysis were also included in the lidar-radar analysis, however the opposite is not true.

3.5 Discussion on sources of microphysical retrieval error

As outlined in Shupe et al. (2008b) the most challenging aspect of ground-based microphysical retrievals in mixed-phase clouds is correct characterization of liquid. The lidar-radar retrieval implemented here assumes only a monomodal size distribution and is thus unable to accurately portray a mixed-phase size distribution. This limitation results in one of two situations. The first is to assume a liquid-only sampling volume despite large radar reflectivities, resulting in estimated liquid particle sizes that are too large and number densities that are too small. Conversely, if the phase is assumed to be ice, a severe overestimation of ice number density and underestimation of size results due to large lidar-measured backscatter cross-sections.

Comparisons between retrieved microphysical estimates using the above techniques, and in-situ measurements from aircraft measurements over Barrow during MPACE were presented in de Boer et al. (2008). Due to lidar attenuation, there was limited overlap between retrievals and aircraft data within liquid-containing layers. Comparisons showed that

lidar-radar retrievals overestimated liquid droplet size by approximately a factor of two due largely to the volume-squared contribution from radar-detected ice. Particle number density was underestimated by almost an order of magnitude ($10^4 L^{-1}$ vs. $10^5 L^{-1}$) because particle size is utilized in particle area estimation. Water content was also overestimated by approximately a factor of two, again, due to utilization of particle size and area in the calculation. These errors become smaller with a reduced ice amount. The following sections show significantly less ice in Eureka clouds when compared to those used in the above comparison, and therefore, liquid retrieval errors are expected to be less than those outlined above.

When looking at sub-cloud ice, assumed particle shape is the largest source for potential error. The assumed graupel crystal type resulted in the best agreement when compared with in-situ ice measurements from MPACE, with a mean size differential of <50%, mean number densities that were both on the order of 1-10 L^{-1}, and TWCs generally ranging between 0-0.1 gm^{-3}. For that particular dataset, variation of assumed particle shape resulted in effective diameter changes of up to 200 μm, number density of up to 90 L^{-1}, and TWC of up to 0.011 gm^{-3}. While some of these numbers may seem large, they are significantly reduced when only applying particle shapes resembling the irregularly shaped crystals with significant riming that have been observed in these clouds (Korolev et al., 1999; McFarquhar et al., 2007).

An additional source of error is full lidar signal extinction below cloud top for clouds with optical depths greater than 5. Thus, combined retrievals for thicker clouds do not include the upper portion of the cloud, where LWC is typically highest, introducing a bias towards underestimated cloud-mean LWC. 3.3 illustrates the extent of attenuation on the collected dataset. The bars illustrate the percentage of cases, by season, for which the lidar was able to sample 80% or more (black), 60% or more (white), 40% or more (light grey) and

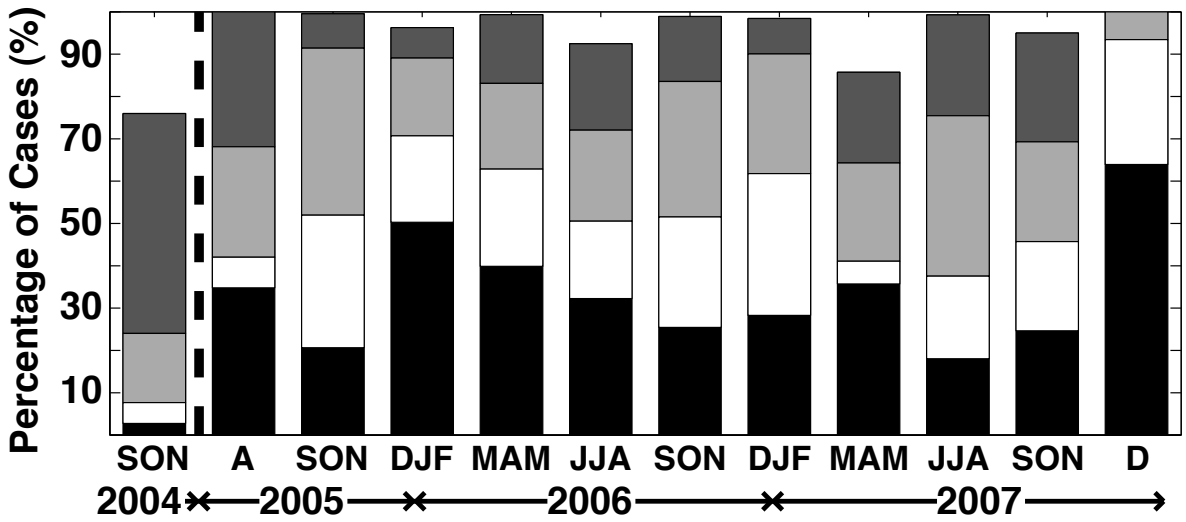

Figure 3.3: A bar graph showing the percentage of all cases (by season) in which the lidar observed 80% or more (black), 60% or more (white), 40% or more (light gray) and 20% or more (dark gray) of the total physical cloud depth before attenuation.

20% or more (dark grey) of physical cloud depth. Most clouds featured some effects due to attenuation. Winter typically had the least amount of cloud missed due to attenuation, while summer and fall had the largest amounts. As discussed later, Barrow clouds were significantly thicker than those at Eureka resulting in lidar penetration of less than 40% of the cloud vertical extent 75% of the time. In contrast, Eureka clouds featured at least 40% vertical sampling between 61-100% of the time, depending on season.

In summary, it is expected that for mixed-phase volumes, estimates of liquid droplet sizes are too large, number densities are too small and water contents are too high. Lidar attenuation is significant in the data and its impact will be discussed when appropriate in the results section.

3.6 Radiosondes

Radiosondes are launched twice daily at the Eureka and Barrow sites. These provide vertical profiles of temperature, wind and humidity information. The temperature data is utilized in the calibration of the AHSRL, and all measured properties are used to gather information on cloud thermodynamical properties. For the observational analysis, cloud boundaries are averaged over +/- 15 minutes from the launch time in order to assure representative cloud properties during a radiosonde profile. By combining these average cloud boundaries and the radiosonde profile, cloud top, cloud base, cloud minimum and cloud maximum temperatures are assigned. Additionally, surface and in-cloud wind speeds and directions are estimated.

Chapter 4

Observations

4.1 Identification of cases

AHSRL and MMCR data from MPACE and SEARCH were manually reviewed for cases featuring single-layer mixed-phase stratus. Regions were identified as mixed-phase clouds when containing high AHSRL-measured backscatter cross-section and low depolarization, while simultaneously having a measured radar reflectivity at the same altitude and high depolarization ratios below cloud base (Figure 4.1). In addition, cloud structure was considered, with only stratiform clouds (i.e. thin vertically, and continuous in nature as in Figure 4.1) included. Any half hour occurrence of mixed-phase stratiform clouds was considered to be a case. Cases showing additional cloud layers in either lidar or radar data within 1 km (vertically) of the stratiform layer were discarded. This subsetting was done to focus on single layer clouds, and to ensure removal of any seeding effects provided by nearby clouds.

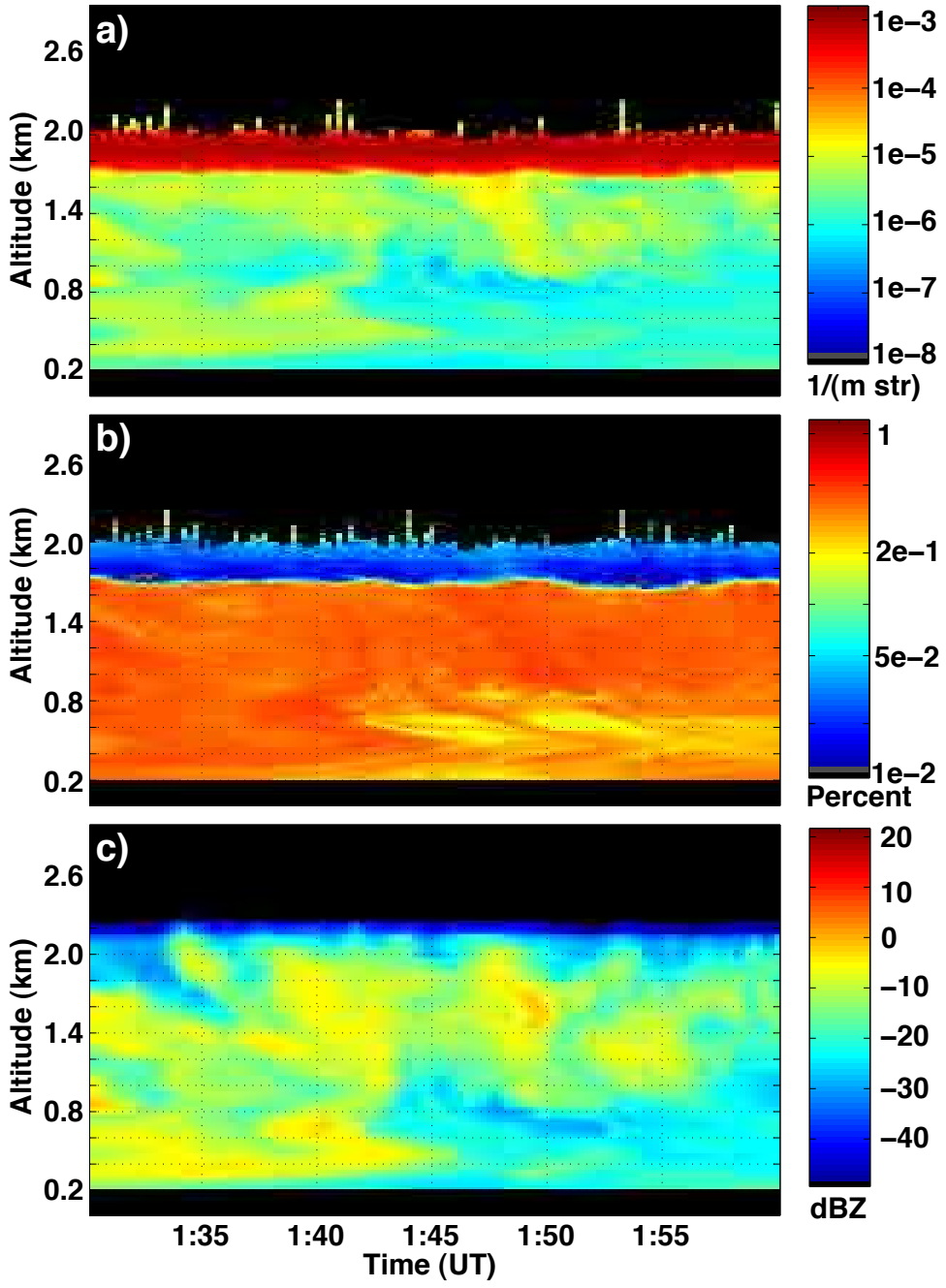

Figure 4.1: A typical 30-minute single-layer mixed-phase stratus case as observed in AHSRL backscatter cross-section (a), AHSRL depolarization (b), and MMCR reflectivity (c) on 29 December 2006. The liquid portion of the mixed-phase cloud results in high backscatter cross-section and low depolarization at 1800 m and above. Note that for this case the lidar is attenuated before reaching the top of the layer.

4.2 Estimation of cloud macrophysical properties

The first distinction made for each case was between the mixed-phase layer and frozen precipitation that occurs below it. In order to accomplish this, cloud-base is determined from AHSRL backscatter cross-section and depolarization measurements. Areas with backscatter cross-sections greater than $5x10^{-5}$ $m^{-1}str^{-1}$ and depolarization below 0.03 are determined to contain liquid. These threshold values were chosen through trial and error for cases from this data set. The first such point from the surface is determined to be cloud base for each 15-second averaging interval. Any signal below cloud base is classified as precipitation.

Cloud top is more difficult to determine because of possible AHSRL attenuation within the cloud layer. Lidar backscatter-cross-section is utilized for cases with optical depths below one. For cases with optical depths greater than one, radar reflectivity is used. Since the radar is most sensitive to larger ice crystals and likely misses small liquid droplets near cloud top, a question to address is whether the uppermost radar returns are indicative of cloud top. In-situ measurements from MPACE (McFarquhar et al., 2007) indicate that ice indeed extends throughout the mixed-phase layer to cloud top. Additionally, radar-estimated cloud-top heights were compared with those calculated from the CALIOP lidar on the CALIPSO satellite for two overpasses that occurred within 1 kilometer from Eureka. Both cases resulted in discrepancies of smaller than 30 meters, the resolution of the CALIOP instrument.

4.3 Cloud properties

Statistics presented here are for single-layer mixed-phase stratiform clouds observed at Barrow and Eureka. Each data point represents a half hour (case) average. In total, there were 532 data points from MPACE, and 2478 data points from SEARCH measurements. Combined, this data set represents over 1500 hours of single-layer mixed-phase cloud observations. Since statistics on temperature and wind required a nearly coincident radiosonde launch, these data sets are reduced significantly in size (13 for Barrow, and 110 for Eureka). Box and whisker plots illustrate the median (box center), 25^{th} and 75^{th} percentiles (box edges), and 5^{th} and 95^{th} percentiles (whisker ends) for the given season. Additionally, all values in the outer 10% of the data are represented by ovals. Seasonal mean values discussed in this work exclude outliers ($>$ 2 x IQR outside of IQR), and are shown using asterisks.

4.3.1 Cloud occurrence and macrophysical properties

Figure 4.2a illustrates frequency of occurrence of single-layer, mixed-phase clouds for each season covered by the data. This value was calculated as the number of half hour cases found in the season (number at the bottom of each bar) divided by the total number of half hour time-periods during which the radar and lidar were operating simultaneously (shown in Figure 3.2). The MPACE period of September, October and November (SON) 2004, shows a significantly higher frequency of occurrence ($\sim 26\%$) than any seasons observed at Eureka. This difference is not surprising since the Beaufort Sea (north of Barrow) is open during the fall season, providing a significant atmospheric moisture source, as well as vertical motions forced by the relatively warm water surface. Without exclusion of layered cases the frequency of mixed-phase cloud occurrence is even higher than represented here.

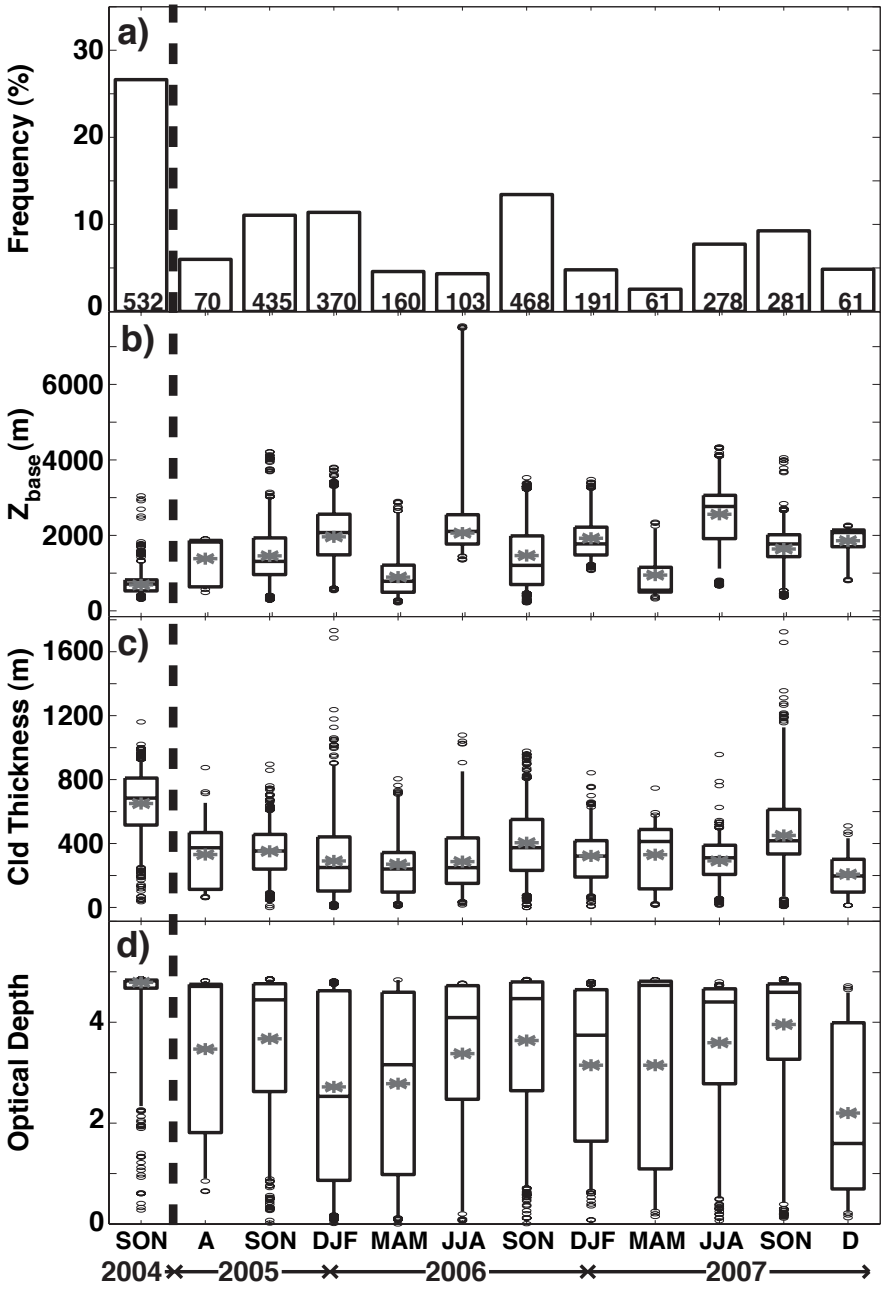

Figure 4.2: Seasonal statistics for single-layer, stratiform clouds, as observed at Barrow (2004) and Eureka (2005-2007). Indicated are frequency of occurrence (a), mean cloud base height (b), mean cloud thickness (c) and mean cloud optical depth (d). The box and whisker plots provide the 5^{th}, 25^{th}, 50^{th}, 75^{th} and 95^{th} percentiles of the 30-minute averages, as well as the mean (asterisk), and outliers (ovals).

At Eureka, fall also seems to have a more frequent occurrence of single layer mixed-phase clouds (10-15%). Interestingly, spring does have far fewer cases than other seasons (typically $< 5\%$). During summer and winter, frequencies also decrease from those observed during fall (5-8% and 5-12%, respectively). Although clouds are still present, more are entirely liquid during the summer time, and entirely glaciated during winter.

Figure 4.2b compares cloud base heights (base of cloud liquid) for different seasons. Interestingly, cloud base height appears to show an annual cycle, with heights in fall and spring being lower (means <1500 m) than those detected during summer months (means $>$ 2000 m). This makes intuitive sense, as colder temperatures necessary for mixed-phase cloud maintenance are found at higher altitudes during summer months. Interestingly, base heights associated with winter months (means $\sim =$ 2000 m) increase from those observed during transition seasons.

Figure 4.2c compares cloud thicknesses for different seasons. Seasonal mean thicknesses range from around 200-700 m, with the thinnest clouds only tens of meters thick, and the thickest around 1000 m thick on average. The thickest clouds exist during fall, and the thinnest during spring. Barrow observations show substantially thicker clouds, on average, than those observed in Eureka.

Thirty-minute average lidar cloud optical depths are reviewed in Figure 4.2d. These statistics are skewed by the AHSRLs inability to penetrate deeper than an optical depth of around 5 before suffering from attenuation. As shown in Figure 3.3, a large fraction of these clouds are thicker than this. Despite this, there are annual patterns in the optical depth data. Winter months feature clouds with the lowest optical depths (mean OD $\sim$ 2-3), while fall and summer months typically produce the thickest clouds (mean OD $\sim$ 3+). Again, Barrow clouds are optically thicker than those at Eureka.

4.3.2 Temperature and wind conditions

In order to better understand dynamic and thermodynamic atmospheric states that support development and maintenance of these single-layer clouds, temperature and wind information from radiosonde launches was analyzed. Figure 4.3 shows observed in-cloud wind direction for the cloud cases. At Barrow, winds are predominantly from the east and northeast. At Eureka, the predominant wind direction supporting mixed-phase clouds varies significantly with season. During fall, cloud-level winds are generally from the southeast. During winter, the distribution flattens out somewhat, illustrating less of a dependence on wind direction. Spring and summer months favor mixed-phase cloud formation under south-southeasterly winds.

Figure 4.4 illustrates statistics of mean cloud minimum temperatures observed for periods with mixed-phase cloud layers. The observed temperature range covers values between 242 K and 271 K. Warmer temperatures were observed during summer (mean ∼263-268 K), with the coldest temperatures observed during winter (mean ∼245 K). Transition seasons observed both at Eureka and Barrow generally featured temperatures between ∼250 K and 260 K. June, July and August (JJA) 2006 and March, April and May (MAM) 2007 had few cases during radiosonde launches.

4.3.3 Microphysical properties

Estimates of microphysical properties are divided into those retrieved from two separate regions: those from the mixed-phase layer as observed by lidar, and those from sub-cloud precipitation. Based on AHSRL depolarization measurements, precipitation is assumed to consist only of frozen hydrometeors. In-cloud lidar-radar size and number density retrievals are strongly biased towards those of the liquid due to the strong influence of the

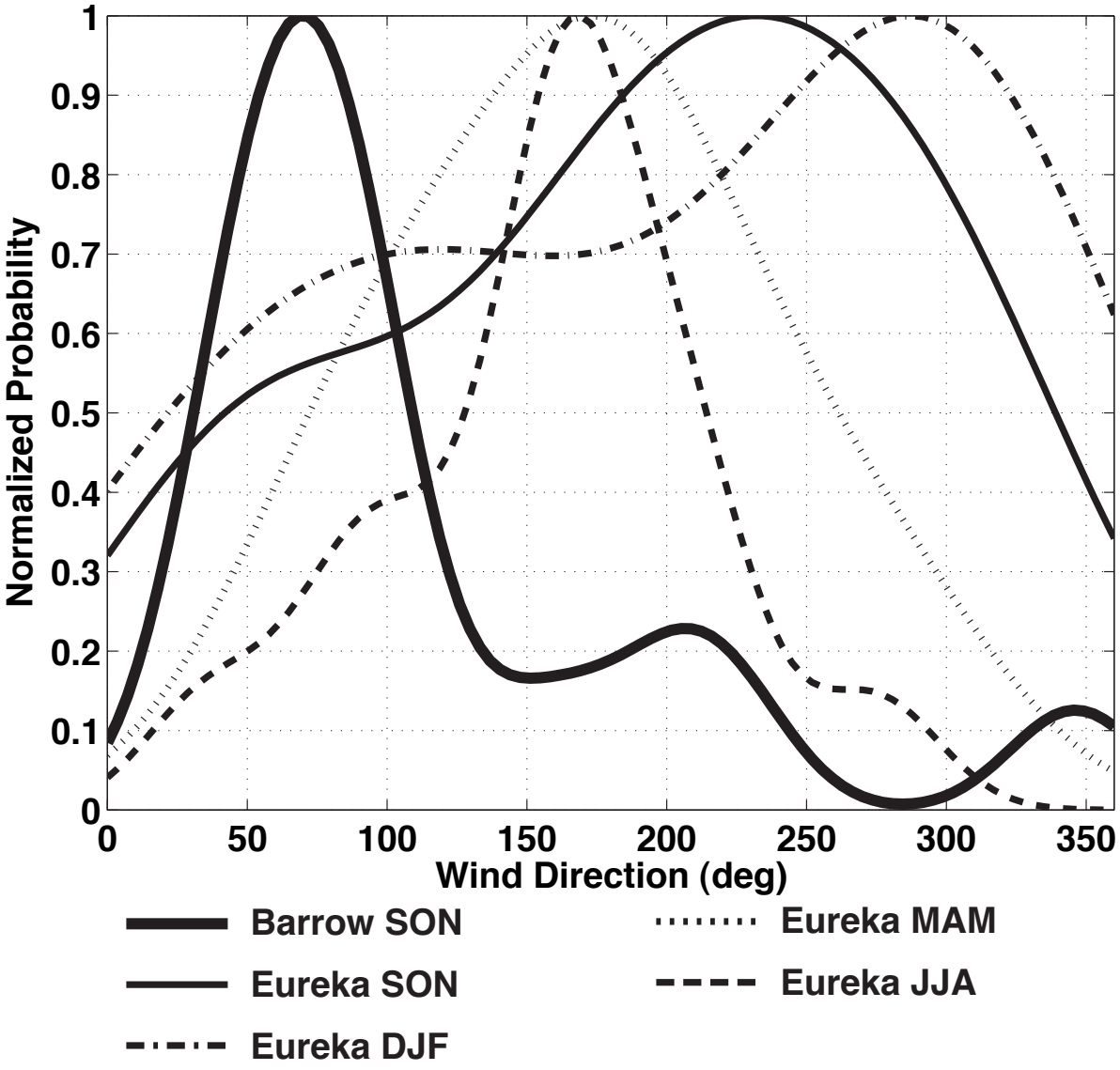

Figure 4.3: Normalized probability density functions of wind direction, separated by season and location.

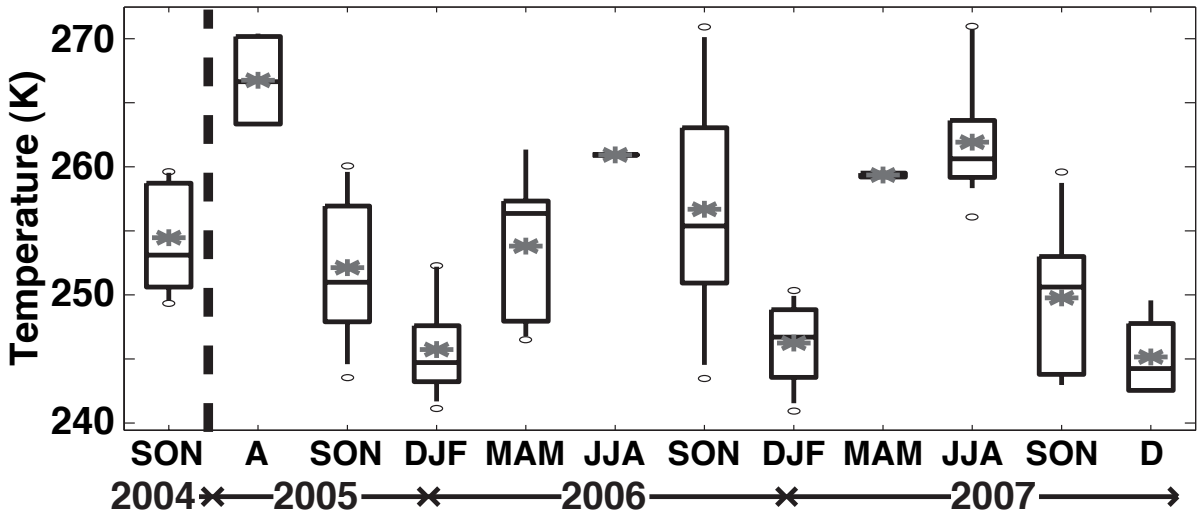

Figure 4.4: Seasonal statistics of cloud minimum temperature for single-layer mixed-phase clouds. Statistics were gathered solely for clouds observed within 15 minutes of a radiosonde launch. The box and whisker plots provide the 5^{th}, 25^{th}, 50^{th}, 75^{th} and 95^{th} percentiles of the 30-minute averages, as well as the mean (asterisk), and outliers (ovals).

liquid droplets on the lidar backscatter cross-section, and are therefore assumed to be representative of liquid. Radar-only ice retrievals are available for both regions.

Figure 4.5 shows seasonal statistics for in-cloud microphysical retrievals. The top three panels showing cloud liquid properties are most representative of lower parts of the cloud since the lidar frequently suffers from signal occultation, as shown in Figure 3.3. It is expected that drop size and LWC increase with height in the cloud (i.e. McFarquhar et al., 2007), and thus layer-averaged values may be larger than those shown here. For Eureka data, mean cloud droplet effective diameters are around 20 μm (Figure 4.5a), with slightly lower values and less variation during summer, and slightly higher values and increased variation during transition seasons (SON, MAM). Barrow data features much larger effective diameter estimates, with a mean of means around 50 μm. Because of higher radar reflectivities associated with this data, larger particles size estimates are likely due to an increase in the amount of ice contamination on the retrieval, rather than an actual increase

in droplet size of the extent shown.

Some indications of an annual cycle are evident in Eureka in-cloud mean particle number densities (Figure 4.5b), with estimates from summer months exceeding 10^5 L^{-1}, and winter-time estimates closer to $5x10^4$ L^{-1}. Notable exceptions to the seasonal cycle include MAM 2007 and SON 2006. Barrow number densities are generally lower, with the majority of data points falling below $5x10^4$ L^{-1}. All seasons reveal a relatively large spread in retrieval estimates, covering one or more orders of magnitude.

Statistics from the lidar-radar total water content (TWC) retrieval are shown in Figure 4.5c. An annual cycle also appears in this data, with higher TWC during fall, a decrease into winter, and then a slight increase into spring. Interestingly, summer months do not seem to continue this trend, with all three summer seasons featuring lower TWC. The annual mean value from Eureka is approximately 0.1 gm^{-3}, with fall typically closer to 0.15 gm^{-3} and summer closer to 0.05 gm^{-3}. Cases observed in Barrow feature higher TWC, with a mean near 0.3 gm^{-3}. With a significant portion of Barrow clouds missed due to attenuation, this is likely an underestimate. For both locations, the spread in case means is highest during fall.

In-cloud, radar only mean IWC is presented in Figure 4.5d. IWC follows a similar trend as TWC. SON typically has the highest values with mean IWC between 0.005 and 0.008 gm^{-3}. Summer is again the lowest with mean values of approximately 0.001 gm^{-3}. Data collected at Barrow feature higher IWC than those from Eureka, with a mean value of 0.037 gm^{-3}, and a wide distribution extending between $\sim$ 0-0.1 gm^{-3}.

Microphysical information on frozen precipitation below cloud base is reviewed in Figure 4.6. Effective radius estimates are naturally much higher for ice than for in-cloud liquid, with mean values typically between 50-100 μm. Differences between months fall within the

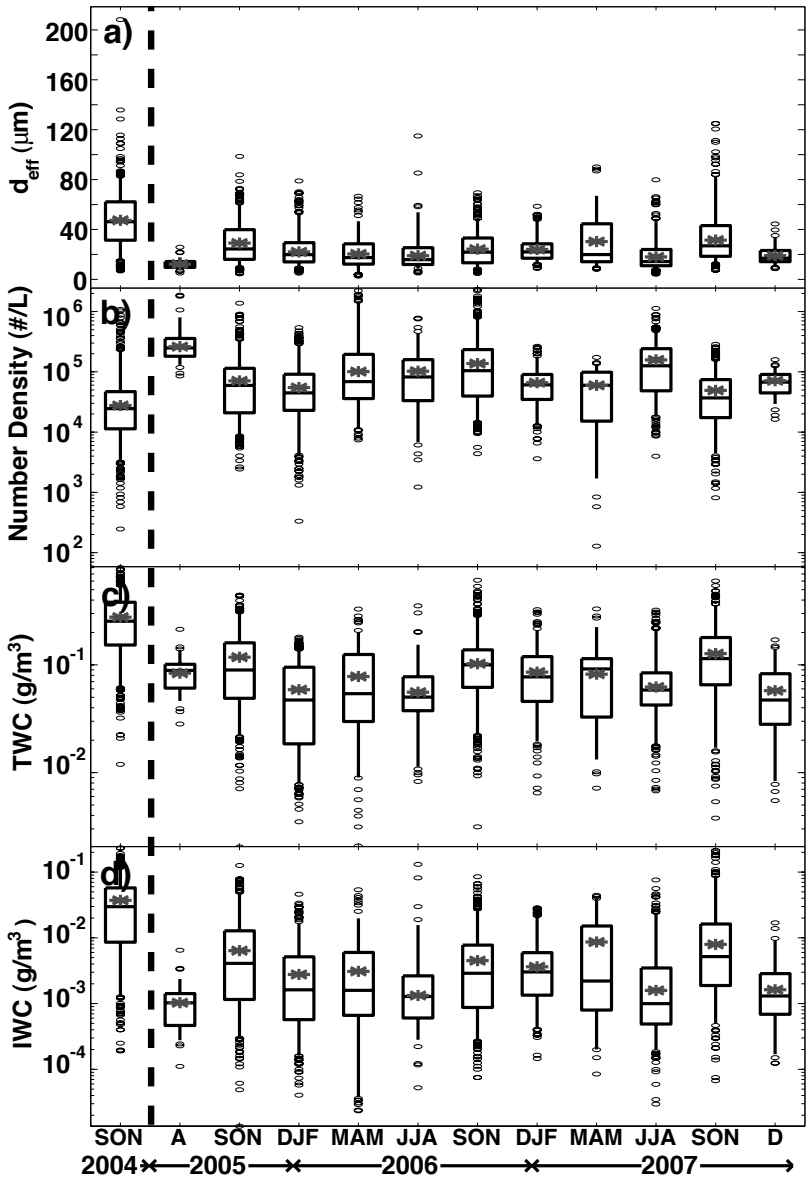

Figure 4.5: Seasonal statistics for the retrieved microphysical characteristics of single-layer, stratiform mixed-phase clouds, as observed at Barrow (2004) and Eureka (2005-2007). These values are for the region containing both liquid and ice and, with the exception of IWC, are strongly biased towards those of liquid. Indicated are lidar-radar derived estimates of mean liquid effective diameter (a), mean liquid droplet number density (b), mean total water content (c) and a radar only estimate of mean ice water content (d). The box and whisker plots provide the 5th, 25th, 50th, 75th and 95th percentiles of the 30-minute averages, as well as the mean (asterisk), and outer 10% of the data (ovals).

range of uncertainty in estimating the particle size, and therefore no significant seasonal trend is observed in the data. Ice particles observed in Barrow appear to be larger than those observed in Eureka, with the mean case average falling around 125 μm.

Because of large differences in particle concentrations between in-cloud and sub-cloud regions, even a minor miscalculation of cloud base height has significant impacts on number density statistics (Figure 4.6b). These miscalculations lead to some large outlying values. For both Barrow and Eureka, mean values for case-mean particle number density fall around 10 L^{-1}. The inter-quartile ranges (hereafter IQRs) for this data set typically range from around 1 L^{-1} to approximately 30 L^{-1}.

Without presence of cloud liquid, below cloud TWC (Figure 4.6c) is much smaller than that in-cloud (Figure 4.5c). Additionally, lidar-radar TWC estimates are very similar in magnitude to radar-only IWC estimates (Figure 4.6d), with lidar-radar estimates slightly lower. Both sets of values range from approximately 0.0001-0.05 gm^{-3} with outliers extending to around 0.15 gm^{-3}. Also, radar-only IWC estimates below cloud are slightly larger than those in cloud.

Finally, liquid water paths (LWPs) from the MWR dataset are reviewed in Figure 4.7. LWPs were largest in fall, with mean values for Eureka ranging from around 50 gm^{-2} during fall, to only around 25 gm^{-2} during winter. Fall also had the largest variation in estimated LWP, with IQRs of 15-80 gm^{-2} (as opposed to a winter IQR of 7-28 gm^{-2}). Barrow featured significantly larger LWPs, with a mean of approximately 100 gm^{-2} and an IQR of 43 to 150 gm^{-2}.

4.3.4 Vertical motion

Shupe et al. (2008a) (hereafter S08b) investigate the relationships between vertical motion

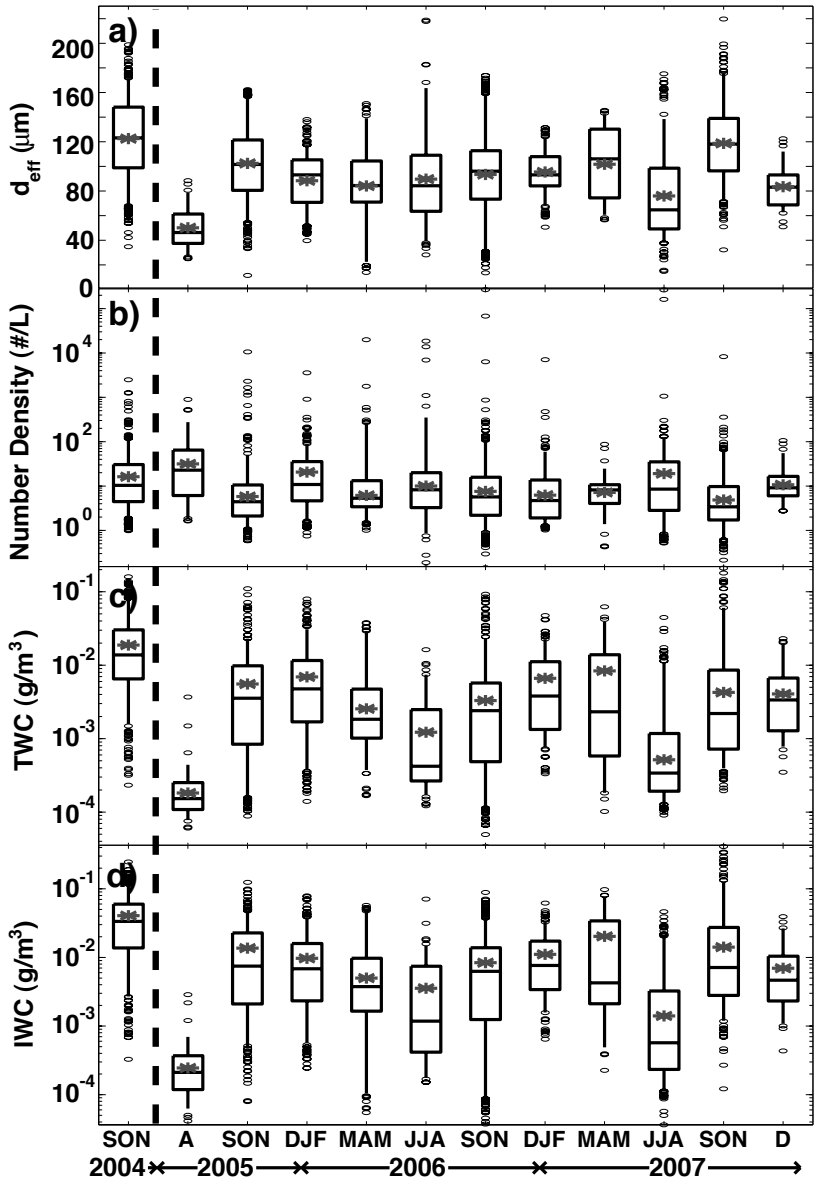

Figure 4.6: Seasonal statistics for the retrieved microphysical characteristics of frozen precipitation falling from single-layer mixed-phase clouds, as observed at Barrow (2004) and Eureka (2005-2007). These values are for the sub-cloud region containing only ice and are indicative of ice properties. Indicated are lidar-radar derived estimates of mean effective diameter (a), mean particle number density (b), mean total water content (c) and a radar only estimate of mean ice water content (d). The box and whisker plots provide the 5th, 25th, 50th, 75th and 95th percentiles of the 30-minute averages, as well as the mean (asterisk), and outer 10% of the data (ovals).

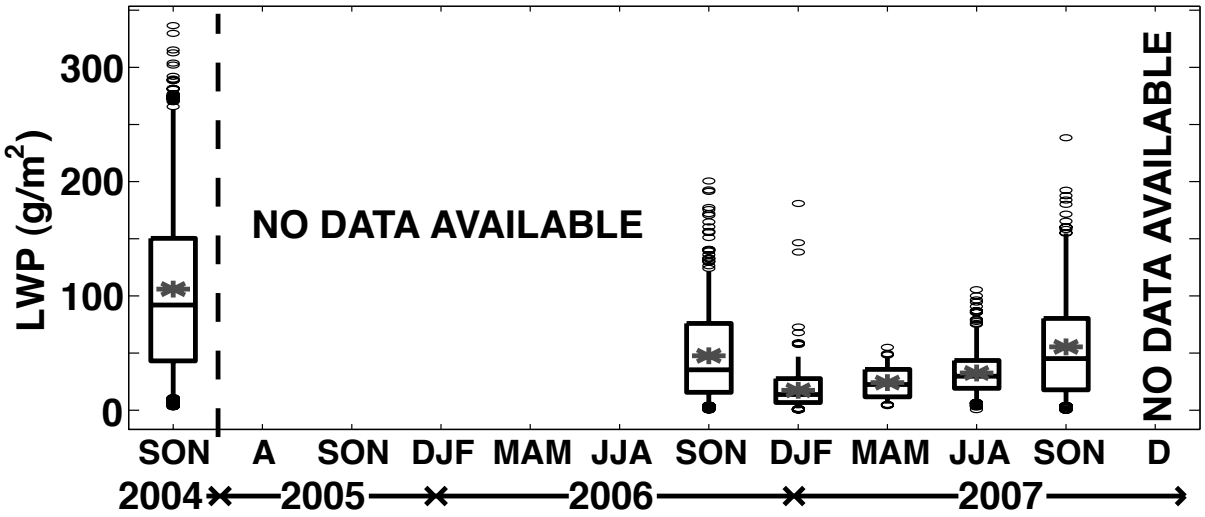

Figure 4.7: Seasonal statistics for microwave radiometer retrieved liquid water paths of single-layer mixed-phase clouds, as observed at Barrow (2004) and Eureka (2005-2007). The box and whisker plots provide the 5th, 25th, 50th, 75th and 95th percentiles of the 30-minute averages, as well as the mean (asterisk), and outer 10% of the data (ovals).

and microphysical characteristics in mixed-phase stratiform clouds in the Arctic. To complete this study, the authors utilized a combination of different instruments, including the MMCR and HSRL. The MMCR Doppler velocity spectra are used to estimate the atmospheric vertical velocity within the mixed-phase cloud layer. In order to separate air motion from the fall velocities of ice particles, the low velocity edge of the spectrum is assumed to be due to these smaller liquid particles, and the motion of these particles is assumed to be representative of the air motion (in other words, cloud liquid particle fall velocity is assumed to be negligible in comparison to the air motion).

Figure 4.8 illustrates a comparison of atmospheric motion with ice water content as estimated by the AHSRL and MMCR. Statistical comparisons between vertical motion and retrieved cloud liquid water path, ice water path, liquid fraction, hydrometeor size, cloud thickness and cloud top height were completed. Both liquid and ice water path were found to decrease with downward vertical motion, and increase within updrafts. The ice fraction

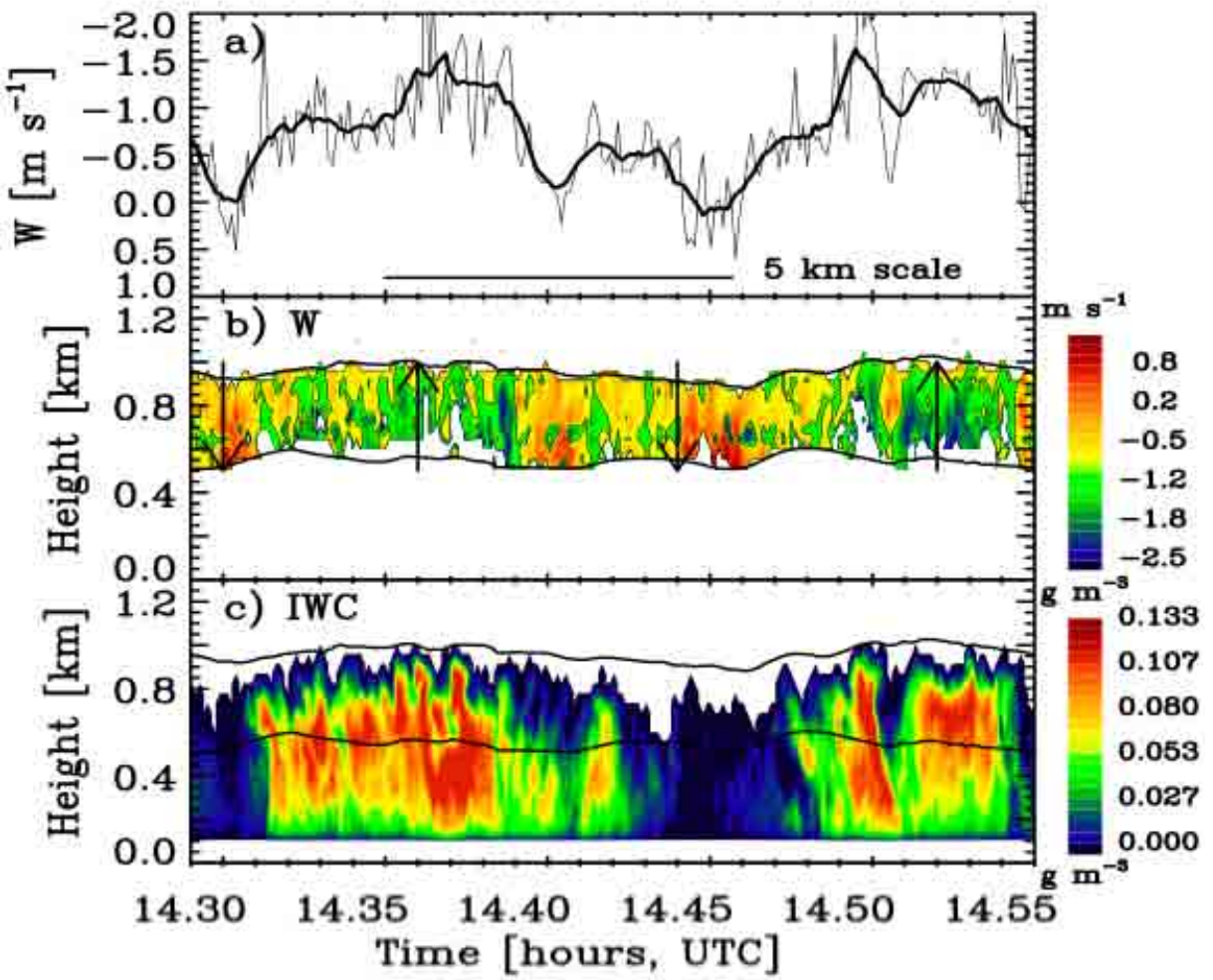

Figure 4.8: Mean (a) and height resolved (b) vertical motion in clouds from MPACE, compared with ice water content (c). (from Shupe et al., 2008b, revised).

decreased in areas of downward vertical motion, and particle effective radii were shown to decrease in these regions as well. Clouds generally were thicker and had higher cloud tops in areas of upward vertical velocity.

4.3.5 Comparison with previous observations and insights on results

Although this study constitutes one of the longest observation periods for this type of cloud, previous analysis of mixed-phase stratiform cloud properties has been done through observations of various shorter time-scales. Shupe et al. (2008a, hereafter S08) describe mixed-phase clouds observed during MPACE. In addition, Shupe et al. (2006, hereafter S06) reviewed findings from one year of observations during SHEBA, while Turner (2005, hereafter T05) and Zuidema et al. (2005, hereafter Z05) reviewed seven-month and weeklong mixed-phase stratus properties, respectively, also from SHEBA. In addition, McFarquhar et al. (2007, hereafter M07) present aircraft and ground-based measurements from MPACE. Finally, Pinto (1998, hereafter P98) presents data from the 1984 Beaufort and Arctic Storms Experiment (BASE).

Generally, comparisons to these data sets result in agreement on cloud properties. Comparing mixed-phase cloud occurrence with S06, the current study appears to have substantially lower numbers (a seasonally dependent 5-25% vs. 10-70% in S06). However, S06 was not limited to single layer or stratiform mixed-phase clouds as in the current work.

Cloud base heights derived here (mean 680-2600 m) agree well with those derived in S08 (500-800 m), S06 (200-2500 m), M07 (400-800 m), P98 (400-1100 m) and Z05 (600m). The lower values from the current observational data set came from the Barrow measurements, and are most comparable to those obtained by M07 and S08 from the same time period. Cloud thickness estimates derived here (mean 210-650 m) fall in line with those from Z05 (450 m), P98 (100-300 m), S08 (400-700 m) and M07 (500 m). However, they are less thick than those derived in S06 (1000-2500 m), because in that study the definition of cloud included both the mixed-phase layer and ice precipitation below, adding significantly to cloud

depth. Both data here and that from S06 indicate correlation between cloud thickness and season. Both show thicker clouds in late summer, fall and early winter months, and thinner clouds in late winter, spring and early summer. This may be associated with a seasonal cycle of moisture available for cloud formation. During the latter mentioned months, the ocean is covered by sea-ice, and less moisture is available to the atmosphere.

Another hint at a relationship between cloud thickness and moisture availability can be found in wind-direction estimates. Sea-ice maxima during spring reduce moisture sources to the north and east of Eureka. However, relatively warm conditions, with open ocean waters persist around southern Greenland. As mentioned previously, both spring and summer reveal a preference for mixed-phase clouds to develop under southerly wind directions.

Cloud optical depths (ODs) were reviewed in T05, with derived values ranging from 0 to 6 (limit for instrumentation). Within this distribution, there appears to be a relatively flat distribution of occurrences between ODs of approximately 0.5 and 5, and fewer occurrences of ODs above 5. This is comparable to data from the current study, which show seasonal variation in mean OD IQRs ranging between 0.75 and 5 (again, instrument limited). Figure 3.3 reveals that most of Barrow clouds and many of those observed in Eureka were thicker than OD 5.

Temperatures observed during the current study (242-271 K) also match well with those from previous work. S06 revealed seasonal mean in-cloud temperatures ranging from ∼248-263 K. S08 found cloud top temperatures between 255-269 K for MPACE, with the majority of those values falling between 257 and 266 K. Our analysis from MPACE reveals a slightly colder range of temperatures between 250-260 K. M07 studied a significantly shorter case period than the present study, but their findings fall within the ranges covered here (257-269 K cloud-top temperature range, with the peak of the distribution around 261K).

Liquid particle effective diameters, which here had seasonally dependent mean values of 12-47 μm are slightly larger than estimates of M07 (13-27 μm, 18-22 μm means), and T05 (5-40 μm, distribution peak at 14 μm). Again, this is most likely due to the retrieval method employed sampling both liquid and ice simultaneously. Although the contribution from the ice is small, it is significant enough to bias the estimates.

Liquid droplet number density estimates vary over orders of magnitude between different studies. For example, M07 found values ranging from 10^4-10^5 L^{-1} (mean values between 2.3-7.2x10^4 L^{-1}), while Z05 reported mean values of approximately 2x10^5 L^{-1}. Both of these estimates were derived from Forward Scattering Spectrometer Probes (FSSPs). With some exceptions (August 2005, MAM 2006, SON 2006, JJA 2007), seasonal mean lidar-radar estimates are generally comparable to those from M07, but slightly lower than Z05 estimates, falling between 3x10^4-2.6x10^5 L^{-1}. Z05 measurements were made during the typically polluted Arctic spring. Interestingly, Eureka data does not show clear increases in spring liquid number densities. This is possibly due to a combination of factors, including retrieval errors, geographic location and observation frequency. First, MAM 2006 does appear to have higher liquid particle numbers than surrounding seasons. MAM 2007 does not and exhibits higher radar-derived IWC estimates. The increased ice amount would contaminate liquid retrievals as previously discussed, resulting in under prediction of liquid concentrations. In addition, the MAM 2007 sample size was small, with only 30.5 hours of observations during this three-month period. Because this limited sample size is due in part to instrument failures (Figure 3.2), it is likely that clouds were missed resulting in an unrepresentative dataset. Finally, it is speculated that Eurekas northerly location (80), and distance from Asian pollution sources limit pollution influence on cloud properties when compared to regions over the Beaufort Sea, for example.

For sub-cloud ice particle concentrations, M07 observed values between 1 and 17 L^{-1} (mean

values of 1.6-5.6 L^{-1}), comparing very well with the majority of data points from the current study. These number density comparisons are very rough, however, due to the limited number of cases covered by M07 and Z05 when compared with the multi-year dataset from Eureka.

Mean in-situ LWC estimates from M07 ranged between 0.15 and 0.19 gm^{-3}, while Z05 measured LWC to range from around 0.01 gm^{-3} near cloud base to 0.06 gm^{-3} near cloud top using the FSSP and King in-situ probes. P98 also utilized the King probe, and showed LWC to range from 0.008-0.02 gm^{-3} at cloud base to around 0.1 gm^{-3} at cloud top. Sampling mainly the bottom and center sections of clouds, lidar-radar retrieved mean LWC estimates of 0.06-0.28 gm^{-3} seem to fall in line with previous estimates. The upper end of this range occurred in Barrow cases, which match very well with M07s estimates from the same location and time period. Despite these similarities, lidar-radar retrievals did present estimates of up to 0.7 gm^{-3}, which is higher than observed in previous studies. Mean IWC estimates from M07 ranged from 0.006-0.03 gm^{-3}, typically increasing from cloud-top to cloud base, but remaining constant below cloud base. P98 and Z05 showed similar spatial distributions, with IWC estimates ranging from 0.001 to 0.06 gm^{-3} and 0.001 to 0.02 gm^{-3} respectively. All of these in-situ measurements fall within the range of retrieved values from the present dataset. S08s estimated mean IWC of 0.023 gm^{-3} for MPACE clouds is slightly lower than the currently presented estimated mean for the same time period ($\sim$0.04 gm^{-3}).

LWPs derived during SHEBA in S06 had a mean of 61 gm^{-2} and ranged from 2.2-180 gm^{-2}, while LWP derived during MPACE in S08 had a mean of 156 gm^{-2} while ranging from 27-310 gm^{-2}. Z05 presented LWP estimates ranging from near zero to 120 gm^{-2}. Generally, LWP estimates from the current work fit into the ranges presented. As discussed previously, Barrow LWPs were significantly higher, matching observations by S08. Higher mean LWP

reported in S08 is likely due to inclusion of additional cases featuring layered clouds, or during which the lidar was inoperative.

Previous studies have attempted to derive a relationship between liquid water fraction (LWF) and temperature for these clouds. This relationship would aid in proper division of phase in numerically simulated clouds. Using in-situ measurements of LWC and IWC, M07 show an average increase in LWF with decreasing temperature over a range of 257-273 K. This occurs because cloud-top is typically coldest, and has the largest LWC and smallest IWC. Unlike M07 LWF estimates, the S06 and S08 studies use vertically integrated LWP and IWP to derive LWF. S06 shows a steep decrease in LWF with decreasing temperature, with average LWFs near zero at temperatures as warm as 257 K. S08 reveals a distribution of estimates where nearly 95% of LWF values are greater than 50% due to large LWPs observed during MPACE. Unfortunately, use of vertically integrated quantities requires inclusion of subcloud ice in liquid water fraction calculations, making them less representative of the ice partition within the mixed-phase layer.

Results from the current study are shown in Figure 4.9, and are divided into cases from Barrow (stars) and Eureka (circles). Here, LWF is defined as:

$$LWF = \frac{< TWC > - < IWC >}{< TWC >} \tag{4.1}$$

where <TWC> and <IWC> are the mean lidar-radar derived water content and radar-derived ice water content within the mixed-phase region, respectively. While not defined in exactly the same manner, LWF derived here is most similar to that used in S06 and S08. Unlike in those studies, however, this approach limits LWF estimates to the mixed-phase region, and does not include ice contributions from sub-cloud precipitation. As discussed earlier, <TWC> values are likely too high within the cloud layer due to the

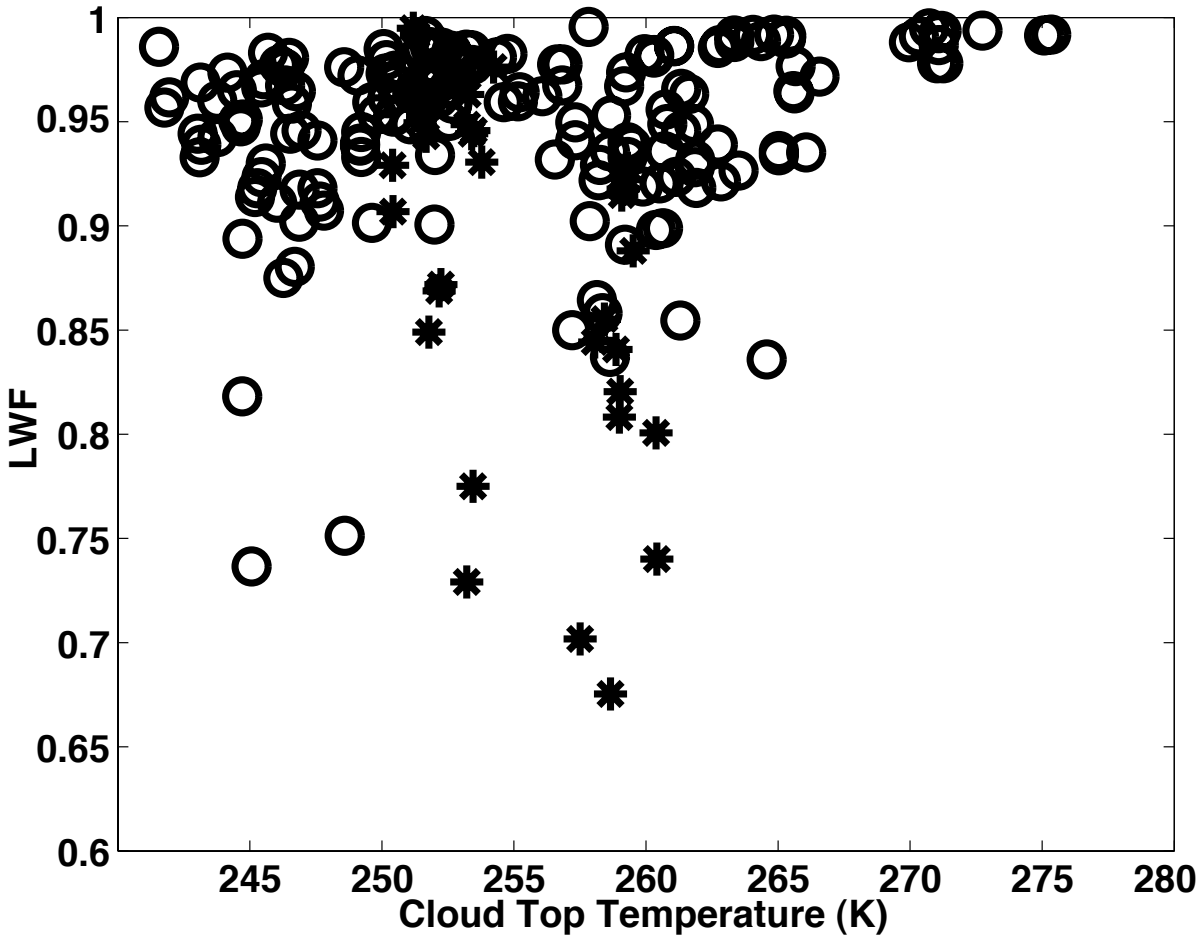

Figure 4.9: Liquid water fraction ([TWC-IWC]/TWC) versus cloud top temperature for cases observed in Barrow (stars) and Eureka (circles).

bimodal distribution of particle sizes. This causes the LWF estimate to be slightly too high. However, since <TWC> is used in both numerator and denominator, even errors in <TWC> of 50% would only result in a LWF error of ∼25%, which translated to data from this study results in changes of LWF between 0.07 and 0.22.

All cases have relatively high LWFs, with values ranging between approximately 65-100%, and the majority of values above 85%, similar to S08. Looking at the entire dataset, values higher than 85% occur across the observed temperature range (242-273 K), and there is a trend toward lower values of LWF as temperature decreases. Inclusion of points not

measured due to lidar attenuation would likely increase LWF estimates, since cloud top has greater LWC and lower IWC (M07). Based on large discrepancies between estimates of LWF from different studies, it is not surprising that parameterized phase partitioning in numerically simulated mixed-phase clouds has proven challenging.

4.3.6 Differences between Barrow and Eureka

This section briefly compares properties of clouds observed at Barrow to those observed at Eureka during fall in order to analyze location-dependent cloud characteristics. Although fall exhibits the most frequent occurrence of single-layer mixed-phase stratiform clouds at both Barrow and Eureka, they occurred nearly twice as frequently in Barrow. Barrow clouds typically have lower cloud bases, and are significantly thicker both optically and physically. The temperature range of fall mixed-phase cloud occurrence is similar for both locations ($\sim$245-260 K).

Microphysical quantities also show differences between the two locations. Barrow has significantly larger IWCs. These larger IWCs contaminate retrieved estimates of in-cloud TWC (higher), liquid number density (lower) and liquid particle effective size (larger). It is unproven that the above relationships are solely due to ice-induced retrieval errors, but comparison with in-situ observations of M07 appear to indicate that this is likely the case. Comparing sub-cloud ice number densities, retrieved properties from Barrow are very similar to those from Eureka, while ice particle size, and thereby IWC estimates are larger. These larger ice particles are not surprising, as thicker Barrow clouds would result in more time spent inside the saturated mixed-phase region for ice particles.

These observations indicate that there may be significant differences between mechanisms driving Barrow clouds versus those in Eureka. Many clouds observed at Barrow during fall

2004 resulted from a cold-air outbreak type situation, with northeast winds bringing air from the sea-ice pack over the open Beaufort Sea (Verlinde et al., 2007). The boundary layer was convective, and sea-surface heat and moisture fluxes were significant. Satellite observations from MPACE show roll structures similar to those commonly observed over the Great Lakes in fall and early winter. In contrast, many clouds in Eureka appear to form independently of the boundary layer, with cloud-top radiative cooling driving buoyancy circulations that support cloud maintenance (Herman and Goody, 1976). These eddies are not necessarily driven by surface energy fluxes, allowing Eureka clouds to be detached from local sources of buoyancy and moisture.

4.3.7 Implications for detection with CloudSAT

It is hoped that the data from this study will be used to improve detection and simulation of mixed-phase stratiform clouds. Many satellite platforms depend upon *a priori* information about clouds to aid in their detection. Properties such as cloud altitude, temperature, optical depth, and physical thickness can aid in correct detection of specific cloud types. Additionally, this information can be utilized to assess whether a particular instrument can detect these clouds at all. CloudSAT, for example, has been shown to have difficulties with mixed-phase cloud recognition and evaluation (de Boer et al., 2008). Part of this is likely due to the fact that some of these clouds do not have sufficient ice to be detected by CloudSAT. Figure 4.10 shows the seasonal mean maximum radar reflectivities detected by the MMCR in the current study. CloudSAT is able to detect to approximately 29 dBZ. Though the majority of observed clouds had mean maximum reflectivities above this threshold, there were some instances that did not. Although the MMCR and Cloud Profiling Radar (CPR) aboard CloudSAT operate at different frequencies, the differences in detected signal would be most evident at higher reflectivities (Alain Protat, personal

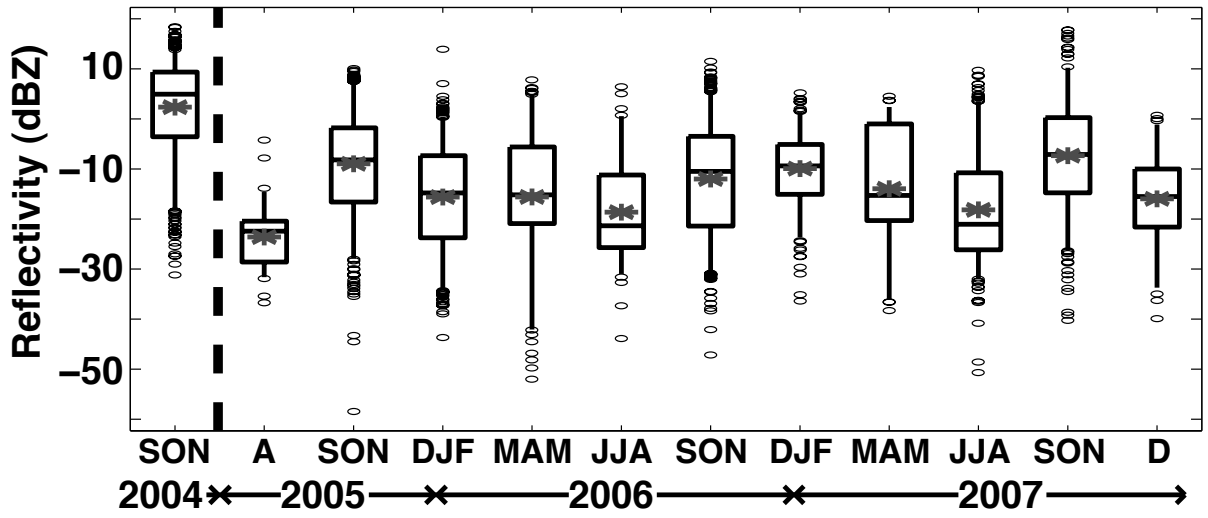

Figure 4.10: Seasonal statistics of mean maximum in-cloud radar reflectivity as measured by the MMCR for single-layer mixed-phase clouds as observed at Barrow (2004) and Eureka (2005-2007). The box and whisker plots provide the 5^{th}, 25^{th}, 50^{th}, 75^{th} and 95^{th} percentiles of the 30-minute averages, as well as the mean (asterisk), and outer 10% of the data (ovals).

communication). An additional source of complication for CloudSAT measurements comes from the low altitudes and thicknesses of these clouds. Because CloudSAT has a vertical resolution of 500 m, ground clutter is an issue for signals detected within the lowest two range gates. Of the 3012 cases analyzed in the present study, 206 had mean maximum radar reflectivities under 29 dBZ, and 316 had cloud top altitudes under 1000 m.

4.3.8 Implications for numerical modeling

In addition to advances in cloud detection and observation, information presented here can aid in the improvement of mixed-phase cloud parameterizations for numerical models. S06 gives a brief overview of model parameterizations, including temperature limits presented by Ose (1993), Del Genio et al. (1996), Tiedtke (1993), Smith (1990) and others. The lower temperature ranges for mixed-phase cloud occurrence from these parameterizations range from 233 K to 264 K. In this work, we have shown that mixed-phase clouds readily exist

at temperatures down to 240 K, and that there is a general (but not robust) decrease in liquid fraction with decreasing temperature. Additionally, cloud frequencies and altitudes presented here can be compared with results from large-scale model predictions.

Chapter 5

Theory of Immersion Freezing

In this section, a theory on nucleation of ice through the immersion freezing process within these layers is presented along with observational evidence in support of this theory (from de Boer et al., 2009b). Finally, possible implications for cloud simulation and observational techniques are discussed.

5.1 Conceptual model for immersion freezing in mixed-phase stratiform clouds

Theories on initialization of liquid cloud layers in the Arctic that ultimately result in mixed phase stratus have been described in Herman and Goody (1976). Moist layers advected over the Arctic are cooled through radiation and diffusion. Eventually, this layer reaches saturation, allowing for condensation of liquid water on available cloud condensation nuclei (CCN) (Figure 5.1, (1)). As discussed in Chapter 2, measurements of Arctic aerosols have shown them to frequently be mixed in nature, containing a high fraction of soluble mass.

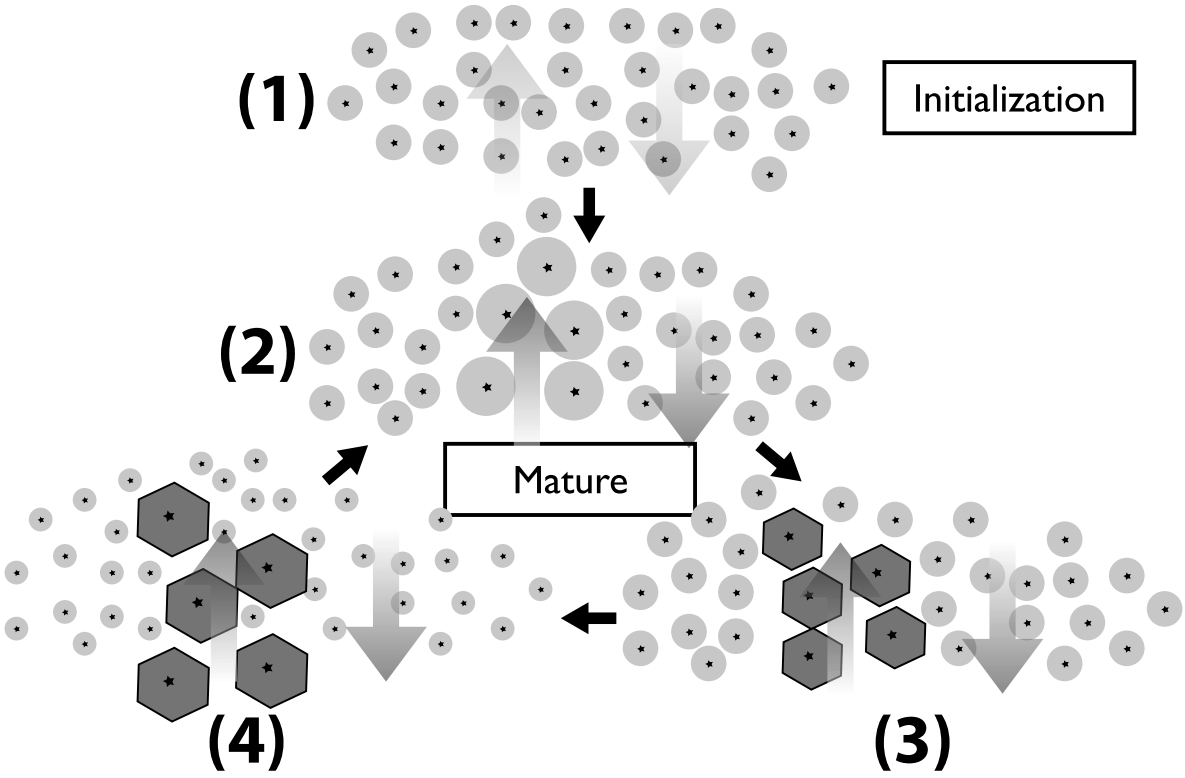

Figure 5.1: A conceptual model of immersion freezing in mixed-phase stratus. In stage 1, a liquid cloud has been formed through radiational cooling of the atmosphere. Stage 2 features a broader drop size distribution produced by the vertical motion in the cloud. In stage 3, the larger, less concentrated droplets freeze, and in stage 4, the ice crystals grow at the expense of further liquid water growth and precipitate out of the cloud layer.

This soluble mass can deactivate potential IN and prevent ice nucleation (Girard et al., 2005). This is important, since the environment will be highly supersaturated with respect to ice at the point of droplet nucleation, and nucleation of ice instead of liquid would result in an ice-only cloud. The end result is that cloud droplets formed upon these particles consist of a solution of water and soluble material, and contain some insoluble aerosol mass.

This liquid nucleation process leads to a relatively uniform layer of cloud droplets, which impart significant effects on the radiative budget of the atmospheric column. Once the liquid layer has formed, radiative cooling from cloud top initiates buoyancy-driven circula-

tions within the cloud, producing a structure consisting of eddies, maintaining the cloud in a manner similar to mid-latitude stratus decks (Paluch and Lenschow, 1991). These buoyancy driven circulations affect the microphysics of the cloud layer in that droplets grow through expansion in updrafts (Figure 5.1, (2)). Unlike in mid-latitude stratus however, drizzle is rarely observed for these mixed phase clouds, unless precipitating ice melts before reaching the ground. This implies that droplets growing in updrafts are not falling as liquid precipitation.

It is hypothesized that alteration of the size of liquid particles allows for initiation of freezing through the immersion freezing process (Figure 5.1, (3)). Besides the volume-dependant reduction in freezing point depression due to internal density fluctuations discussed in PK97, another way in which droplet growth through condensation will increase the likelihood of freezing is through dilution of the droplet solution. This reduction in concentration of soluble material reduces the freezing point depression induced by presence of soluble material within the droplet (Bertram et al., 2000). The critical concentration for effects on ice nucleation is dependent on several variables, including temperature of the drop and initial aerosol particle size and composition. However, PK97 give an approximate lower limit for the concentration of soluble material affecting droplet freezing at 10^{-3} mole L^{-1} for atmospheric salt solutions surrounding typical aerosol insolubles such as illite or kaolinite. Diehl et al. (2006) provide a slightly higher estimate of 0.05 mole kg^{-1}. Figure 5.2 illustrates the molality of droplets as a function of droplet and aerosol particle size. The initial aerosol particles used for these calculations were considered to have 70% soluble material by mass (Bigg and Leck, 2001; Zhou et al., 2001). The molality is shown in mole L^{-1}, along with the activation radius of liquid droplets at two levels of supersaturation for the given aerosol sizes (bold black lines) at -20 °C, as calculated by:

$$r_{N,c} = \left[\frac{a_c^3 (A - s_{v,w} a_c)}{A + (B - s_{v,w}) a_c} \right]^{1/3} \tag{5.1}$$

where $r_{N,c}$ is the critical radius of a dry aerosol particle, a_c is the droplet activation radius and $s_{v,w}$ is the supersaturation. A and B are coefficients as provided by PK97 (pg. 178), where A is a function of temperature.

In order for immersion freezing to be possible as described here, droplets would have to be able to activate with molalities higher than 10^{-3} moles L^{-1}. Figure 5.2 indicates that this would be possible at supersaturations between 0.1% and 1%.

Aerosol measurements by Heintzenberg et al. (2006), Engvall et al. (2008), Hegg et al. (1995) and Covert and Heintzenberg (1993) reveal Arctic aerosol particles with radii ranging from ∼0.1-0.42 μm (Figure 5.2, light grey box). Activation of a droplet on particles in this size range would result in liquid droplets of ∼2.3-8 μm (1-3.2 μm) at a supersaturation of 0.1% (1%). Liquid droplet size measurements by Zuidema et al. (2005), Pinto (1998), Hegg et al. (1995) and McFarquhar et al. (2007) show droplet radii ranging between ∼2.5-11 μm (Figure 5.2, light grey box), matching the approximate range of expected droplet sizes given the aerosol measurements. Of these observations, only the Hegg dataset (darker grey box) has measurements of both aerosol and droplet sizes from the same date and region. Unfortunately, it is difficult to measure aerosol properties inside a supercooled liquid cloud. Therefore, only ranges of the observations are presented here. The extreme lower right hand corner of the observational ranges shown (large aerosol but very small droplets) is a scenario that would only be possible at relatively high supersaturations (∼2%). Nevertheless, from the observed ranges we note that even some of the larger observed droplet sizes fall in the range required for inhibition of the freezing process due to the concentration of soluble mass within the droplet. This implies that the possibility of a contribution to the freezing

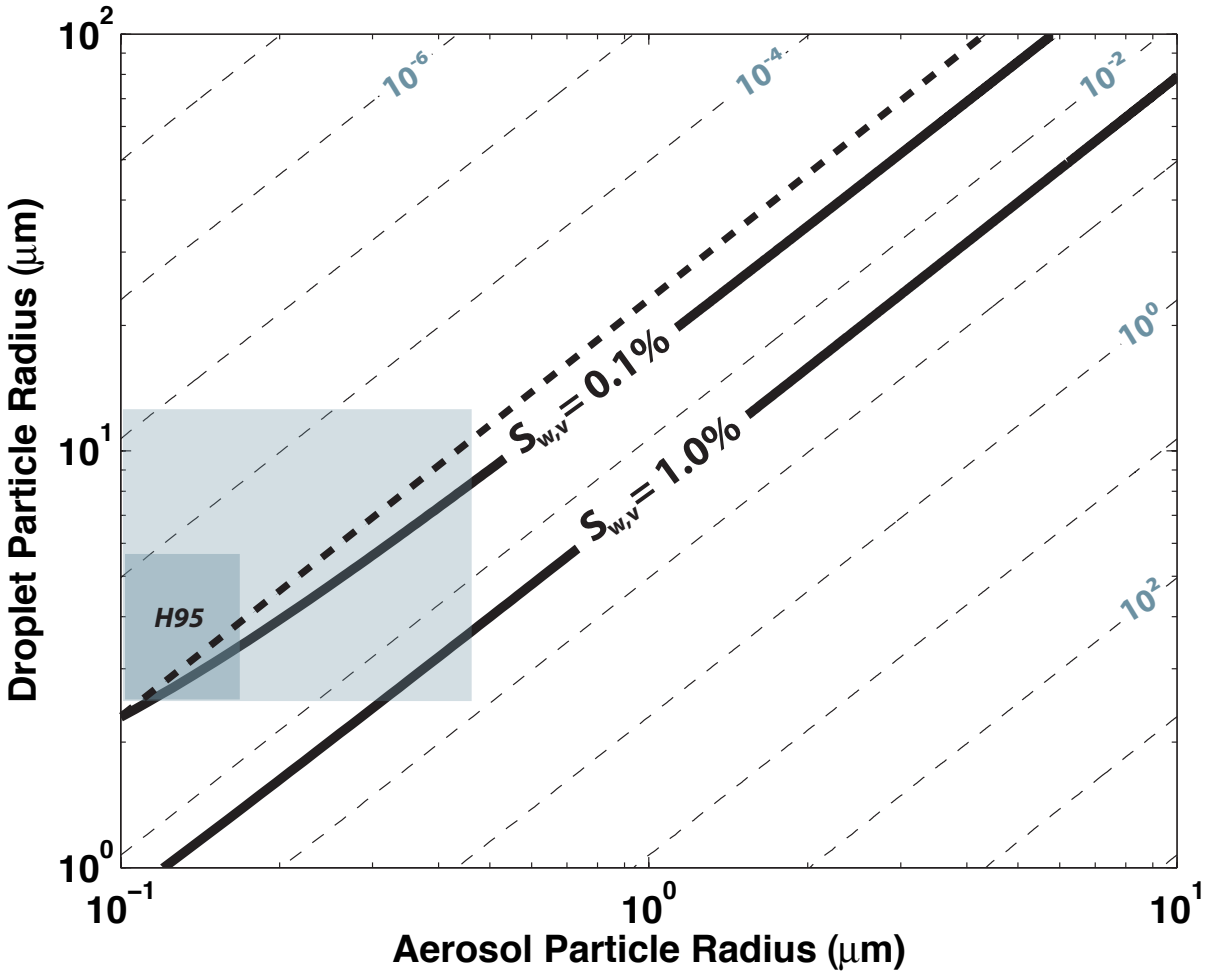

Figure 5.2: Molality (moles/liter) of the droplet solution plotted as a function of drop radius and aerosol radius (dashed lines, grey labels). The 10^{-3} moles/liter line is shown as a bold dashed line. Also plotted is the activation radius of liquid droplets corresponding to 0.1% and 1% supersaturation (bold lines). Finally, a range of Arctic observations for aerosol and droplet sizes derived from the literature is illlustrated (light grey box) as well as a shared set of observations from a single flight from Hegg et al. (1995, dark grey box). Here, the aerosol particles are assumed to be 70% soluble by mass, and consisting of a combination of NH_4HSO_4 and illite.

point depression from the concentration of soluble mass exists in observed cloud droplets, a conclusion that is contrary to the statement from Khvorostyanov and Curry (2004, hereafter KC04) that solution effects for activated droplets are small, and in agreement with PK97s (pg. 354) assessment that for most mixed atmospheric aerosols drops must grow to sizes beyond activation before freezing can be initiated.

In addition to the molality of the droplet solution, the composition of the insoluble fraction of the aerosol particle is also important to its ultimate freezing point. Diehl and Wurzler (2004) simulated the freezing of droplets with different concentrations of soluble mass at different temperatures and on different insoluble particles. They showed that for ammonium sulfate drops at -20 °C, liquid droplets containing illite formed on an initial aerosol particle containing a soluble mass fraction with an equivalent radius of 0.1 μm would need to grow to a radius of $\sim$160 μm before freezing. At -30 °C, this number falls to around 10 μm. Leaitch et al. (1984) showed that soot and clay particles are common insoluble species found in the Arctic. Out of those types of particles, illite provides the earliest freezing point in the study of Diehl and Wurzler. By these calculations, droplets would likely need to grow to radii of more than 10 μm in order to freeze, but could do so at less than 100 μm.

Once the particle freezes, it is located in a heavily supersaturated environment with respect to ice (Figure 5.1, (3)). Because of its lower saturation vapor pressure, the frozen particle will grow quickly at the expense of further growth of liquid particles. Once a significant amount of ice has nucleated, further liquid growth, and therefore ice nucleation, will be greatly reduced. Droplets that have not nucleated into ice crystals are reduced in volume due to the removal of water vapor by the ice present, increasing their soluble mass concentrations. Eventually, ice particles grow to a size that can no longer be supported by vertical motion in the cloud layer, and precipitate out (Figure 5.1, (4)), resulting in the spatial vari-

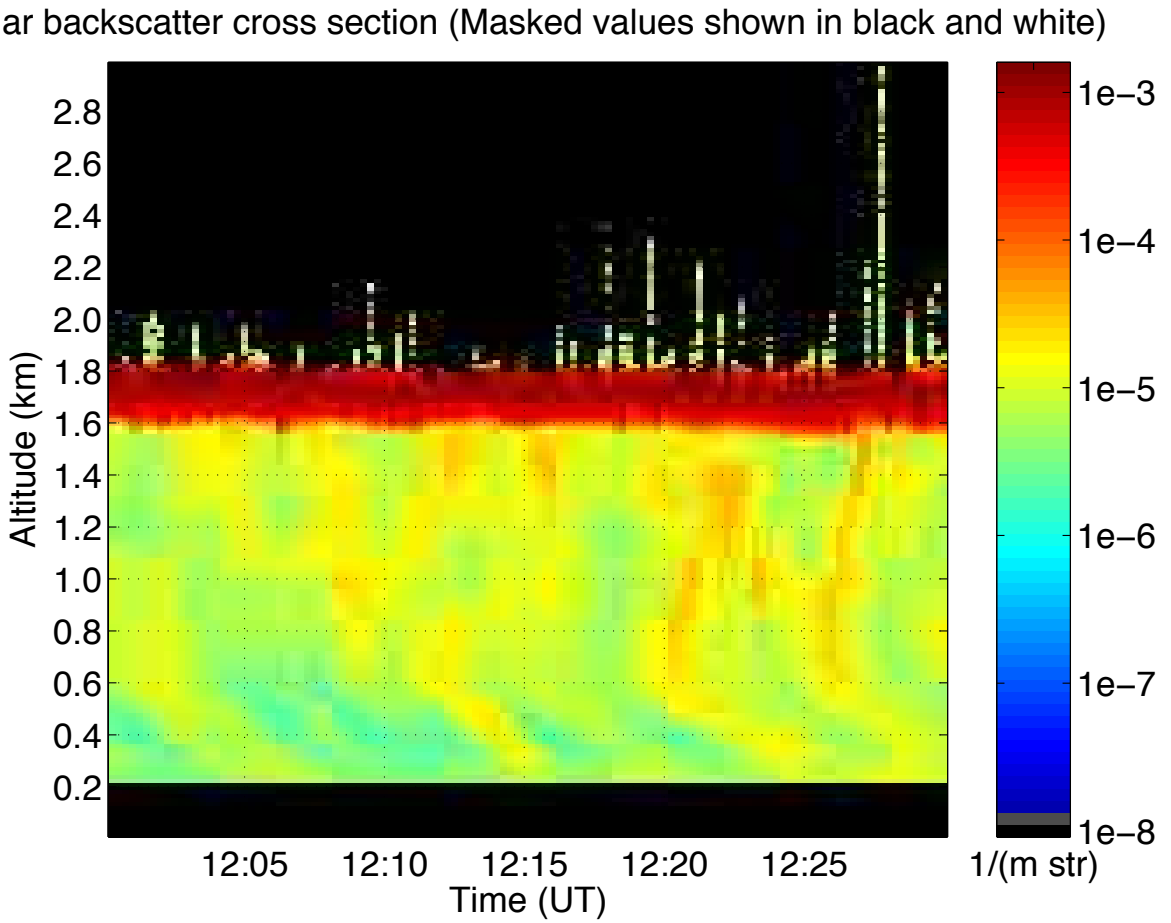

Figure 5.3: A mixed-phase stratus layer as observed in Eureka by the University of Wisconsin Arctic High Spectral Resolution Lidar. The high backscatter cross-section (red) is caused by the large number of liquid droplets in the mixed-phase layer. Note the periodic nature of the ice (yellow) precipitating from the mixed-phase layer.

ability of frozen precipitation that can be seen in Figure 5.3. As mentioned in KC04, this is a very important step in this process because it limits the amount of ice produced at any given time in any given region, and prevents rapid glaciation of the mixed-phase layer, allowing for extended cloud lifetime. Once precipitation has fallen out of the mixed-phase layer, the process repeats, starting at step 2 in Figure 5.1.

5.2 Observational evidence

This idea of droplets growing larger and freezing is supported by several recent studies investigating mixed-phase cloud maintenance. As mentioned in Chapter 4, Shupe et al. (2008a) illustrate a strong correlation between upward vertical motion and liquid water path (LWP) and ice water path (IWP) as measured by a 35 GHz millimeter cloud radar and microwave radiometer. Increases in both LWP and IWP are shown to occur within the updrafts, with only minimal IWP in areas of downward vertical motion. It is also suggested that liquid water seems to respond most quickly to the presence of an updraft, while the response of ice is slightly lagged in time behind that of liquid. This observation fits the presented theory nicely, as water droplets would grow in the updrafts under supersaturated conditions increasing LWP, and rapidly freeze, halting the LWP increase and increasing the IWP through continued depositional growth of the newly formed ice particles.

In addition to the study completed by Shupe et al., in-situ measurements from SHEBA presented by Rangno and Hobbs (2001) revealed a strong correlation between the concentration of larger liquid particles (>20 μm) and that of ice particles. Additionally, it is noted that for one of the cases observed, frozen drops make up 424 of 2174 observed ice particles, placing second behind only irregularly shaped ice particles (802/2174) which are later explained to be caused in part by shattering of isolated drops undergoing freezing. This correlation between larger droplets and ice formation, as well as the significant contributions to the observed ice crystal population from frozen droplets appears to indicate an active immersion freezing regime.

5.3 Discussion and implications

The inability of numerical simulations to accurately represent the mixed-phase in stratiform cloud structures represents a large void in our understanding of the Arctic climate. Because models are often producing too much ice, they cannot maintain the liquid portion of the cloud, thereby greatly affecting radiative characteristics of the cloud layer. The immersion freezing mechanism presented here represents a pathway to limiting the amount of ice produced and a better understanding of ice nucleation in mixed-phase stratiform clouds. Unfortunately, very few models currently utilize an immersion freezing parameterization that directly takes concentration of soluble mass within a droplet into consideration. One parameterization which does include a solution-induced contribution to the freezing point depression has been presented in Diehl and Wurzler (2004), providing a pathway to more accurately capture immersion freezing in mixed-phase scenarios.

It should be noted that this is not believed to be the only active nucleation mechanism in mixed-phase stratus, but rather one of several that are likely operating simultaneously. Here, an overview of other nucleation modes, and their likelihood in the mixed-phase scenario is discussed. Looking first at the secondary nucleation modes discussed in Chapter 2, the combination of liquid water and ice particles seems to be conducive to both drop shattering and splinter production during riming. However, as discussed in Chapter 4 typical droplet sizes are too small to support an active drop shattering regime, and temperatures observed under mixed-phase conditions fall significantly outside of the -3 to -8 °C range provided for the Hallett-Mossop mechanism. In addition, ice-ice collisions seem unlikely due to the very low ice crystal number concentrations ($\sim$ 0.1-10 L^{-1}). In addition, an IN recycling process, such as the mechanism through which ice particles nucleate on the residual particles left from evaporating droplets (Fridlind et al., 2007), though interesting and

worthy of further investigation, has not been observed in the atmosphere.

A similar review of the primary nucleation modes can be completed. The first thing that becomes apparent is that within the supercooled liquid cloud layer, it is likely that the environment is supersaturated with respect to ice. Therefore, uncoated IN would form ice crystals quite rapidly, which would grow and fall out of the cloud layer, removing the IN from that layer. The same would be true for contact freezing. This rapid depletion of IN from the cloud layer would contest the observations that show long-lived, continuously precipitating cloud layers. Therefore, there would have to be an additional source of IN either above or below the cloud layer in order for either of these two mechanisms to be a primary ice production mechanism for mixed-phase stratiform layers. Although it may be possible that IN are introduced into the mixed-phase layer through cloud top entrainment, eventually that source would be depleted as well, again halting further nucleation of ice particles. This leaves immersion and condensation freezing. KC04 provide a thorough discussion on condensation freezing for mixed-phase stratiform layers. However, as previously discussed in this chapter, given the high soluble mass fractions observed in the Arctic, there would be a significant freezing point depression associated with the freezing of haze particles activated during condensation of water vapor onto the aerosol particle.

With immersion freezing currently poorly represented in many models, significant time is being spent to adjust ice nucleation schemes acting in other modes (such as condensation/deposition freezing) to better fit observations (e.g. Morrison and Pinto, 2005). The production of ice through immersion freezing as outlined above would likely alter these results and require adjustments made to simulation of alternative nucleation modes to be reconfigured.

Chapter 6

Simulations

6.1 Model Description

6.1.1 The University of Wisconsin Non-Hydrostatic Modeling System

To better understand characteristics supporting mixed-phase stratiform clouds, and to test the hypothesis presented in Chapter 5, numerical simulations were completed utilizing the University of Wisconsin Non-Hydrostatic Modeling System (UW-NMS, Tripoli, 1992). The UW-NMS was designed as a fully scalable mesoscale model, capable of cloud-scale simulation. The formulation of the NMS is enstrophy-conserving and utilizes a quasi-compressible closure formulated in the non-Boussinesq framework. The UW-NMS diffusion scheme is based on the turbulent kinetic energy budget. For simulations discussed in this section, two different radiative transfer models were applied. Early simulations (MPACE case) were completed utilizing a cloud active long and short wave radiation scheme (Ackerman and Stephens, 1987). Later simulations (SHEBA case) were completed using long and short-

wave rapid radiative transfer models from Atmospheric and Environment Research Inc. (AER).

6.1.2 The Advanced Microphysical Prediction System

For most simulations discussed in this work, a novel new bin microphysical scheme is utilized. The Advanced Microphysical Prediction System (AMPS, Hashino and Tripoli, 2007) is composed of several components. Liquid microphysics is handled by the Spectral LIquid Prediction System (SLIPS), aerosol microphysics by the Aerosol Prediction System (APS) and ice phase microphysics by the Spectral Ice Habit Prediction System (SHIPS).

SliPS, simulates vapor deposition, collision-coalescence and collision-breakup processes for the liquid phase. This is handled in a mass-based bin method, with prognostic variables including concentration and mass content. In the majority of the work presented here, 40 mass bins were utilized, with 20 bins assigned to droplets with radii ranging between 0.1 μm and 25 μm, and the other 20 handling droplets with sizes between 25 μm and 5 mm. Liquid particle property variables (PPVs) predicted include aerosol mass content and aerosol soluble mass content. Vapor deposition onto activated droplets is calculated in the model. Collision processes are modeled using a quasi-stochastic approach. Finally, the model of Low and List (1982) is used to include collision processes.

The APS predicts two types of aerosols. Purely insoluble aerosols are considered to be ice forming nuclei (IN) while mixed aerosol particles, consisting of both soluble and insoluble mass are considered to be cloud condensation nuclei (CCN). Aitken and accumulation mode CCN are simulated using two lognormal distributions, while IN are simulated with a monodisperse distribution. As with SliPS, APS predicts concentration and mass content, along with the PPV soluble mass content. Sources and sinks considered for aerosols include

evaporation of hydrometeors and nucleation scavenging. Deposition-condensation freezing is therefore a sink for IN, while CCN are only removed through cloud droplet activation. The fraction of cloud droplets activated is based on formulations from Abdul-Razzak et al. (1998), and are based on the Köhler curve for mixed aerosol particles.

SHIPS simulated the ice phase, utilizing 20 mass bins. This unique system simulated the evolution of ice article properties through physical mechanisms, rather than pre-assigned pathways. Ice nucleation modes handled in SHIPS include deposition/condensation freezing, contact nucleation and immersion freezing. Deposition/condensation freezing is estimated using a parameterization from Meyers et al. (1992). This nucleation mode becomes active at temperatures below -5 °C when the environment is supersaturated with respect to water, or if the supersaturation with respect to ice exceeds 5%. Contact nucleation is simulated following Young (1974). This formulation considers interactions between IN and water droplets due to Brownian diffusion, thermophoresis, and diffusiophoresis, with the latter following calculations by Cotton et al. (1986). Immersion freezing was initially simulated using the stochastic hypothesis from Bigg (1953), and has since been updated to include solubility effects in droplets after Diehl and Wurzler (2004). In this implementation, the freezing rate for pure water droplets of similar sizes containing insoluble particles is given by:

$$-\frac{dN_f}{dt} = N_u a B_{h,I} V_d \exp(-aT) \frac{dT}{dt} \tag{6.1}$$

where N_f is the number of frozen droplets, N_u the number of unfrozen droplets, V_d the drop volume in cm^3, T the temperature in °C, and a and $B_{h,I}$ constants, with $a = 1\,°C^{-1}$. $B_{h,I}$ represents the nucleating efficiency in the immersion mode of an insoluble particle type, per unit volume of liquid. Immersion freezing acts as a sink for liquid hydrometeors.

A unique aspect of SHIPS is that it allows for an evolutionary size spectrum for ice or liquid hydrometeors. This is accomplished through the use of a modified spectral approach, which assumes a simple log-linear distribution for a limited number of mass-size bins. The slope and intercept of the distribution are defined by relationships requiring mass and concentration conservation between neighboring bins during a growth process. As a result, complex multi-modal distributions of ice or liquid hydrometeors, such as those found in mixed-phase situations, can evolve with complexity dependent upon the number of bins assigned to the hydrometeor type.

A second very unique aspect is that the ice model makes no a-priori assumption of ice characteristics such as habit, size and density. This is a key innovation of SHIPS because it allows ice habits to evolve as a function of particle history. This results in an infinite number of habit configurations and overcomes a long-standing shortcoming of previous ice microphysics parameterizations that simulate the variability of ice habit only through the formation of a few specific ice categories such as cloud ice, graupel, snow. The problem with the traditional approach is that no history of particle evolution is stored. This makes it very difficult to formulate inter-habit conversion rates as well as capture evolutionary subtleties within habits. In SHIPS, the ice in each ice (and liquid) bin contains characteristics that are advected with that ice mass throughout the cloud. These characteristics include total ice mass, length of a, c and dendritic axes, and the amount of rime mass collected. Quantities such as growth rate, fall velocity, collision and collection efficiency depend on these evolving ice characteristics. Then, at any point, these evolved parameters can be utilized to diagnose ice particle habits for any bin (i.e. dendrite, plate, column, rosette, aggregate, low-density graupel, hail, etc.).

6.1.3 Bulk microphysics scheme

Despite the above mentioned shortcomings, some of the simulations completed for the MPACE intercomparison were run using a traditional bulk microphysics scheme in order to asses its effectiveness in simulating the mixed-phase. This scheme, described in Flatau et al. (1989), includes class separation between cloud water, rain, pristine ice crystals, snow, graupel and aggregates. Conversion between categories occurs via collection of particles, vapor deposition, melting, and particle nucleation. Although these pathways represent realistic processes, the limitation to a small number of particle types and interactions reduces the accuracy of prediction of both ice and liquid characteristics. Because of this, analysis of the influences of individual microphysical processes is handled using AMPS.

6.2 Model case studies

6.2.1 10 October, 2004

Preliminary simulations were completed in conjunction with the Atmospheric Radiation Measurement (ARM) programs Cloud Parameterization and Modeling Working Group and the Global Cloud System Study (GCSS) Polar Cloud Working Group. This model intercomparison (Klein et al., 2009) was designed to document the current state of mixed-phase cloud microphysics in models, and to understand sources of differences between models in their simulations of mixed-phase clouds.

6.2.1.1 Case overview

Simulations using the UW-NMS were completed for case B of the intercomparison study, a single layer mixed-phase cloud observed during the ARM MPACE campaign described in Chapter 4. From 9-14 October, 2004, a persistent anticyclone situated to the north of Siberia resulted in east-northeasterly near surface winds. This led to cold air being advected from over the sea ice pack to over relatively warmer open waters of the Beaufort Sea, creating cold-air outbreak conditions. These conditions feature large ocean sensible and latent heat fluxes and a well-mixed cloud-topped boundary layer. Clouds forming on the tops of boundary layer rolls were advected to the Alaskan coast, bringing them over the observation site at Barrow (Figure 6.1).

Observations showed a continuous cloud layer over Barrow during the simulation period (1700Z 9 October 0500Z 10 October). An idealized atmospheric sounding was provided for model initialization (Figure 6.2). In addition, large-scale forcings were derived from an analysis of European Centre for Medium-Range Weather Forecasts (ECMWF) model data. Included were large-scale horizontal advective tendencies of vertical velocity, temperature and water vapor. Surface fluxes were specified to the ECMWF values of 136.5 Wm-2 for sensible heat and 107.7 Wm-2 for latent heat.

Aerosol specifications were given based on a Hand-Held Particle Counter (HHPC-6) on board an Aerosonde unmanned aerial vehicle and a CCN counter provided by the NOAA Climate Monitoring Diagnostics Laboratory (CMDL). The CCN size distribution was given as:

$$\frac{dN}{d\ln(r)} = \frac{N_t}{\sqrt{2\pi}\ln(\sigma)} \exp\left[\frac{\ln^2(r/r_m)}{2\ln^2\sigma}\right] \tag{6.2}$$

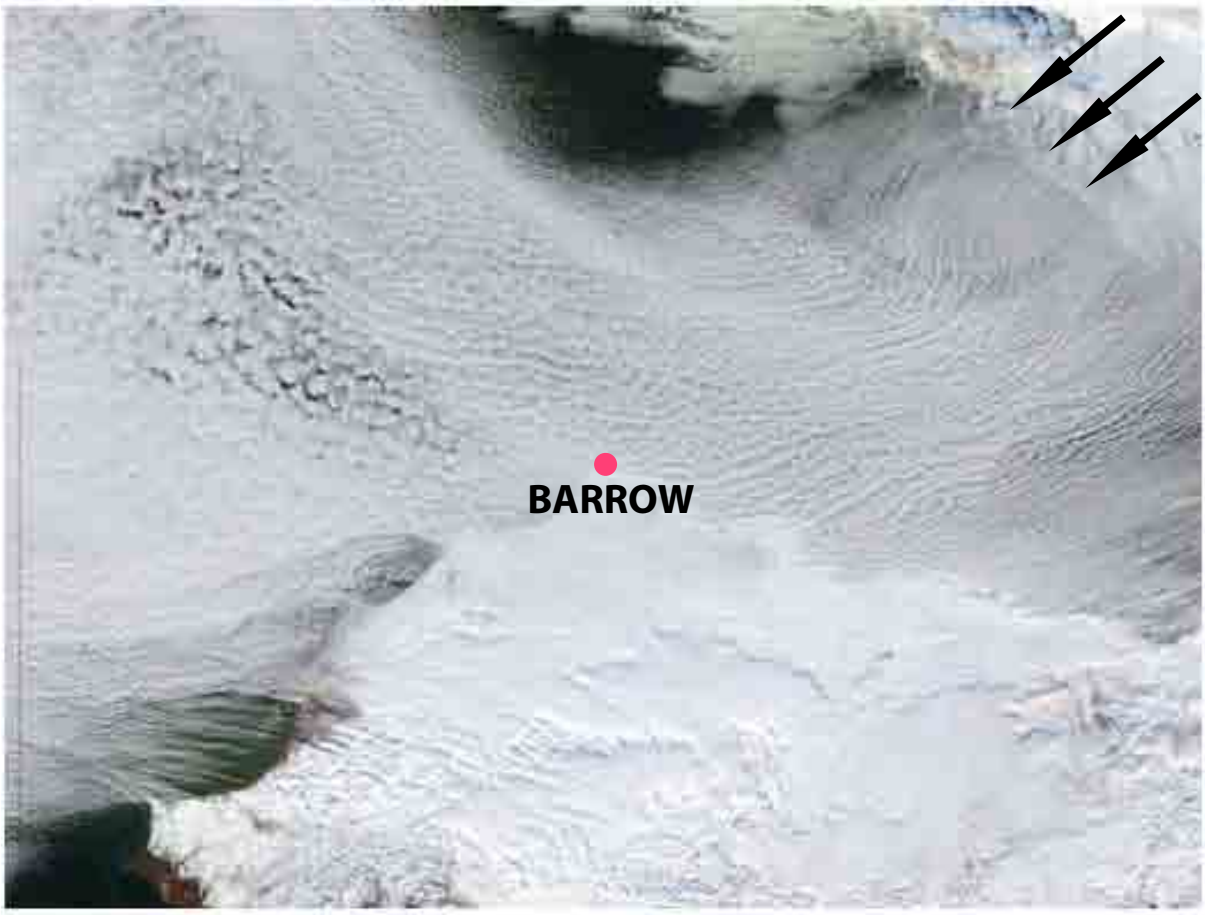

Figure 6.1: A composite visible satellite image from the NASA Terra satellite for October 9, 2004 (from Klein et al., 2005). The arrows denote the wind direction.

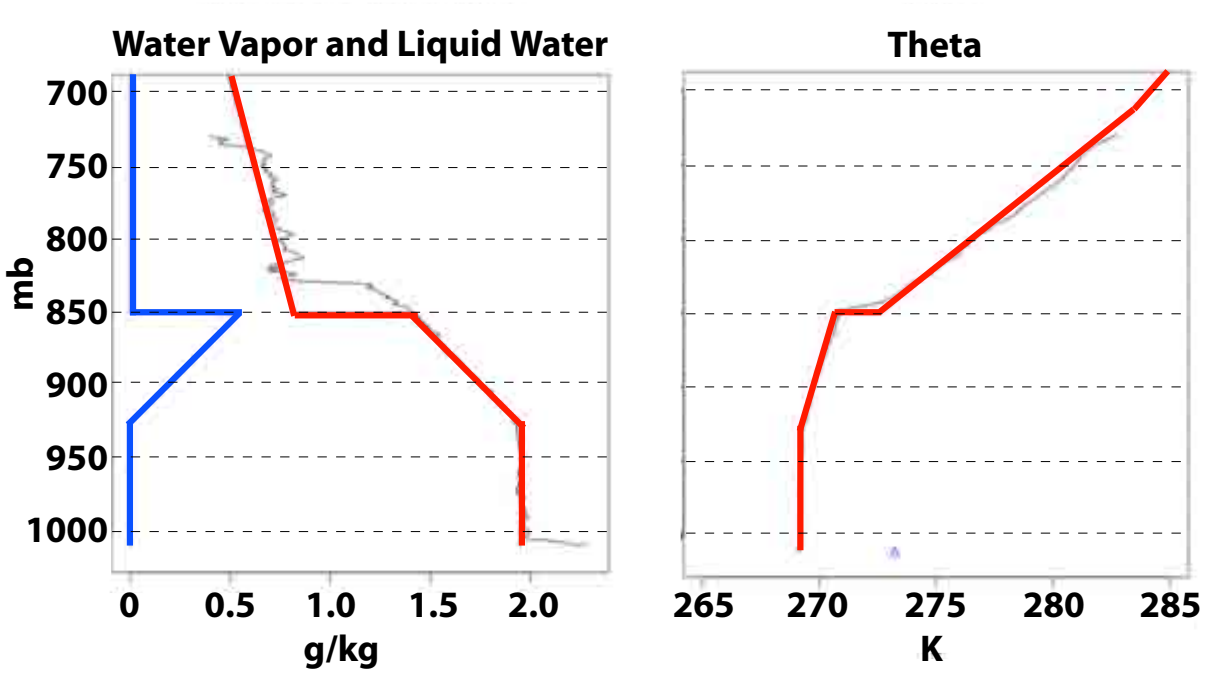

Figure 6.2: Profiles of water vapor, cloud liquid water and potential temperature used for the 9-10 October simulations (from Klein et al., 2005).

where σ, r_m and N_t are the standard deviation, geometric mean and total number concentration of each mode, respectively. For the smaller aerosol mode, these values are 2.04, 0.052 μm and 72.2 cm^{-3}, respectively. For the larger aerosol mode, these values are 2.5, 1.3 μm and 1.8 cm^{-3}, respectively. All CCN were assumed to consist of ammonium bisulfate with a soluble mass fraction of 70%.

Ice nuclei (IN) concentrations for particles smaller than 2 μm were derived from Continuous Flow Diffusion Chamber measurements taken aboard the University of North Dakota Citation aircraft. This instrument provides an estimate of ice nuclei concentrations acting in the deposition, condensation freezing and immersion freezing modes, but not the contact-freezing mode. Generally, these measurements indicated locally elevated concentrations of IN (up to 10 L^{-1}), with a mean value of only around 0.16 L^{-1}. The mean value was assumed for the simulations.

6.2.1.2 Simulation results

Both simulations completed using AMPS and the bulk microphysics resulted in a completely glaciated cloud layer when ice processes were included. Figure 6.3-Figure 6.6 illustrate time and space averaged mixing ratios for cloud water (reff $\leq$ 50 μm), rain (reff $>$ 50 μm), cloud ice (maximum dimension $\leq$ 100 μm), snow (unrimed, maximum dimension $>$ 100 μm) and graupel (rimed, maximum dimension $>$ 100 μm) for the four simulations completed. Averages were calculated only over model grid points that featured the particular category of interest, with a minimum threshold of 10^{-2} gkg^{-1} used for cloud water and 10^{-4} gkg^{-1} for all other categories. The simulation including full bulk microphysics (Figure 6.3) very rapidly loses all cloud water. This is converted to small ice particles, some of which are converted to graupel while cloud water is still available. Also, there is a small amount of rain early on in the simulation. When ice formation processes are removed, the simulation does maintain a raining liquid cloud layer (Figure 6.4).

Cloud lifetime is extended when using AMPS (Figure 6.5), with significant cloud water mixing ratios present through approximately half of the 12-hour simulation period. This simulation also produced a larger amount of rimed ice particles early on in the simulation than the bulk simulation, as may be expected in an environment supersaturated with respect to water. Once cloud water was converted to ice mass, riming ceased, and nucleated particles only grow into the snow category. A minimal production of cloud ice mass is likely the result of rapid crystal growth both within the mixed-phase layer and outside of it. Similar to when the bulk microphysics was employed, the AMPS simulation with ice processes removed (Figure 6.6)resulted in a sustained liquid cloud throughout the 12-hour period.

Figure 6.7 shows the simulated mean total liquid (cloud+rain) and ice (cloud ice + snow

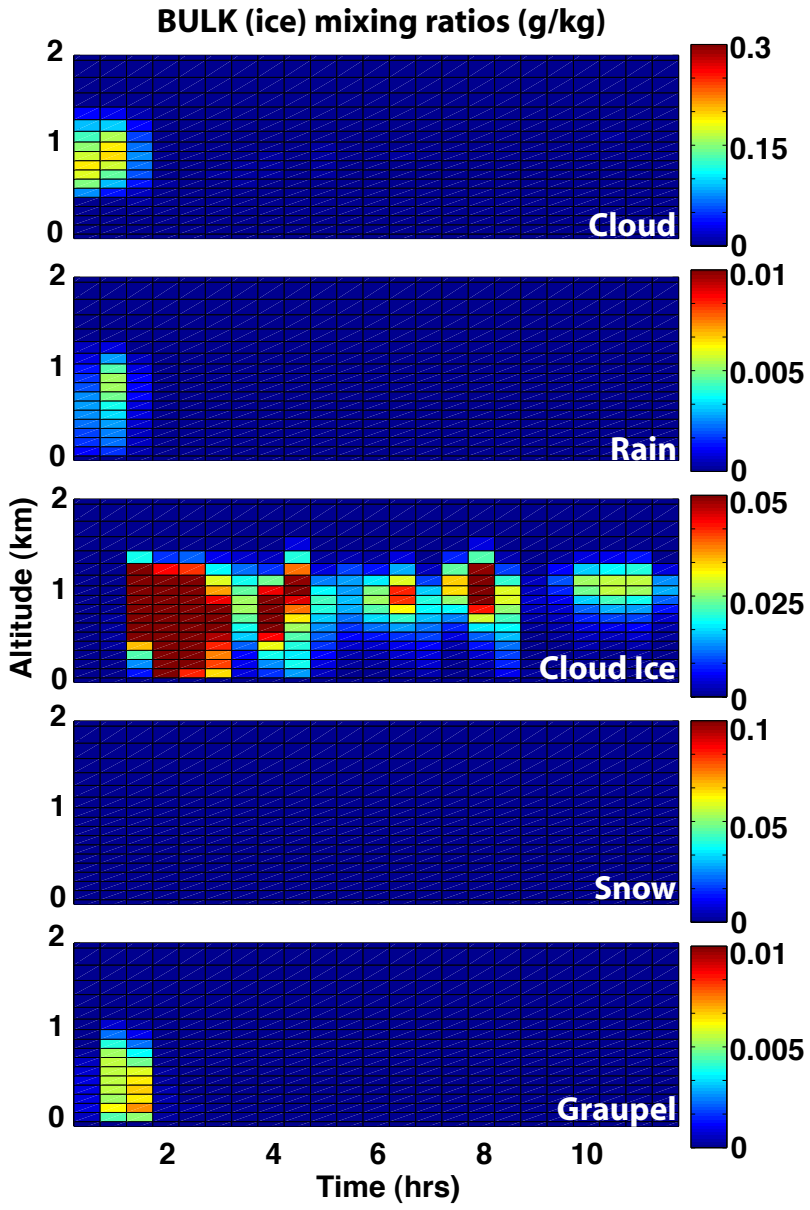

Figure 6.3: 30-minute mean simulated cloud liquid, rain, cloud ice, snow and graupel mixing ratios for 10 October, 2004 using the full bulk microphysics.

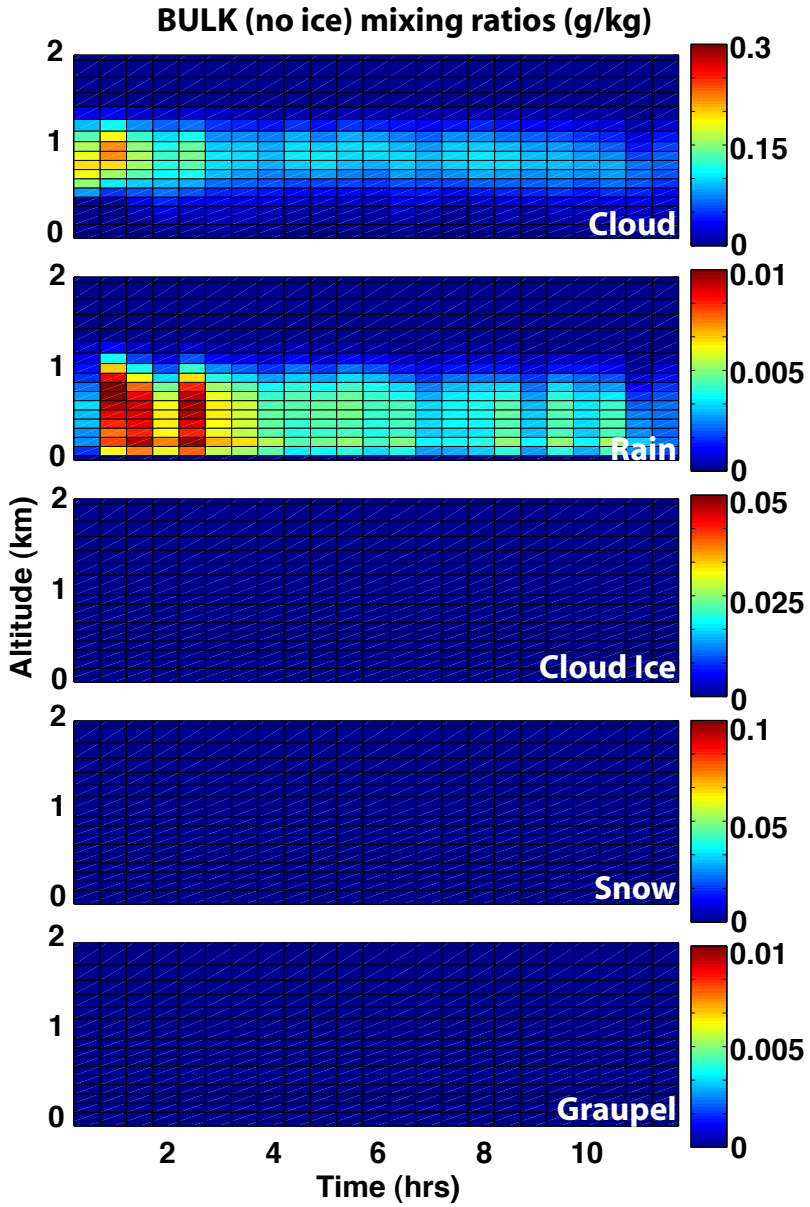

Figure 6.4: 30-minute mean simulated cloud liquid, rain, cloud ice, snow and graupel mixing ratios for 10 October, 2004 using the bulk microphysics with ice nucleation processes removed.

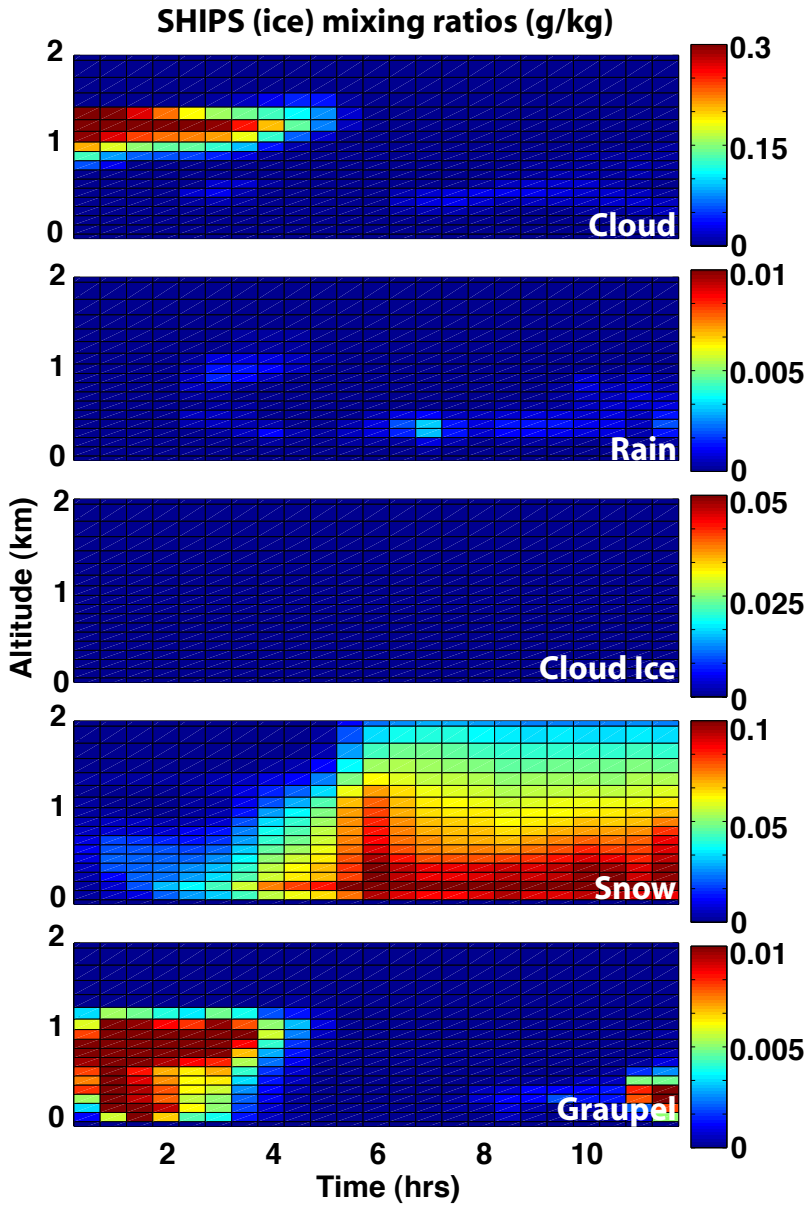

Figure 6.5: 30-minute mean simulated cloud liquid, rain, cloud ice, snow and graupel mixing ratios for 10 October, 2004 using the full AMPS microphysics.

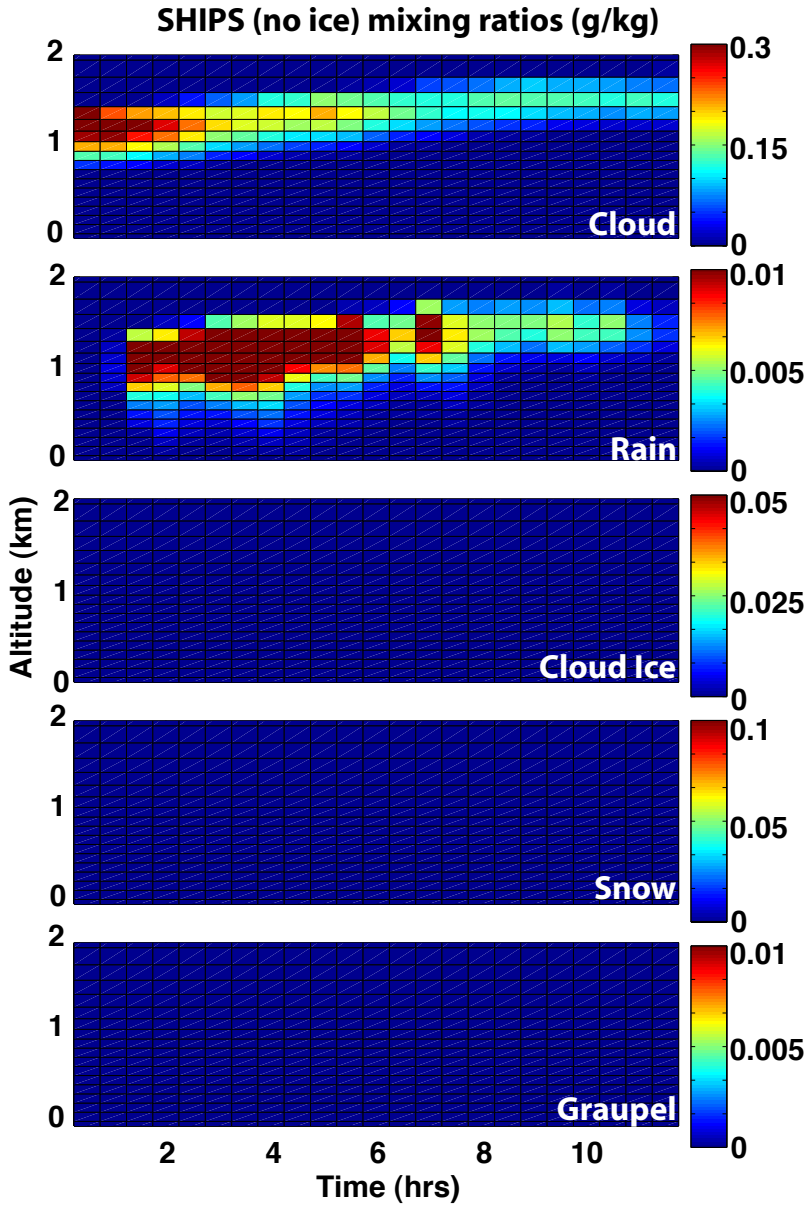

Figure 6.6: 30-minute mean simulated cloud liquid, rain, cloud ice, snow and graupel mixing ratios for 10 October, 2004 using the AMPS microphysics with ice nucleation processes removed.

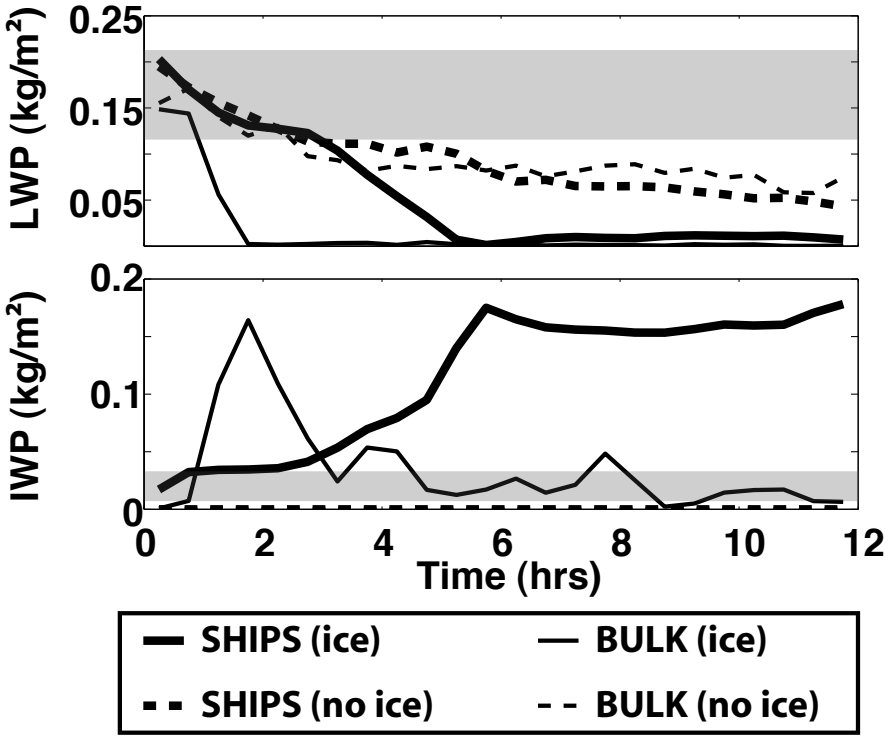

Figure 6.7: Total liquid (top) and ice water (bottom) paths from 10 October simulations. A range of estimates from observations is represented by the gray shading.

+ graupel) water paths (LWP, IWP, respectively) for all four simulations discussed above. Interestingly, despite being initialized with a specified amount of liquid water, all predicted liquid water paths quickly fall below the observed values for that date by 7 gm^{-2} or more. Ice production occurred at very different rates between the bulk microphysics and AMPS, with AMPS producing ice at a more gradual pace. However, the initial spike in IWP seen in the bulk simulation is reduced quickly, and a much smaller amount of ice is maintained than within the AMPS simulation.

With the objective of these simulations being to test the models capabilities in simulating a single-layer mixed-phase cloud, additional investigations into the causes of these differences were not completed. Nevertheless, both microphysical arrangements resulted in complete glaciation of the liquid layer due to excessive production of ice. This result, in combination

with the observational evidence presented in earlier chapters lead to the theory on immersion freezing presented in Chapter 5. This theory is explored further using the UW-NMS for a case observed during the SHEBA campaign, as explained in subsequent sections.

6.2.2 7-8 May, 1998

6.2.2.1 Case overview

The 7-8 May case involved a cloud layer observed during the SHEBA campaign. This layer was simulated as part of a recent GCSS/World Meteorological Organization (WMO) model intercomparison aimed at improving our understanding of results from the MPACE case discussed in the previous section. The simulated cloud represents part of a persistent mixed-phase cloud system that occurred continuously at SHEBA from 1-18 May. The synoptic scale pattern for the 7-8 May time period was characterized by a broad region of anti-cyclonic circulation centered above the SHEBA site. NCEP reanalysis information revealed general subsidence, with an 850-hPa vertical pressure velocity of about 1 hPa per hour. The boundary layer height had also been decreasing in response to the strengthening anticyclone.

Aircraft and ground-based instrumentation was used to determine cloud characteristics. Cloud temperatures between 253-256 K were reported. Liquid water contents from the FSSP and King probes ranged from around 0.01 gm^{-3} to approximately 0.06 gm^{-3}. Liquid water paths were very small, ranging from 10-35 gm^{-2}. Ice concentrations, as determined by the 2DC and 2DP probes ranged from near zero to around 20 L^{-1}, with a mean value of 1.44 L^{-1} below cloud, and 0.75 L^{-1} within the mixed-phase layer.

As with the MPACE case, an idealized atmospheric sounding was provided for model initialization (Figure 6.8). In addition, large-scale forcings were derived from an analysis of

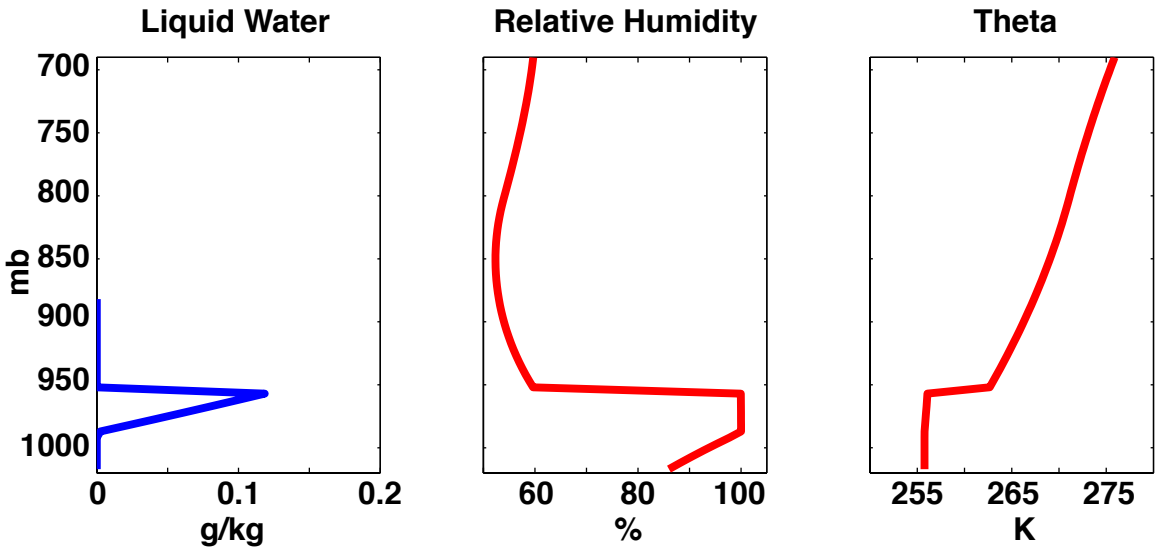

Figure 6.8: Profiles of water vapor, cloud liquid water and potential temperature used for the 7-8 May simulations (from Morrison and Zuidema, 2008).

European Centre for Medium-Range Weather Forecasts (ECMWF) model data. Included were large-scale horizontal advective tendencies of temperature and water vapor. Surface fluxes were much lower than those from MPACE, and were specified to the ECMWF values of 7.98 Wm^{-2} for sensible heat and 2.86 Wm^{-2} for latent heat.

Aerosol specifications were given based on measurements described in Yum and Hudson (2001). However, since no size or composition measurements were available, aerosol specification was done similarly to that from MPACE, with total concentrations adjusted to reflect SHEBA measurements. The standard deviation, geometric mean and total number concentration parameters for the small (large) mode were determined to be 2.04, 0.052 μm and 350 cm^{-3} (2.5, 1.3 μm and 1.8 cm^{-3}), respectively. All CCN were assumed to consist of ammonium bisulfate with an soluble mass fraction of 70%.

Again as with MPACE, ice nuclei (IN) concentrations for particles smaller than 2 μm were derived from CFDC measurements. Mean values from the 7 May flight were used in determining an ice nucleus concentration of 1.7 L^{-1}.

6.2.2.2 Simulation results

As a part of the SHEBA intercomparison, five initial simulations were completed using the UW-NMS with AMPS microphysics. A control simulation was carried out with the specifications provided in the preceding section. In order to reduce differences between models due to ice nucleation, this control simulation was completed with ice nucleation through deposition/condensation freezing in areas where supersaturation with respect to ice is greater than 5% limited by:

$$\frac{dN_i}{dt} = \max(0, (N_{IN} - N_i)/\Delta t) \tag{6.3}$$

where N_i is the total concentration of existing ice particles, N_{IN} the specified ice nuclei concentration of 1.7 L^{-1}, and Δt the model time step. In regions of supersaturation smaller than 5% (with respect to ice), no new ice is nucleated. This limit directly controls the total ice concentration by capping nucleation of new crystals. Although this may seem like an imposing limitation, a brief overview of alternate deposition/condensation freezing parameterizations should illustrate it's necessity. Traditional parameterizations, such as those from Meyers et al. (1992) are based upon empirically derived relationships between temperature, supersaturation and measurements of ice nucleus concentrations. Unfortunately, these relationships are based upon rather limited data sets, and are not necessarily indicative of IN concentrations within the Arctic. Utilization of this type of parameterization within these mixed-phase layers results in rapid glaciation of the cloud due to an over-prediction of ice nucleus availability. Here, we have adjusted the parameterization to be more representative of conditions observed during the SHEBA experiment and reduce the otherwise bottomless supply of particles for ice nucleation.

In addition to the control simulation, four required sensitivity tests were completed. The first of these is a warm case, with all ice microphysics removed, allowing for assessment of the degree to which ice microphysics alters cloud structure. Simulations with 3x (5.1 L^{-1}), and 1/10x (0.17 L^{-1}) IN concentrations were also completed. The 3xIN simulation subjects the mixed-phase layer to ice nucleus concentrations comparable to those measured at mid-latitudes (e.g. Meyers et al., 1992), while the 1/10x simulation features concentrations closer to those measured during the MPACE campaign. Finally, a simulation in which the CCN concentration was reduced to 72.2 cm^{-3} (value from MPACE) was completed, with the IN concentration set at 1.7 L^{-1}. The last three tests allow for the assessment of simulation sensitivity to aerosol properties. For all of these core simulations, only deposition/condensation freezing was considered.

Figure 6.9 shows liquid and ice water paths, along with in-cloud ice crystal concentrations from the simulations described in the previous paragraph. Ranges of MWR-retrieved estimates of liquid and ice water paths are presented by the blue bars. The simulation with ice microphysics removed eventually features a LWP over four times larger than the largest observed value. This very clearly illustrates the role that ice plays in limiting the amount of liquid water present in these layers. Simulations with limited ice nucleus concentrations show strong sensitivity to ice nucleus limitations imposed within the deposition/condensation freezing parameterization. Simulations with 1.7 L^{-1} IN generally fell within the observed liquid and ice water paths. The simulation featuring a higher IN concentration (5.1 L^{-1}) rapidly depleted the liquid cloud due to overproduction of ice. Conversely, the low IN simulation (0.17 L^{-1}) produced ice at much slower rates (and lower concentrations), resulting in an initial overestimation of the liquid water path. However, along with this increase in liquid water, IWP too steadily rises, likely due to increased ice particle growth and riming within the cloud layer. Because of this additional conversion

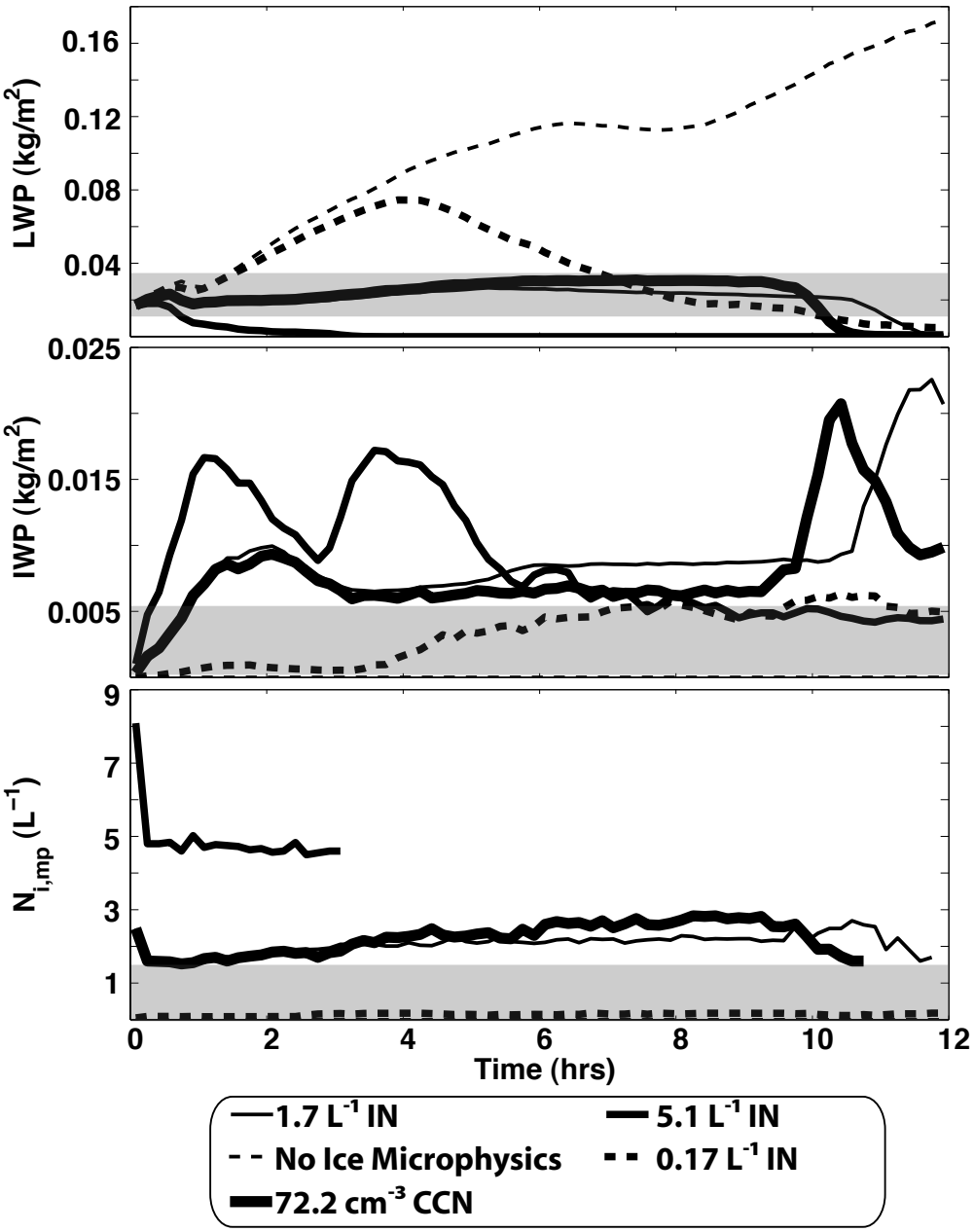

Figure 6.9: Liquid water path (top), ice water path (middle) and mean in-cloud ice particle number density (bottom) for the core intercomparison simulations. These include simulations with ice nucleus concentrations fixed at 1.7, 5.1 and .17 L^{-1}, a simulation with no ice microphysics and a simulation with a reduced CCN concentration of 72.2 cm^{-3}. The ranges of measured estimates are shown using the gray boxes.

to frozen hydrometeors, the 0.17 L^{-1} IN simulation actually loses much of its liquid water cloud before the 1.7 L^{-1} IN simulation. There was little difference between simulated LWP and IWP for the control simulation and the simulation featuring reduced CCN concentrations. Despite the relative success of the control (1.7 L^{-1} IN) simulation in reproducing the observed conditions, one question that still requires an answer is whether or not the processes simulated in this simulation are actually indicative of those occurring within the true atmosphere. In order to assess the theory on immersion freezing presented in Chapter 5, several additional simulations were completed using the SHEBA intercomparison framework. These are discussed in the following sections.

6.2.2.3 Immersion freezing sensitivity studies

The simulations discussed in this section were designed to investigate the role of immersion freezing in mixed-phase stratiform clouds, as well as sensitivity of simulated immersion freezing to different aerosol characteristics. In this effort, several questions were addressed:

- Does immersion freezing contribute significantly to ice formation in these stratiform layers?
- If so, does it occur via the mechanisms described in Chapter 5?
- How do aerosol properties affect immersion freezing within these cloud layers?

In order to address the first of these questions, several simulations including immersion freezing were completed. The first of these was carried out with only immersion freezing active, and all other ice nucleation modes turned off. This simulation assumed kaolinite as the CCN insoluble mass type, and a 70% aerosol soluble mass fraction. An attempt to replicate a more realistic environment was carried out through simulations utilizing

both immersion and deposition/condensation freezing. These simulations assumed the same CCN characteristics described in the previous sentences, and fixed nucleation rates in the deposition/condensation mode as described in the previous section to limit particle nucleation to 1.7 L^{-1}, 0.52 L^{-1} and 0.17 L^{-1} or below.

Figure 6.10 illustrates a comparison of liquid and ice water paths produced by these simulations to instrument retrievals. All simulations rapidly increase cloud liquid mixing ratios before ice formation occurs. Simulations featuring the highest deposition/condensation IN concentrations (1.7 L^{-1}) produce the highest amounts of ice, and deplete liquid water most rapidly in the early stages of the simulation. Despite maintaining comparable IWPs, the simulations with and without immersion freezing result in very different LWPs. This is not entirely surprising since ice formation in the immersion mode not only produces ice particles, but also acts as a sink for liquid water droplets.

Using simulations in which both immersion and deposition/condensation freezing were active, an assessment of the fraction of ice formation through different modes was completed. For simulations with multiple active nucleation modes, immersion freezing appears to control the total ice production. As the droplet population grows, immersion freezing increases, resulting in even larger contributions to ice nucleation from this mode. As shown in Figure 6.11, all of the simulations feature a significant immersion freezing contribution to the total ice nucleation rate, with that contribution decreasing towards the end of the liquid cloud lifetime. Simulations with smaller amounts of available IN have larger immersion freezing contributions.

The notion that immersion freezing appears to dominate ice production is reinforced in Figure 6.12, which shows freezing rates at 4 hours into the simulation for all simulations discussed in the previous two paragraphs. This figure also illustrates spatial differences between the two nucleation modes, with immersion freezing resulting in the highest ice

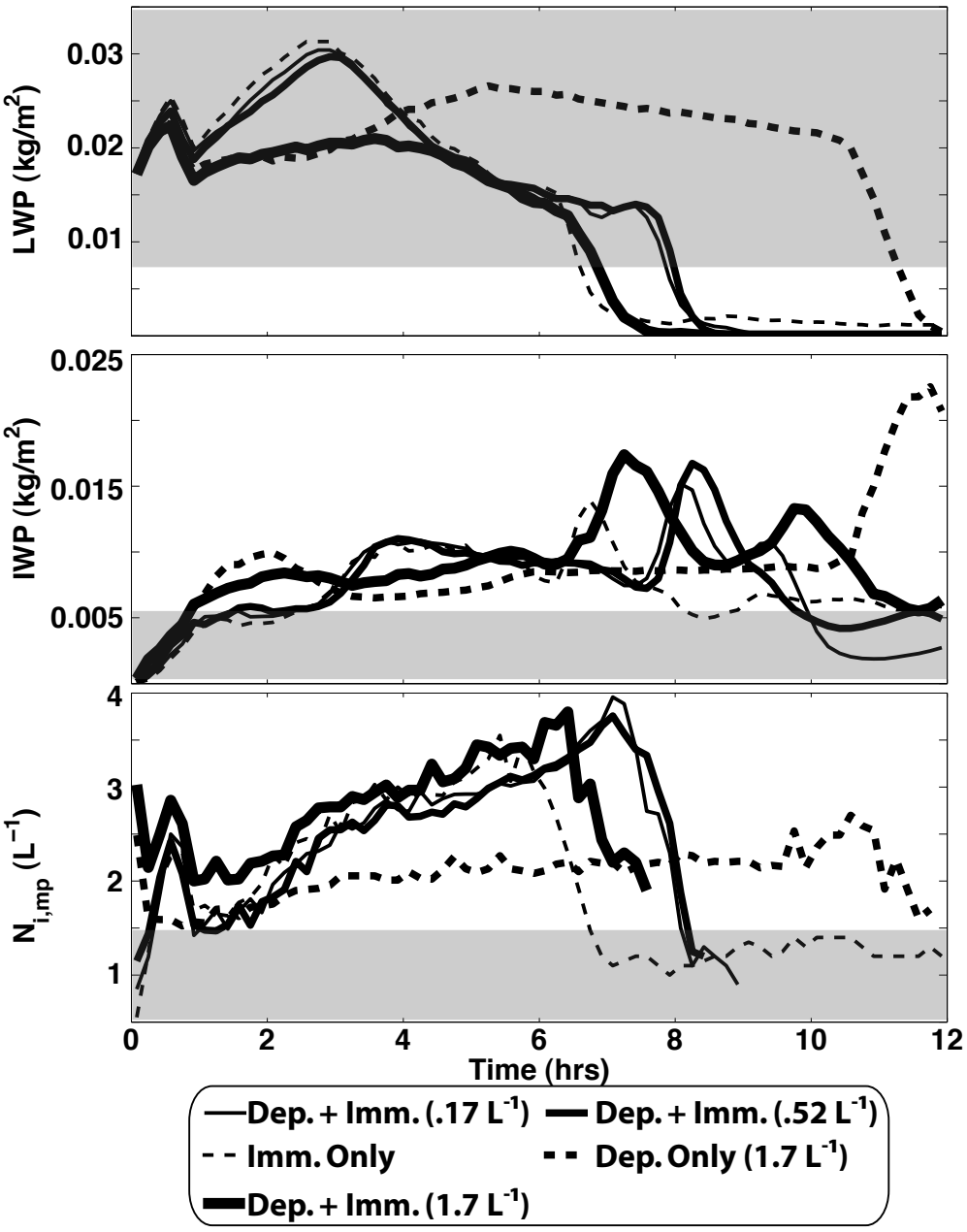

Figure 6.10: Liquid water path (top), ice water path (middle) and mean in-cloud ice particle number density (bottom) for simulations comparing different modes of nucleation. These include a deposition freezing only simulations with ice concentrations fixed at 1.7L^{-1}, an immersion freezing only simulation (Kaolinite, 70% soluble) and simulations with both immersion and deposition freezing with ice concentrations fixed at 1.7, .52 and .17 L^{-1}. The ranges of retrieved estimates are shown using the gray boxes.

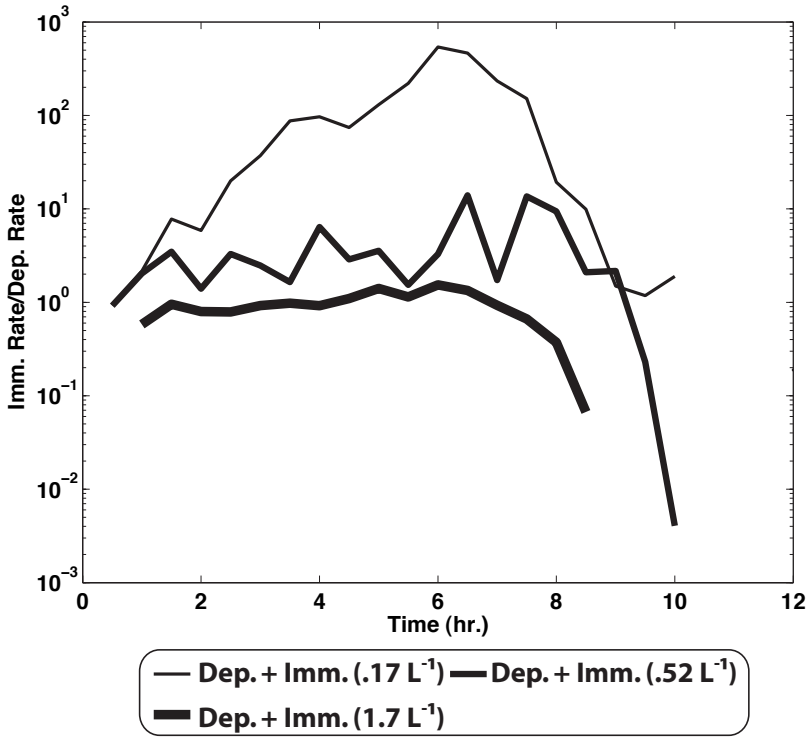

Figure 6.11: The ratio of ice particle nucleation through immersion freezing to that of deposition/condensation freezing for simulations with immersion freezing and deposition/condensation nucleation within the mixed-phase layer. Deposition/condensation freezing was limited to keep maximum ice concentrations at 1.7 L^{-1} (thick line), 0.52 L^{-1} (medium line), and 0.17 L^{-1} (thin line) or below.

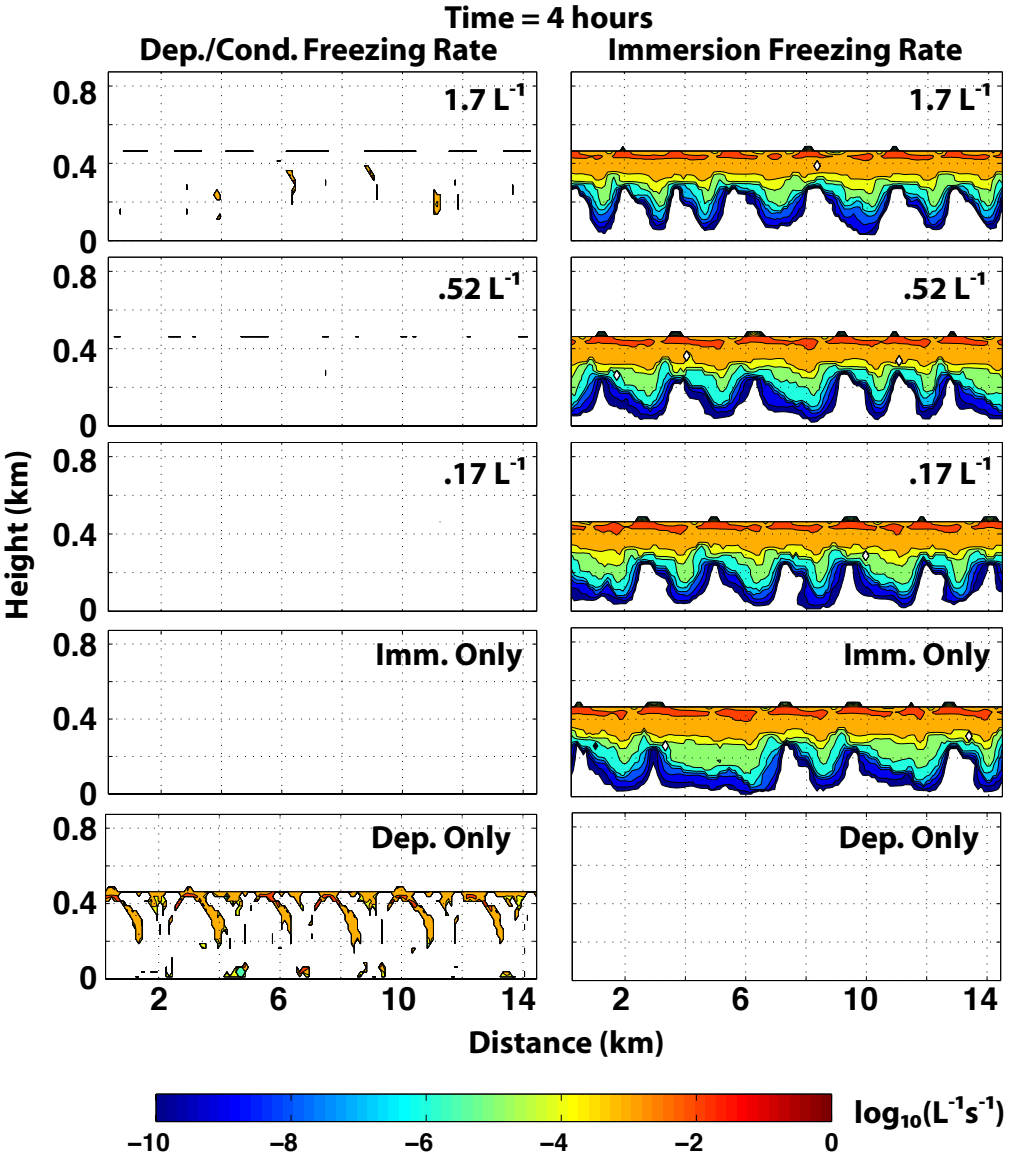

Figure 6.12: Rates of nucleation through immersion and deposition/condensation freezing at 4 hours for simulations featuring both nucleation modes, within the mixed-phase layer. Deposition/condensation freezing was limited to keep maximum ice concentrations at 1.7 L^{-1} (top), 0.52 L^{-1} (2^{nd} from top), and 0.17 L^{-1} (center) or below. The bottom two figures represent simulations with immersion freezing only (2^{nd} from bottom) and deposition/condensation freezing only ($1.7L^{-1}$, bottom).

production near cloud top where radiative cooling, liquid water content and droplet sizes are largest, and deposition/condensation freezing contributing relatively uniformly with height, wherever IN are present, ice supersaturation exceeds 5%, and the imposed maximum ice concentrations have not been met.

Given evidence that immersion freezing does indeed appear to be a significant contributor to ice formation within these mixed-phase stratiform layers, the next question to address is where and why it occurs. In Chapter 5, a theory was provided linking freezing through the immersion mode to a decrease in concentration of soluble mass within cloud droplets as they grew through updraft-induced expansion. Here, simulations featuring only immersion freezing and those with both immersion and deposition/condensation freezing active are reviewed in order to see whether this phenomenon occurs in the model.

A comparison of mean liquid droplet molality and immersion freezing rate (Figure 6.13) shows strong correlation between immersion freezing rate and location of the most diluted liquid particles. This is not surprising, as diluted droplets have reduced freezing point depressions as discussed in Chapter 5. Figure 6.14 illustrates the extent of freezing point depression as measured in laboratories. In addition, these diluted droplets are also likely larger than those with with higher concentrations of soluble mass. As reviewed in Diehl et al. (2006), larger droplets result in enhanced immersion freezing. This correlation is due to the stochastic nature of ice germ formation (Pruppacher and Klett, 1997), which states that all equal-sized ice embryos within a population of equally-sized supercooled liquid drops have equal probability of reaching critical size for droplet freezing as a result of random density fluctuations within the droplet. Since the likelihood of these fluctuations increases with increasing droplet size, the chance of the drop freezing increases as well.

To help determine the extent to which aerosol soluble mass fraction affects immersion freezing in the SHEBA case, simulations were completed with aerosol soluble mass fractions

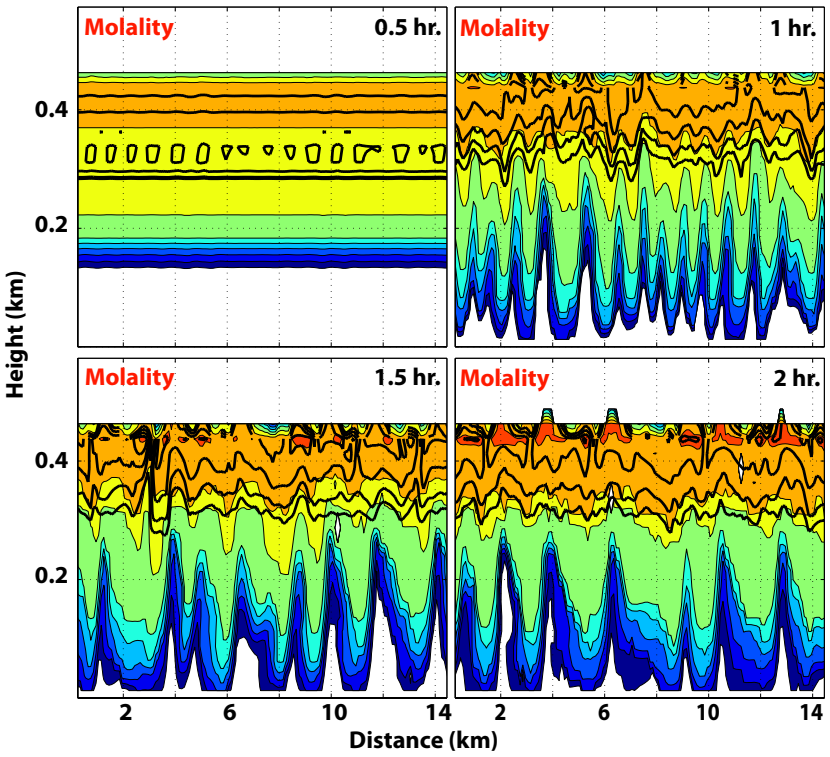

Figure 6.13: Immersion freezing rate (colored shading) and mean liquid particle molality (black contours) at 0.5, 1, 1.5, and 2 hours into the simulation with only immersion freezing active (CCN: Kaolinite + 70% soluble mass). The molality contours scaled logarithmically between 7×10^{-3} and 6×10^{-2} mole kg^{-1}.

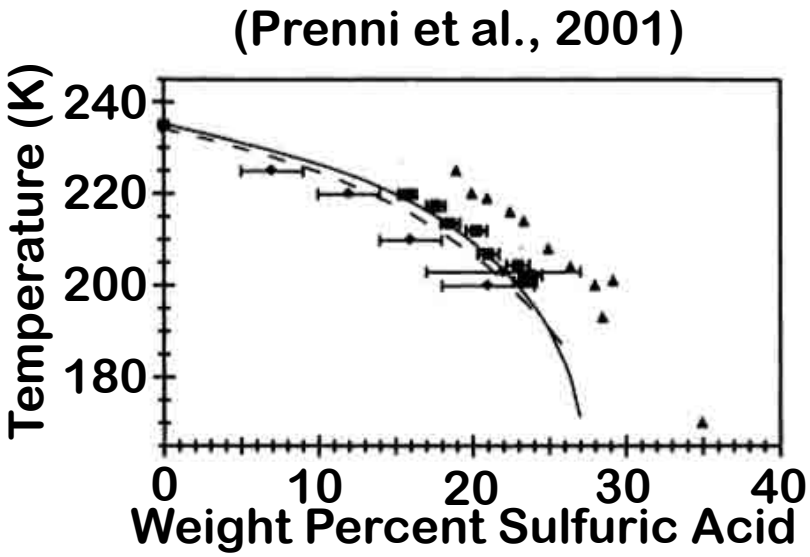

Figure 6.14: Ice formation temperature from H_2SO_4/H_2O aerosol as a function of weight percent. The squares designate the data from Prenni et al. (2001); the triangles designate the data from Bertram et al. (2000); the diamonds designate the data from Cziczo and Abbatt (1999); the solid line designates the data from Koop et al. (1998); and the dashed line designates the data of Chen et al. (2000). (Figure and caption from Prenni et al., 2001).

of 30%, 50%, 70% and 95%. All of these simulations assumed kaolinite as the insoluble mass type. Since a higher soluble mass fraction increases the freezing point depression for a droplet of a given size, in theory, simulations with higher soluble mass fractions should nucleate ice from larger droplet sizes. This occurs because droplets forming on aerosol particles with higher amounts of soluble mass would require increased volume to attain a similar dilution as smaller particles formed on aerosols containing less soluble mass. A simulation with no solution effect induced freezing point depression was also completed to illustrate the magnitude of the solution effect on ice formation in these clouds.

Figure 6.15 illustrates the effect that increased concentrations of soluble material within liquid cloud droplets have on the production of ice. Here, distributions of immersion freezing rate corresponding to binned ranges of maximum droplet diameter are displayed. The boxes represent the interquartile range of the data, grouped into 5 μm bins. The box center represents the median immersion freezing rate for that size bin, the box edges the interquartile range (IQR), and the whiskers represent the IQR +/- two times the IQR. The black circles represent values outside of this range and mean values are represented by the red dots. The simulation with no solution effect calculations and the one assuming 30% aerosol soluble mass have comparable freezing rates at small drop sizes, with the other simulations having lower rates of immersion freezing due to the induced freezing point depression. Decreases in immersion freezing rates at larger droplet sizes are likely the result of smaller number of droplets at those sizes.

The anticipated delay in freezing associated with initial aerosol soluble mass fraction does appear to influence mean simulated ice and liquid water paths, as well as the number of ice particles produced (Figure 6.16). However, these effects appear to be small and non-linear. Initially, all of the simulations feature approximately similar rates of crystal formation. Once new liquid particles are nucleated, however, the simulations begin to diverge. As ex-

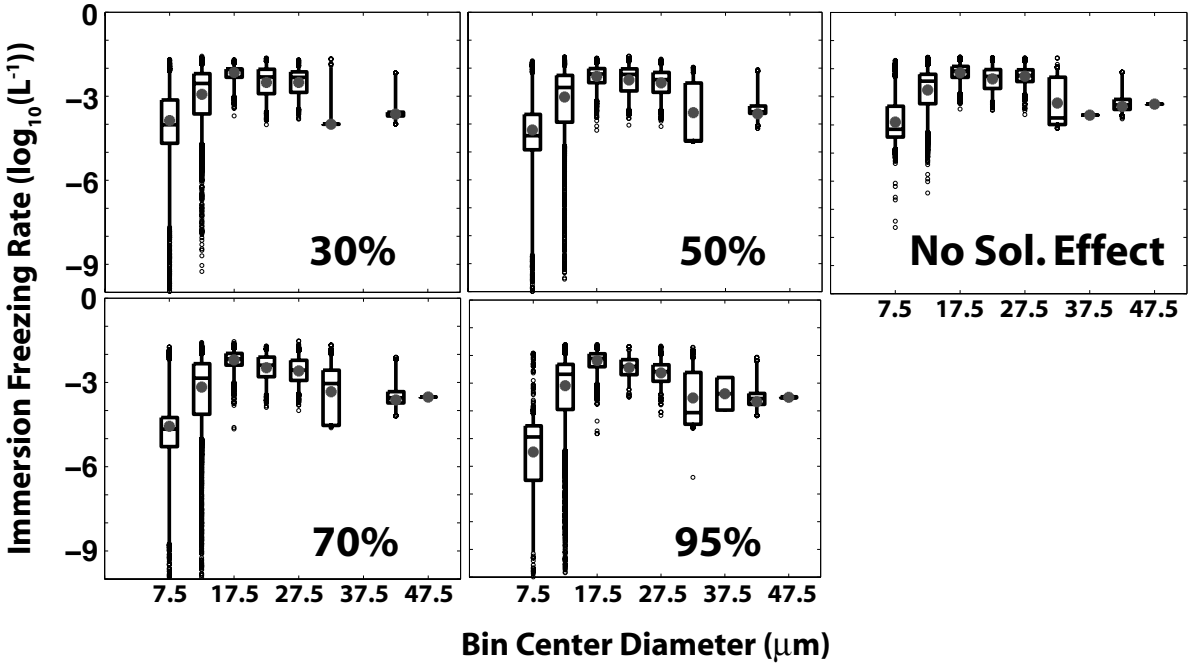

Figure 6.15: The distribution of immersion freezing rate within the liquid cloud layer (q_c > 0.01 gkg^{-1}) over ten liquid droplet size bins for simulations featuring different aerosol soluble mass fractions. The boxes represent the interquartile range (IQR), with the line in the center representing the median value, and whiskers illustrating the IQR +/- 2xIQR. Circles are representing outliers (> IQR +/- 2xIQR). The mean values are represented by the grey dots.

pected, the simulation with the highest aerosol soluble mass fraction results in the smallest number of ice particles nucleated, while the simulation with no consideration for solubility effects nucleates the most particles. Interestingly, the simulation featuring 70% aerosol soluble mass fractions glaciates first, illustrating some of the non-linear characteristics of these interactions. Because aerosol soluble mass fraction also influences the particle's water nucleating ability (increased CCN activation with increased soluble mass fraction), and larger numbers of liquid droplets may induce increased growth of nucleated ice particles via riming, this combination can lead to more ice mass formation than a lower aerosol soluble mass fraction. Regardless, the simulations generally follow similar patterns, and all result in near-total glaciation by approximately nine hours.

Similarly, Figure 6.17 illustrates the effect of droplet freezing point depression through soluble mass fraction on average rate of immersion freezing over the 12-hour simulation period. The simulation not including the freezing point depression maintained a higher rate of ice production throughout the most of the simulation period. Ice production in the other simulations is more or less controlled by aerosol soluble mass fraction until approximated 6 hours into the simulation, at which point some of the previously discussed non-linear features come forward. Clearly obvious here is the ability of the simulation featuring 95% soluble mass to maintain larger immersion freezing rates for a longer time period due to an enhanced liquid cloud lifetime.

Having determined that the soluble mass fraction can reduce freezing under the current conditions, and that larger droplet sizes result in enhanced freezing rates in scenarios with larger aerosol soluble mass fractions, the next step is to determine where in the cloud conditions are favorable for freezing to occur. Initially, it was believed that droplets were cooled through expansion as they rose through the cloud within updrafts, resulting in larger droplets near cloud top which then freeze. Examination of the immersion freezing

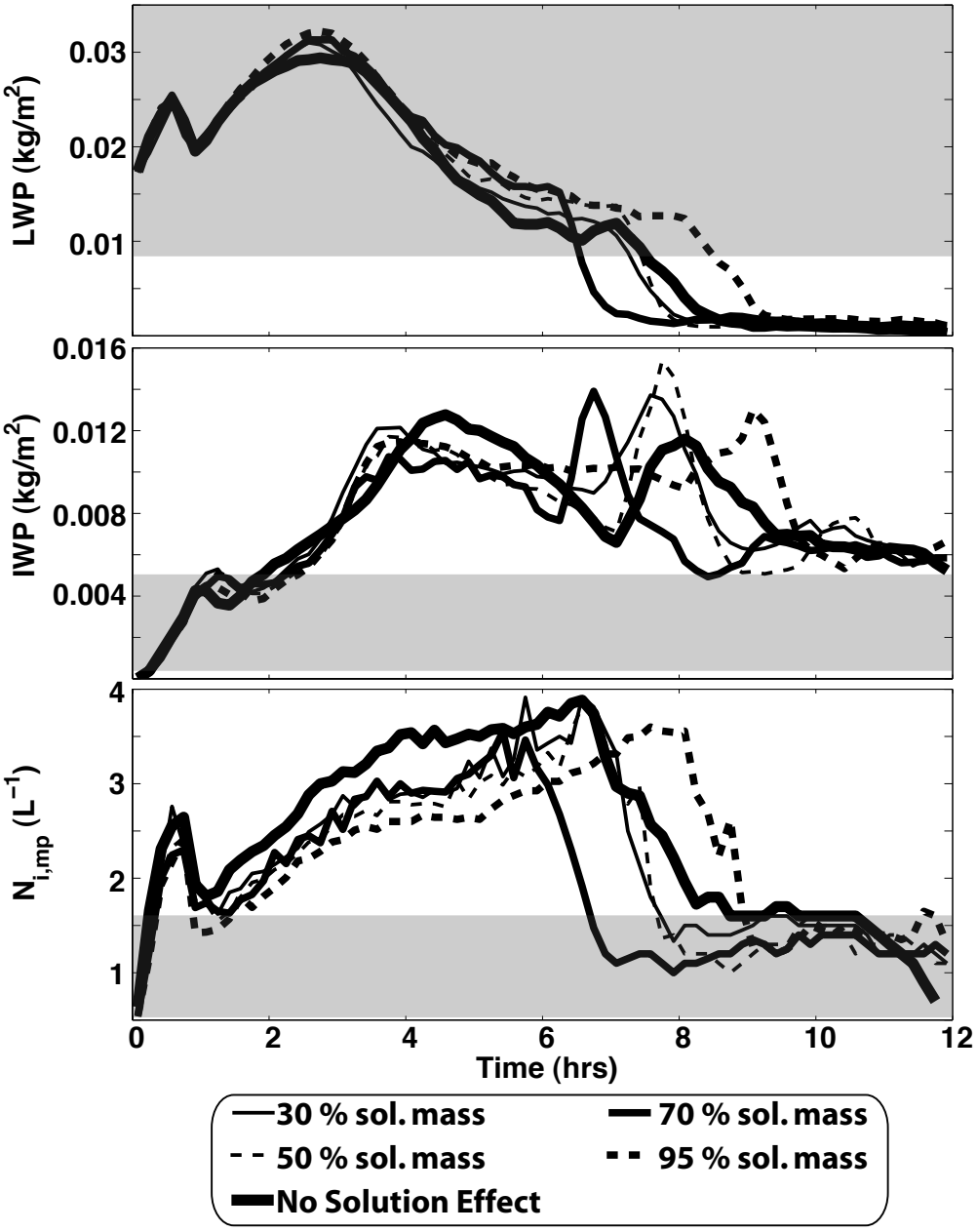

Figure 6.16: Liquid water path (top), ice water path (middle) and mean in-cloud ice particle number density (bottom) for simulations featuring different aerosol soluble mass fractions. The ranges of retrieved estimates are shown using the gray boxes.

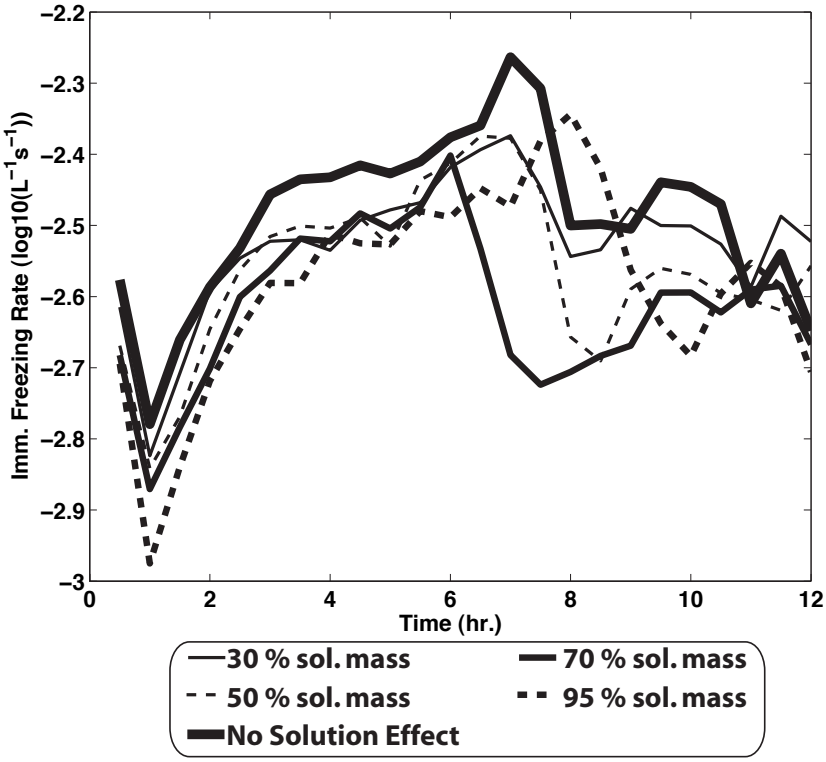

Figure 6.17: Mean rate of immersion freezing within the mixed-phase layer ($q_c > 0.01$ gkg^{-1}) with time for simulations featuring different aerosol soluble mass fractions.

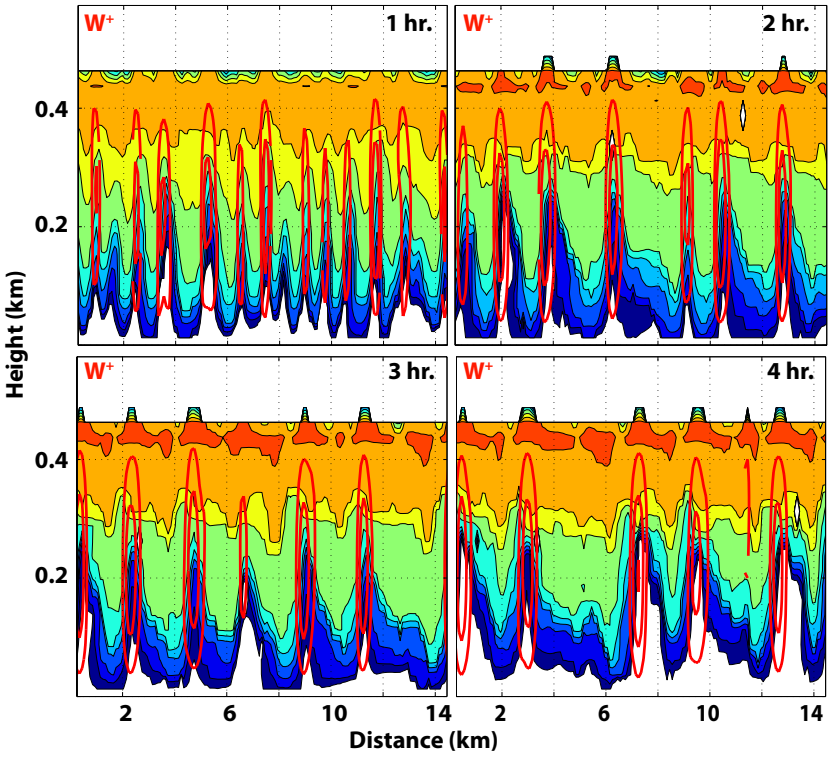

Figure 6.18: Immersion freezing rate (colored shading) and positive vertical motion (red contours) at 1, 2, 3, and 4 hours into the simulation with only immersion freezing active (CCN: Kaolinite + 70% soluble mass). Vertical velocity is contoured at 0.5, 1 and 1.5 ms^{-1} (only positive values). Simulated negative vertical velocities were of comparable strength and situated in between updrafts.

only simulation shows that there is correlation between enhanced immersion freezing rates and the position of updrafts, particularly early on in the simulation (Figure 6.18). As the simulation continues, however, elevated immersion freezing rates appear to occur above both upward and downward vertical motion.

In order to better understand why elevated levels of immersion freezing are found over downdraft regions, contributions to immersion freezing rates of pure water droplets (from eq. 6.1) by changes in drop size and temperature are analyzed for approximate temperature and drop radius ranges found in this cloud (Figure 6.19). It becomes apparent that temperature changes can strongly modulate the immersion freezing rate. This effect is not as

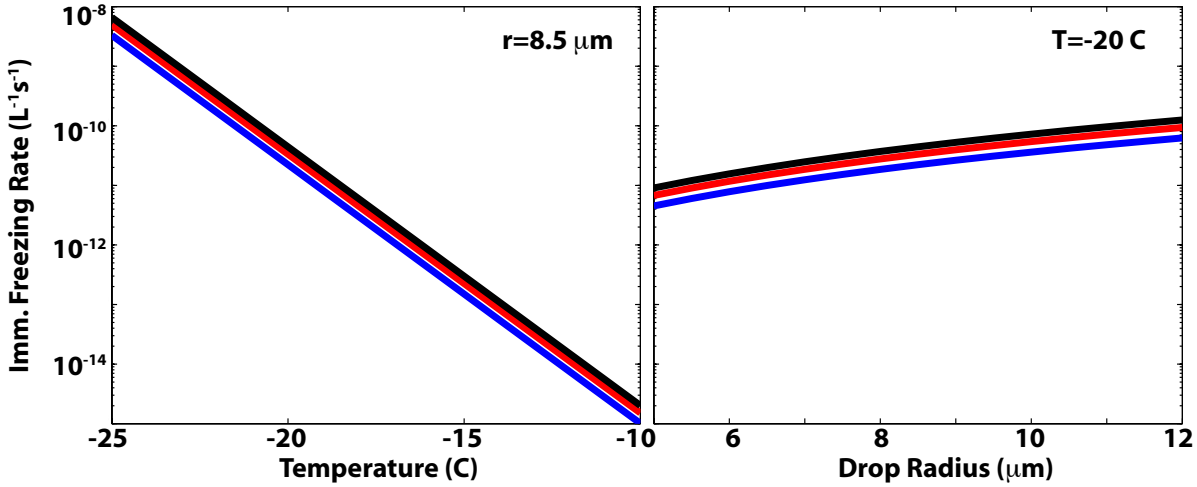

Figure 6.19: A comparison of the influence on immersion freezing rate of temperature (left) and droplet radius (right) for a pure water droplet. Rates are calculated for 250 cm^{-3} droplets, assuming kaolinite as the insoluble mass, a cooling rate of 100 (blue), 150 (red) and 200 (black) $Kday^{-1}$ (comparable to radiative cooling rates) and the drop radii and temperatures provided in the figures.

large as the solution effect, which would require consideration of both of these curves, since the size-controlled solution would effectively lower the freezing temperatures plotted here. Nevertheless, given droplets of a certain size and concentration, changes in temperature can modulate the freezing rate.

A closer analysis of the region over a downdraft shows a local minimum temperature located directly in between the two updrafts (Figure 6.20). This decrease in temperature increases the relative humidity of the region directly over the updraft, and appears to be the result of horizontal convergence from the vertically-trapped outflow of the updrafts. The convergence of cloud mass in between updrafts results in stronger radiative cooling from the cloud top in this region, as well as increased evaporative latent cooling. Within this local temperature minimum, droplet growth occurs, and the soluble mass concentration is decreased. A review of the molality and temperature in the regions of enhanced immersion freezing shows that these appear to be the controlling factors in increased ice

production.

Additional methods for droplet spectrum broadening towards larger sizes near cloud top have been suggested in the literature. The idea of spectral broadening enhanced by shear-induced mixing was introduced by Pobanz et al. (1994). However, this is unlikely in this particular scenario because there is very limited wind shear at cloud top. Work completed by Korolev and Isaac (2000) investigates influences of mixing on supersaturation levels at isobaric surfaces, stating that regions of enhanced supersaturation caused by this mixing may be responsible for broadening of cloud droplet spectra. This mechanism is particularly strong in stratiform clouds near the cloud top inversion due to strong temperature gradients in this region. However, the temporal and spatial scales presented for this mechanism are significantly smaller than what is resolvable in the current simulations. In the end, many of the processes causing broadening of cloud droplet size distributions, particularly through mixing of air parcels, are not well understood (Rasmussen et al., 2002). However, the simulations illustrate both isobaric cooling through cloud-top radiation and evaporation from cloud mixing ratio maxima, along with cooling through expansion in updrafts. These two combine to create increases in cloud droplet size and decreases in temperature that result in elevated immersion freezing rates near cloud top over both up and downdrafts.

With ice nucleating across most of the top of the cloud layer, higher radar reflectivities observed in regions of upward vertical motion using the MMCR (Chapter 4) do not necessarily appear to be due to locally higher ice nucleation levels. However, it is important to remember that radar measurements are not directly sensitive to the number of ice particles, but rather to their average volume squared. Therefore, it is possible to have smaller numbers of large ice particles within updrafts result in elevated values of radar reflectivity. To assess whether this is the case for these clouds, ice particle number density is plotted by habit (Figure 6.21, top). From this analysis, it becomes evident that at this point in the

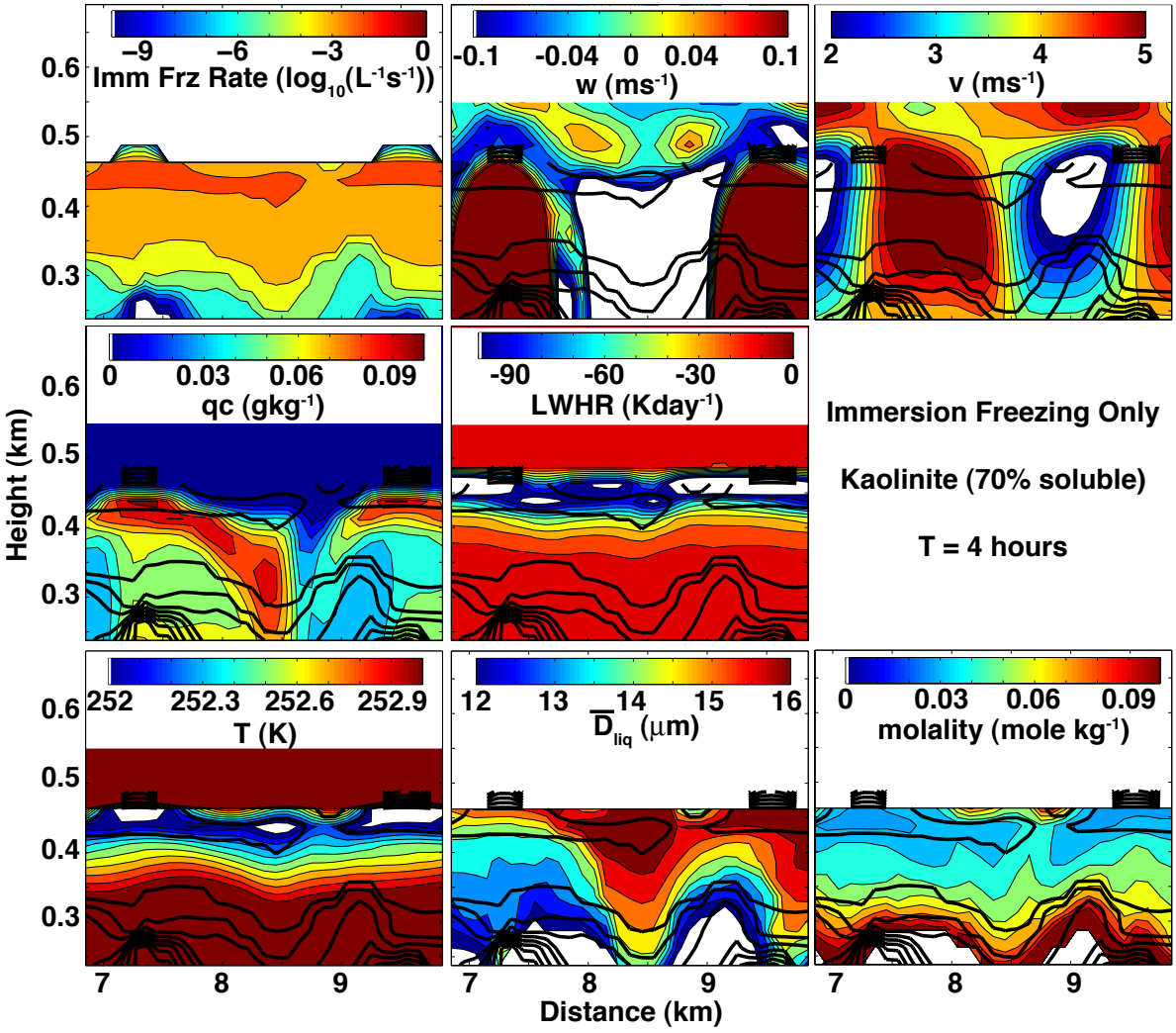

Figure 6.20: Properties for the area at cloud top between two updrafts. Immersion freezing rate is contoured over all plots in black except its own.

Table 6.1: Values of freezing efficiency from Diehl and Wurzler (2004)

Particle Type	**$B_{h,I}$ ($cm^{-3}s^{-1}$)**
Bacteria	6.19
Leaf Litter	4.38×10^{-1}
Pollen	1.01×10^{-2}
Montmorillonite	3.23×10^{-5}
Kaolinite	6.15×10^{-8}
Soot	2.91×10^{-9}

simulation the majority of the particles are in the form of pristine crystals or rimed crystals, with lesser contributions to total ice concentration by graupel, and rimed and unrimed aggregates. However, an analysis of the simulated radar reflectivity (Figure 6.21, bottom) reveals little correlation between the locations of the highest particle number concentrations and the highest reflectivities. Rather, graupel and rimed mass (particles with higher volumes) provide the largest contributions, and are mainly found in the updrafts.

Finally, composition of the insoluble portion of the aerosol affects freezing temperature as well (e.g. Diehl and Wurzler, 2004). This effect is included in simulated immersion freezing calculations through the ice nucleating efficiency term ($B_{h,i}$). Examples of ice nucleating efficiencies provided by Diehl and Wurzler (2004) are presented in Table 6.1. Figure 6.22 nicely illustrates combined effects of solution concentration and insoluble mass properties, with less concentrated droplets freezing at warmer temperatures. To better understand the effect of insoluble mass type, simulations were completed for aerosol particles including kaolinite, illite, montmorillonite and soot. For all of these simulations, aerosol soluble mass fraction was held at 70%, as prescribed for the SHEBA intercomparison case. In addition, a simulation utilizing the original Bigg (1953) parameterization was completed. Here, the freezing efficiency parameter (B) is 10^{-4} $cm^{-3}s^{-1}$ and A is $0.66\,^{\circ -1}$, and no freezing point depression due to aerosol soluble mass fraction is calculated.

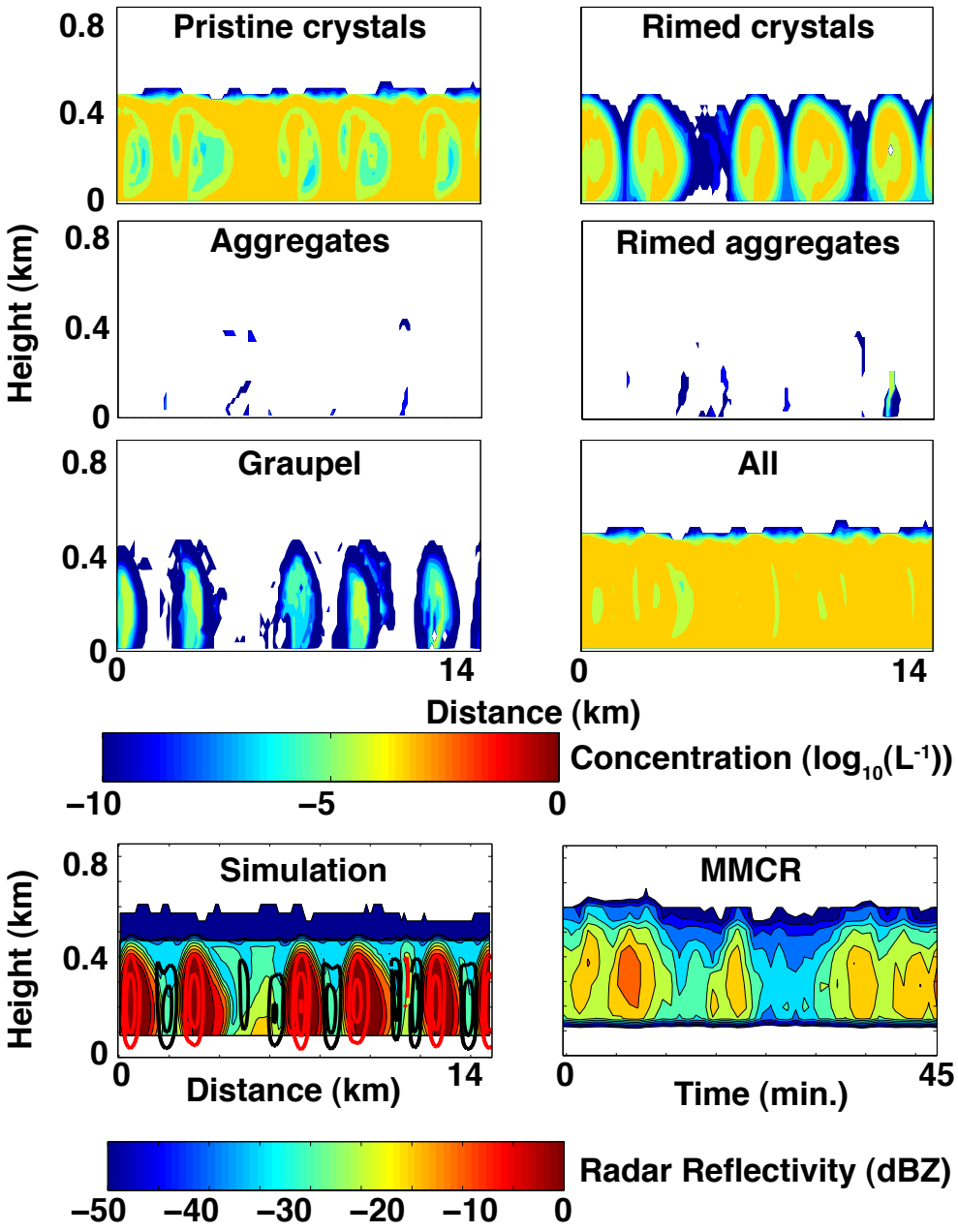

Figure 6.21: Ice particle number concentrations separated by habit (top) and simulated and observed radar reflectivity (bottom) from the immersion freezing only (Kaolinite, 70% soluble mass) simulation. Vertical velocity is contoured in red (+ 0.5, 1, 1.5 ms^{-1}) and black (- 0.5, -1, -1.5 ms^{-1}) along with the simulated reflectivity.

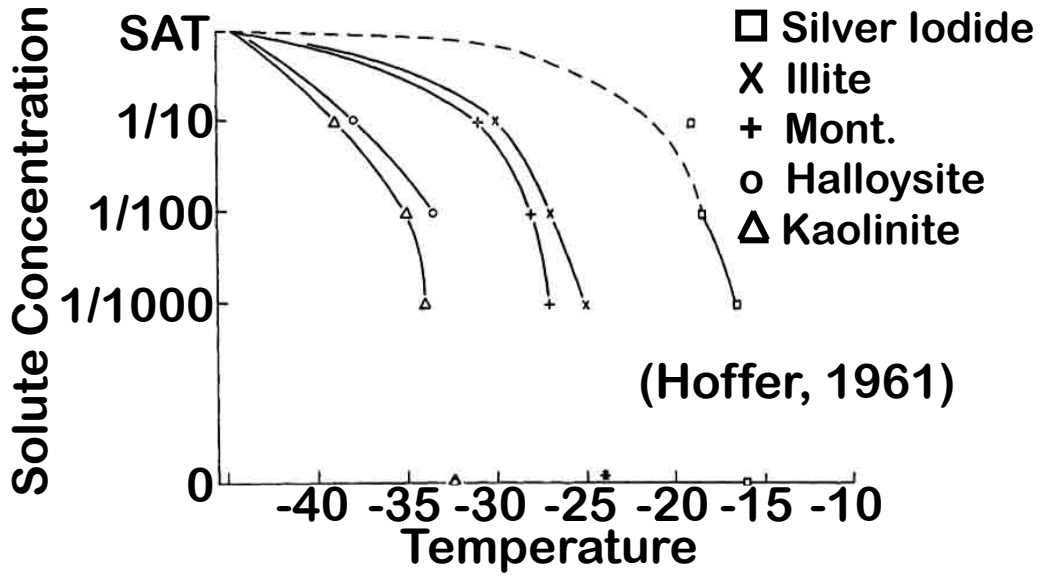

Figure 6.22: Median droplet freezing temperature for droplets of different solute concentrations (100-120 μm diameter) (from Hoffer, 1961).

Figure 6.23 illustrates the effect of varying insoluble mass types on simulated liquid and ice water paths as well as on mean ice particle concentration. Illite and montmorillonite both allow for early initiation of droplet freezing via the immersion mode, even at very small sizes, resulting in the freezing of a large number of droplets. Correspondingly, liquid water paths for these simulations are quickly reduced to near zero, resulting in a completely glaciated cloud. Kaolinite allowed for a longer cloud lifetime but still allows for sufficient ice production to glaciate the cloud at approximately seven hours into the simulation. Soot particles appear to have a significantly smaller impact, only allowing for development of a small amount of ice after the 12-hour simulation. This results in a significant overestimation of liquid water. Finally, utilization of the Bigg parameterization results in ice being produced very early in the simulation. However, the ice mass produced in this simulation is limited, and the cloud is glaciated more slowly than with the illite, and montmorillonite simulations.

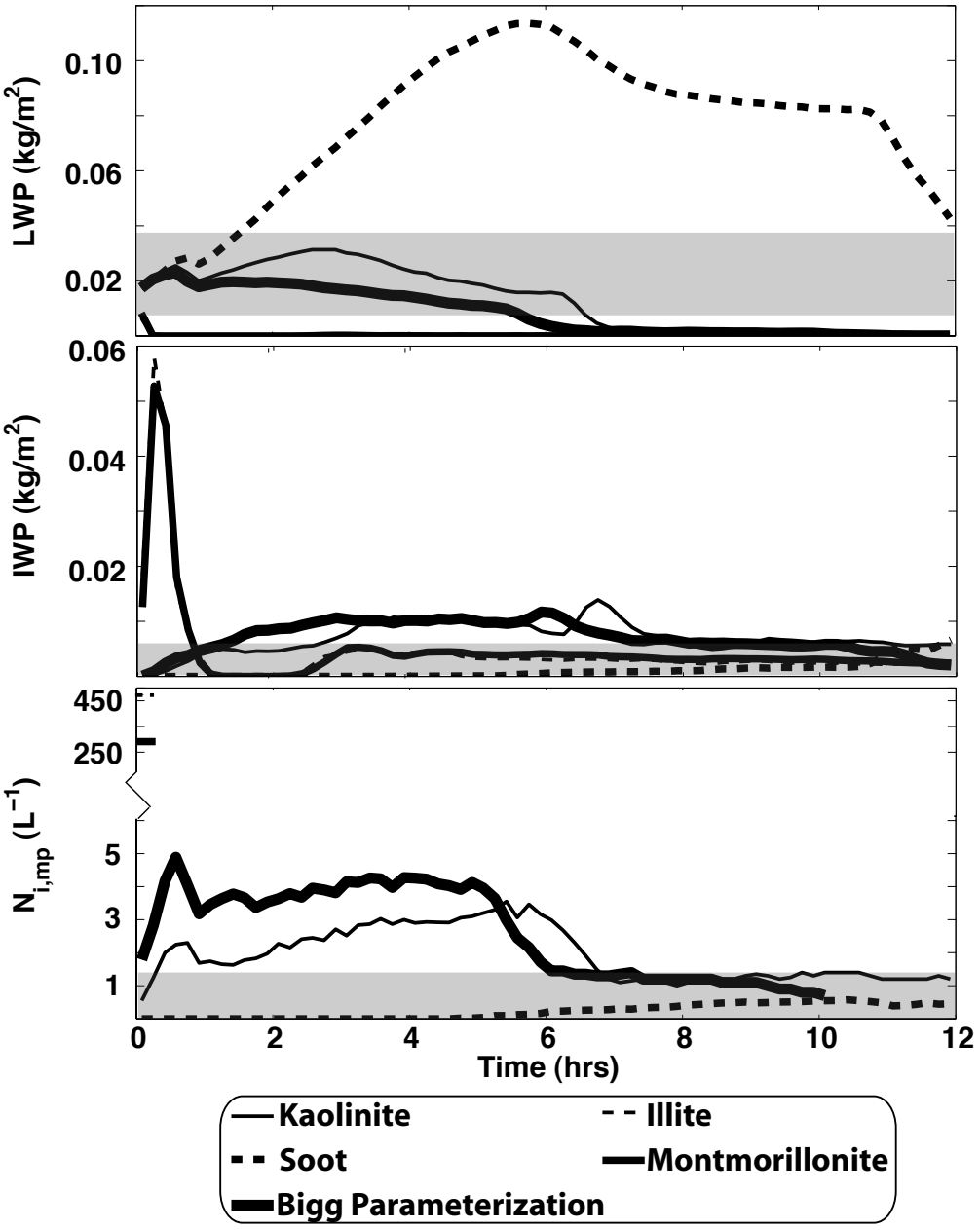

Figure 6.23: Liquid water path (top), ice water path (middle) and mean in-cloud ice particle number density (bottom) for simulations featuring different aerosol insoluble mass types. The ranges of retrieved estimates are shown using the gray boxes.

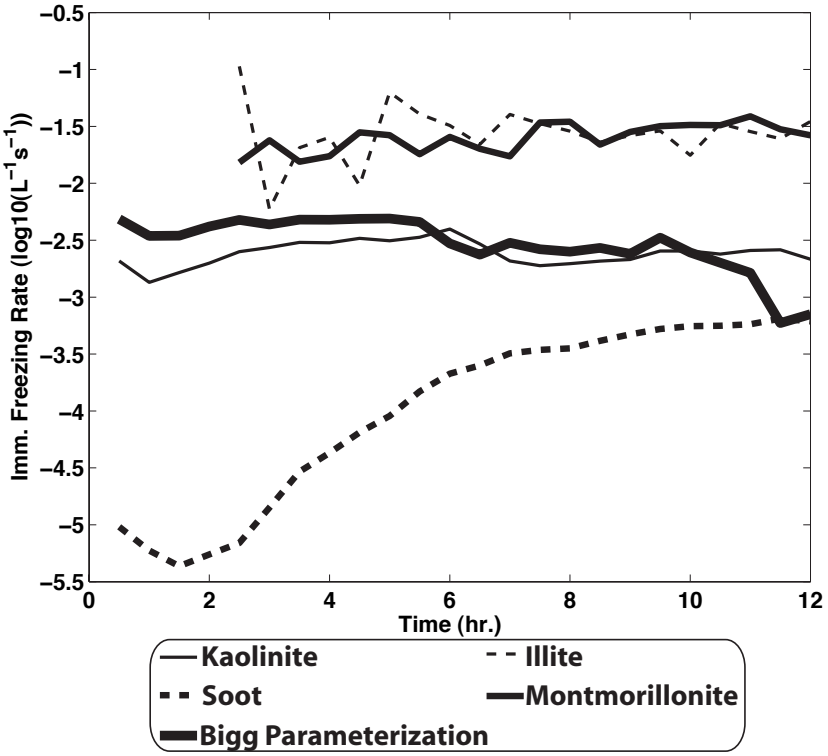

Figure 6.24: The mean rate of immersion freezing within the liquid cloud layer ($q_c > 0.01$ gkg^{-1}) with time for simulations featuring different aerosol insoluble mass types.

The corresponding influence of different insoluble mass types on ice formation rates through the immersion mode is reviewed in Figure 6.24. Simulations assuming illite or montmorillonite insoluble mass types result in relatively high rates of immersion freezing within the cloud layer. Simulations completed with kaolinite and the Bigg parameterization, also yield comparable (but lower) immersion freezing rates throughout the simulation. Finally, freezing rates obtained assuming soot were substantially lower (note the logarithmic scale) than those from the other simulations, but increased with time, likely due to activation and growth of additional liquid droplets.

Figure 6.25 illustrates differences in immersion freezing rates at different droplet sizes for simulations featuring varying insoluble mass types. Significant differences are illustrated. Most noticeably, the simulations assuming illite and montmorillonite feature high immer-

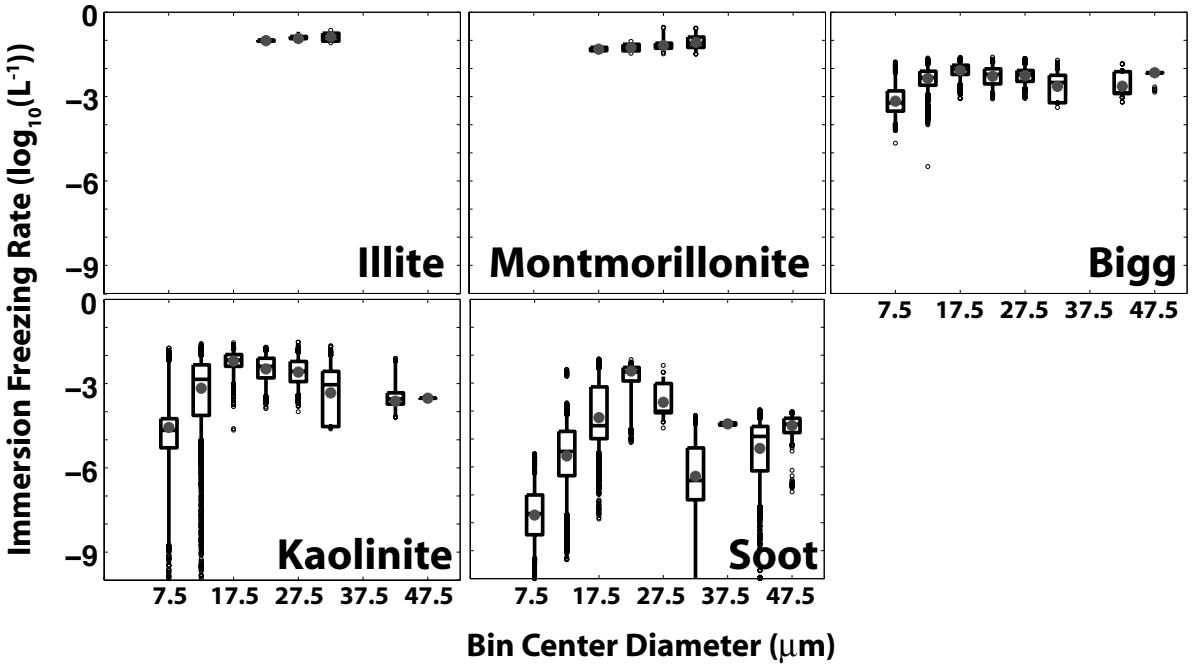

Figure 6.25: The distribution of immersion freezing rate within the liquid cloud layer (q_c > 0.01 gkg^{-1}) over ten liquid droplet size bins for simulations featuring different aerosol insoluble mass types. The boxes represent the interquartile range (IQR), with the line in the center representing the median value, and whiskers illustrating the IQR +/- 2xIQR. Circles are representing outliers (> IQR +/- 2xIQR). The mean values are represented by the gray dots.

sion freezing rates across relatively small size ranges. Because these simulations very rapidly glaciate the cloud, the droplet population does not evolve as far as in other simulations. The simulation assuming soot is shown to have smaller immersion freezing rates across the size spectrum, and particularly so at smaller droplet sizes. The Bigg parameterization allows for a relatively narrow range of immersion freezing rates, but does so across a wide range of droplet sizes. Also, removal of the solution effect with the Bigg simulations is evident, with higher immersion freezing rates at small droplet sizes.

6.2.2.4 Realistic simulation

From the previous chapters and sections, much has been learned about the structure of and processes governing mixed-phase stratiform cloud formation and maintenance. Here, some of this information is utilized to attempt to realistically simulate this type of cloud structure.

First, it is unrealistic to believe that immersion freezing is the only active nucleation mechanism within these clouds. There are likely some aerosol particles composed mainly of insoluble mass that would act as very good IN in condensation and deposition nucleation modes. One of the challenges faced in trying to simulate this partitioning of ice nucleation lies in how IN concentrations are assigned in the simulation. Typically, estimates of these concentrations are provided from Continuous Flow Diffusion Chamber (CFDC) measurements. According to the instrument operators, the CFDC can measure aerosol particles which induce deposition, condensation and immersion nucleation. In AMPS, however, aerosol particles involved with immersion freezing come from the CCN category, since a droplet must be formed first. Therefore, a straightforward assignment of the CFDC-measured values will result in a double-counting of ice produced through the immersion mode: First from the contribution to the CFDC IN measurements, which will now contribute to simulated condensation and deposition freezing, and second from simulated immersion freezing, which is drawing from the CCN aerosol component. Therefore, IN concentrations should be reduced from CFDC measurements when used in simulations which separately predict condensation/deposition and immersion freezing. The amount by which they must be scaled can not readily be determined at this time, and likely varies from case to case.

As shown in the previous section, a second important consideration is the composition of the insoluble mass type within CCN, as it will have a significant effect on the freezing efficiency

of the liquid droplets in which they are embedded. As mentioned earlier, Leaitch et al. (1984) speculated insoluble mass inside CCN observed in Canada's Northwest Territories likely consisted of soot and clay particles. Both Hara et al. (2003) and Yamanouchi et al. (2005) measured soot as a major constituent in both Arctic haze and background aerosol, and Koch and Hansen (2005) utilized a large-scale model to illustrate several pathways of soot transport to the Arctic from mid and even tropical latitudes.

In order to most accurately represent these ideas within the SHEBA framework, four simulations with both immersion and condensation/deposition freezing active were completed. Two of these, completed with $0.52L^{-1}$ and 0.17 L^{-1} IN concentrations and kaolinite as the insoluble mass type, were discussed at the beginning of this chapter. In addition, similar simulations using soot as the insoluble particle type were completed. The liquid and ice water paths from these simulations, along with ice particle number densities are shown in Figure 6.26.

Of these four simulations, only the one assuming 0.17 L^{-1} IN with soot as a part of CCN maintained a liquid water cloud consistent with observations at the end of 12 hours of simulation. This simulation was extended to 24 hours. The liquid and ice water paths and mean ice particle number density from this 24 hour simulation are shown in Figure 6.27. Ice growth appears to occur in reaction to liquid water path, with increases in liquid water path resulting in corresponding increases in ice particle number density and IWP. During much of the simulation (from 5-17 hours), the IWP maintains a value between 3 and 5 x 10^{-3} kgm^{-2}, falling within the upper range of retrieved estimates. During this time period, simulated liquid water path slowly decreases within the observed range. Toward the end of the simulation, ice production increases in reaction to a small increase in LWP.

Because soot was assumed as the insoluble mass fraction, immersion freezing was limited. Despite this, the percentage of ice produced through immersion freezing remains significant

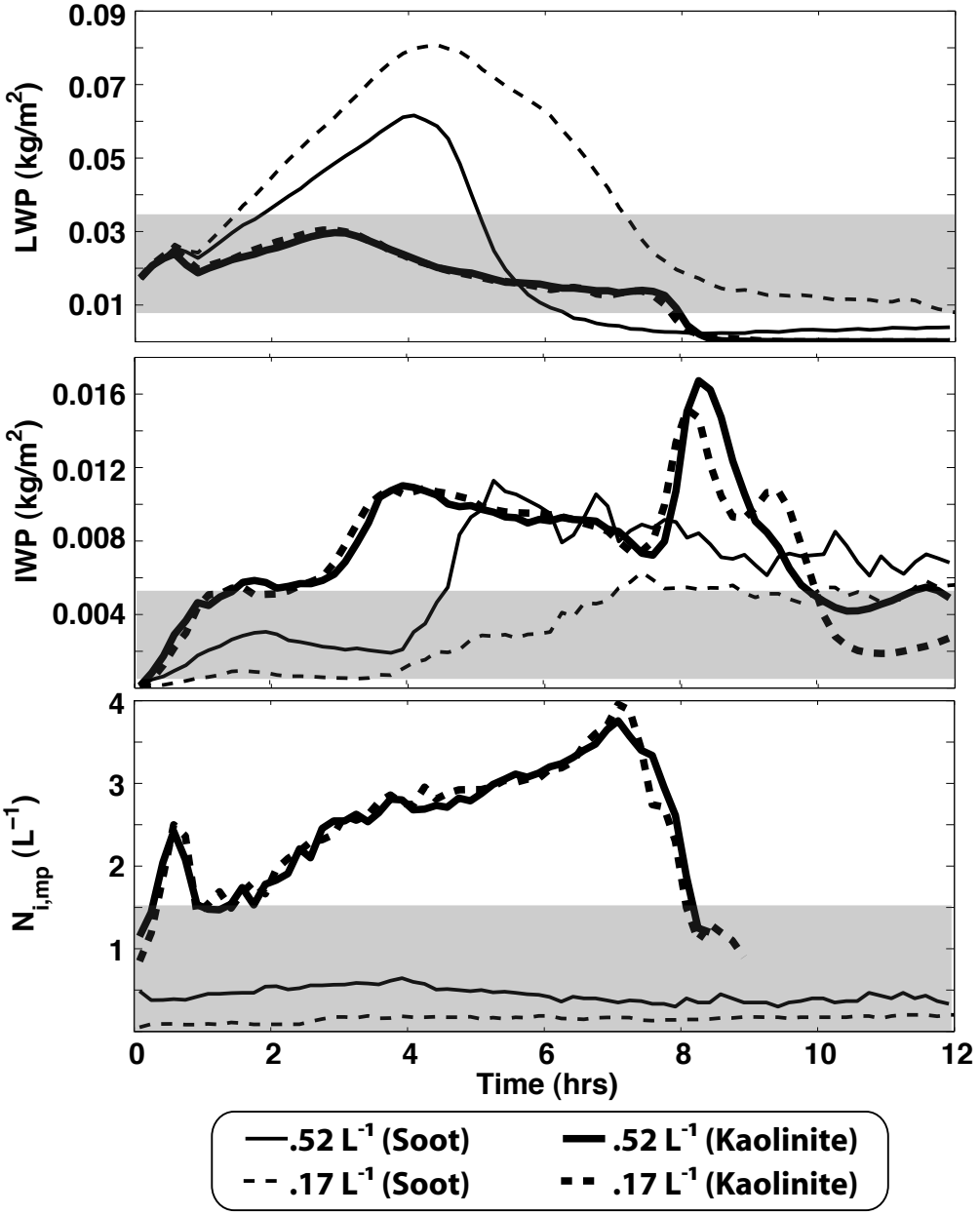

Figure 6.26: Liquid water path (top), ice water path (middle) and mean in-cloud ice particle number density (bottom) for simulations featuring both immersion and condensation/deposition freezing. The ranges of retrieved estimates are shown using the gray boxes.

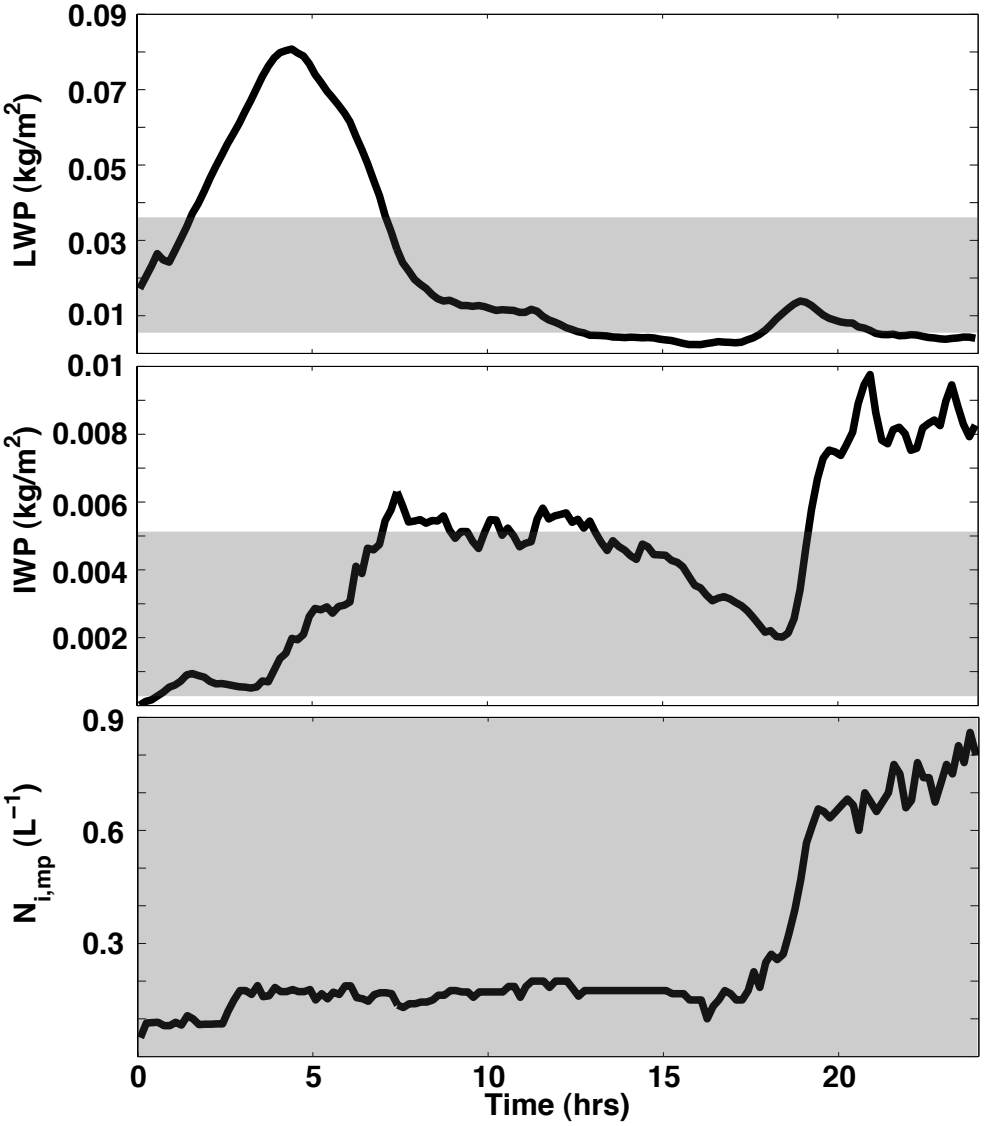

Figure 6.27: Liquid water path (top), ice water path (middle) and mean in-cloud ice particle number density (bottom) for 24 hours of a simulation using a 0.17 L^{-1} IN concentration and soot as the insoluble mass type within CCN. The ranges of retrieved estimates are shown using the gray boxes.

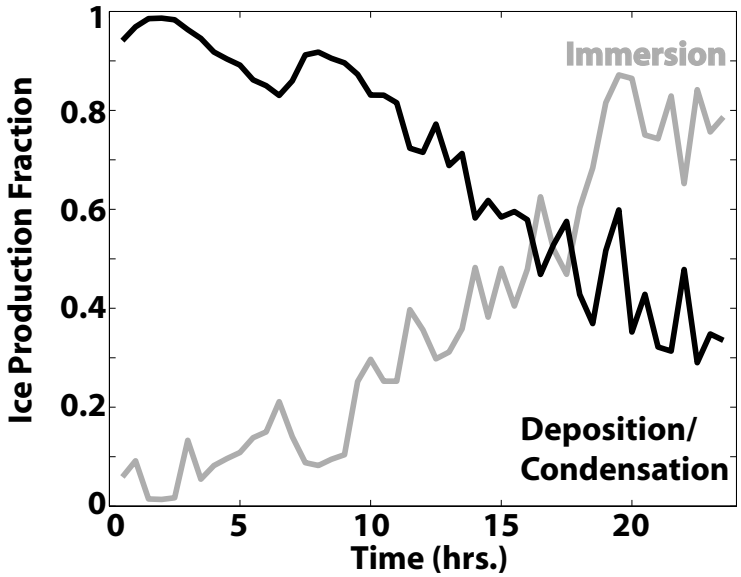

Figure 6.28: The percentage of the total ice production rate contributed to immersion (gray) and deposition/condensation (black) freezing for the 0.17 L^{-1} IN/Soot simulation.

compared to that produced via deposition/condensation freezing (Figure 6.28). To evaluate the structure of the simulated cloud, simulated lidar and radar products were produced at 15 hours into this simulation (Figure 6.29). From these figures, a visual representation of the model liquid and ice fields is produced. Liquid, which produces the largest amount of scattering in the simulated lidar product is located relatively uniformly across the domain, with a cloud base between 250-300 meters, and cloud top at around 475 meters. The periodic nature of ice precipitation locations is evident in both the lidar and radar simulations, with the simulated radar product indicating where regions of elevated ice mass are located.

6.3 Discussion on model uncertainties

Inherent in all simulated evaluations of processes are the uncertainties associated with parameterizations and assumptions made within the model dynamics, microphysics, radiation

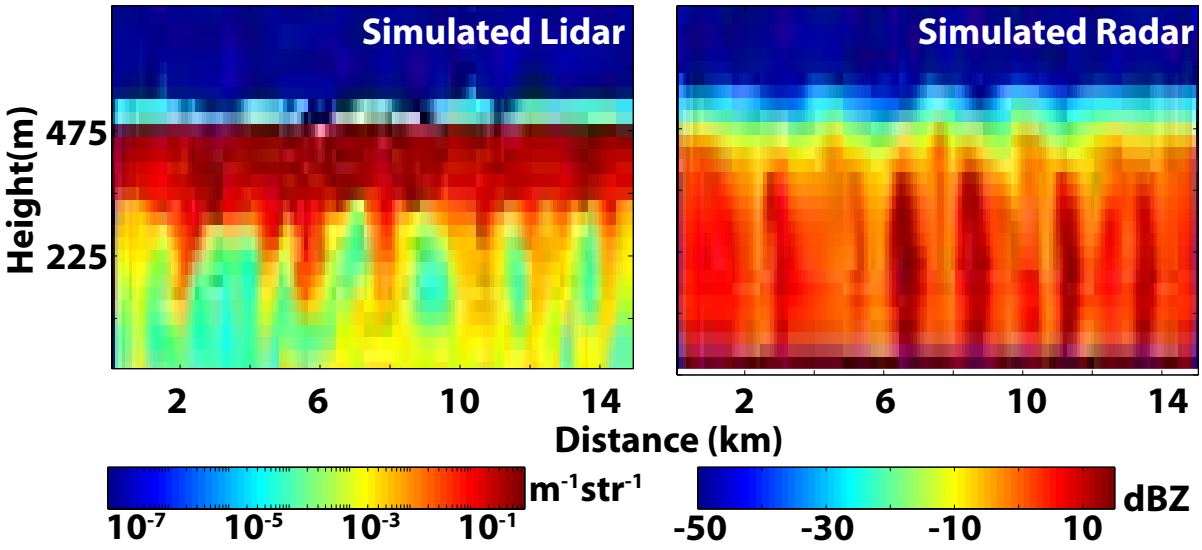

Figure 6.29: Simulated lidar backscatter cross-section (left) and radar reflectivity (right) for the 0.17 L^{-1} IN/Soot simulation at 15 hours.

and initialization. Although a full analysis of all of these uncertainties is far beyond the scope of this work, this section discusses some of the most relevant uncertainties associated with the simulations completed in this section, and with the simulation of mixed-phase stratiform cloud layers.

One factor recently discussed as a major uncertainty in the simulation of mixed-phase stratiform layers is the handling of vapor deposition and ice crystal growth within numerical models (Avramov and Harrington, 2009). Because crystal growth rate is strongly dependent upon the shape of the ice crystal, both removal of available water vapor and particle terminal velocity are as well. In addition, the fall velocity aspect presents a double whammy, because the slowest falling particles are typically also the fastest growing (dendrites). In the SHIPS simulations completed above, habit is diagnosed through evaluation of physical characteristics of the ice particles, including the axis lengths and amount of rimed and aggregated mass. Since these values are calculated explicitly, simulation of further depositional growth and particle fall velocity can be based on physical principles, and

can vary between different sized particles at any grid point. Vapor deposition is handled by Chen and Lamb (1994), with the exception that instead of only handling the a- and c-axis lengths of a spheroidal crystal, here the a-axis is divided into an a- and d- axis, with the d-axis representing dendritic growth. Particle terminal velocity can strongly modulate the lifetime of the liquid part of the cloud, as a slower-falling particle will spend more time within the mixed-phase layer, thereby removing more available moisture from that region. In SHIPS, terminal velocity is calculated using mass and habit information as obtained in the above description following the formulation of Bohm (1989). Explicit calculation of relevant parameters provides SHIPS with an advantage over traditional microphysical schemes, which assign ice crystal habits in more simplified manners, often assuming shape and size parameters based on user specified values.

A second potential source of error within these simulation stems from model initialization of aerosol particles. Both IN and CCN properties are drastically simplified within the current framework. With IN, many of the possible discrepancies stem from the assignment of IN concentrations from CFDC measurements. First, since IN number concentration is a user-assigned variable within the model, there is a constant resupply of IN at every model time step. As discussed in Chapter 2, realistically in this type of super-cooled, supersaturated (with respect to ice) environment, it is likely that uncoated IN would quickly nucleate ice crystals, which would grow and fall out of the cloud layer. This would result in a removal of available IN for further production of ice particles through deposition/condensation freezing, and not allow for a consistent resupply of IN as carried out within the simulation. Completion of simulations which treat IN concentrations prognostically would provide insight into the magnitude of errors induced through this form of IN treatment. A second potential source of uncertainty stemming from IN initialization comes from the horizontal homogeneity of IN applied within the model. Measurements from the CFDC taken outside

of the mixed-phase layer showed IN concentrations below the instrument noise floor more than 50% of the time, illustrating that even in regions where IN would not necessarily be quickly scavenged, their supply is limited. Although the mean concentration value that is used in model initialization is significantly lower than the values observed in measurements registering above the noise floor, a uniform application of this concentration to the model domain will likely have a different impact than a spatial distribution with less homogeneity.

Because these simulations were initialized with liquid water but without ice, there is a trade off in the early hours of the simulation between accurate representation of liquid water path via higher ice production rates (i.e. control simulation) and accurate ice production rates further into the simulation at the expense of an original large increase in liquid water (i.e. immersion+deposition, 0.17 L^{-1} IN). Because both can be detrimental to accurate simulation of the cloud layer, an interesting experiment for future work would be to attempt to allow the cloud to develop in entirety within the model. That way, ice particle formation would spin up with the evolution of the liquid water droplet distribution. This would likely reduce the overestimation of liquid water early in the simulation.

A more realistic portrayal of CCN properties may too influence mixed-phase stratiform cloud lifecycle. In particular, providing a distribution of aerosol soluble mass fractions, rather than limiting this to one distinct value would likely lead to a more realistic simulation. This would strongly affect immersion freezing, since some cloud droplets would have significantly higher amounts of insoluble mass than others, allowing them to freeze more readily.

Due in part to the computational expense of running the Advanced Microphysical Prediction System, the simulations in this work were all completed in two dimensions. Although this was deemed to be appropriate due to the horizontal homogeneity of these stratiform

clouds, there are some aspects of the results that may be altered by expanding to three dimensions. First, the accumulation of cloud mass in between updrafts that resulted in localized regions of enhanced immersion freezing with increased radiative cooling may be reduced via horizontal dispersion within this region if simulated in three dimensions. This would reduce the amount of ice nucleated within the simulation. A second potential effect of converting to three-dimensional simulation would be the increase of cloud edge locations. Both radiative and evaporative processes at the cloud edge could lead to localized cooling. However, due to the high latitude of the currently studied phenomenon, and the low sun angle involved, three dimensional radiative effects in the short wave are considered to be minimal.

Chapter 7

Summary and future work

In this work, several observational and modeling tools were utilized to gain insight into the lifecycle of mixed-phase stratiform clouds commonly observed in the Arctic. First, a multiyear dataset of single-layer mixed-phase startiform cloud observations was developed using several instruments. From this study and others, it is clear that Arctic Mixed-phase clouds occur frequently. In addition, this dataset contains information on cloud mean macro- and microphysical characteristics, and a comparison between measurements at several Arctic locations is provided. This is done directly between measurements from Eureka, Canada and Barrow, AK, as well as indirectly with results from previous studies at various locations. A summary of mean macro- and microphysical properties for these clouds, along with key findings is presented below. Again, mean values reported here exclude outliers as described in Chapter 4.

- Single-layer mixed-phase clouds occurred with a frequency of 26% at Barrow during fall of 2004, and a mean frequency of 8% at Eureka. Multi-layer cases are not included here, and there were significant variations in frequency by season.

- Fall clouds observed at Barrow had a mean cloud base height of 688 m, mean thickness of 650 m, and occurred at temperatures between 249 and 263 K.

- Fall Barrow clouds had a mean retrieved effective diameter of 47 μm, likely due largely to ice contamination of the lidar-radar retrieval. The mean retrieved number density was 2.8x10^4 L^{-1}, mean retrieved TWC was 0.28 gm^{-3}, mean retrieved IWC was 0.04 gm^{-3} and the mean retrieved LWP was 106 gm^{-2}.

- Precipitation from the clouds observed at Barrow had a mean retrieved effective diameter of 123 μm, mean retrieved number density of 16 L^{-1}, and a mean retrieved IWC of 0.03 gm^{-3}.

- Clouds observed at Eureka had a mean cloud base altitude of 1720 m, mean thickness of 338 m, and occurred at temperatures between 240 and 272 K.

- Eureka clouds had a mean retrieved effective diameter of 24 μm, mean retrieved number density of 8.6x10^4 L^{-1}, a mean retrieved TWC of 0.09 gm^{-3}, a mean retrieved IWC of 0.004 gm^{-3} and a mean retrieved LWP of 38 gm^{-2}.

- Precipitation from clouds observed at Eureka had a mean retrieved effective diameter of 93 μm, mean retrieved number density of 9 L^{-1}, and a mean retrieved IWC of 0.006 gm^{-3}.

- Liquid fraction is shown to decrease with decreasing temperature.

- Seasonal mean LWCs and IWCs appear to change in phase with one another; Seasons with high LWCs also had higher IWCs.

- Barrow clouds typically are lower and thicker, with higher water contents than those found at Eureka.

Utilizing information gathered from the observations described above, along with that from literature review, a conceptual model for immersion freezing in mixed-phase stratus clouds was developed. This model explains the persistence of mixed-phase clouds through self-limitation of ice nucleation in any given point in the cloud, and is based on the freezing point depression induced by relatively high concentrations of soluble material inside cloud droplets. Necessary conditions for the formation of these activated supercooled droplets with high molality include:

- A supersaturation with respect to water of 0.1-1%
- Larger aerosol particles (radii of 0.2-0.4 μm)
- Large soluble fractions (60%+ by mass) of the initial aerosol particle

The presented conceptual model also helps to explain recent observations of some characteristics of mixed-phase stratus, including their long lifetime and the spatial variability of ice production.

In order to test this theory, a variety of numerical simulations were completed. These simulations were focused on ice nucleation via immersion freezing, and did not necessarily address the influences of ice crystal depositional growth rates or particle fall velocities. The vast majority of simulations completed resulted in complete glaciation of the liquid cloud layer within the 12 hour simulation period. This occurred even when ice nucleation through deposition/condensation freezing was limited to match measured ice concentrations. Inclusion of immersion freezing resulted in similar results, and only a reduction of the production of ice through deposition/condensation nucleation to a maximum of 1/10 the observed ice concentrations allowed for prolonged maintenance of a liquid layer.

Comparison of ice production rates through multiple modes of nucleation showed that *immersion freezing produced a large fraction of ice as compared to deposition/condensation*

freezing. Given the conditions imposed on the nucleation of ice via deposition/condensation freezing, it is impossible to quantitatively say how much more ice is produced via immersion freezing. However, it is certain that the rates of immersion freezing and deposition/condensation freezing are at least equal when the ratio of the two approaches one. In addition, although ice formed via the deposition/condensation mode may be reduced, there are several reasons to believe production of ice from "free" (non-coated) IN should be limited, as discussed in the previous chapter. How to best perform this limitation is beyond the scope of the current effort, and is left for future studies.

An analysis of the effects of CCN properties on cloud lifetime was completed. *Aerosol soluble mass fraction was found to influence the initiation of freezing via the immersion mode by requiring droplet growth to larger sizes when soluble mass fraction was increased.* These larger droplets were found to form near cloud top in simulations completed with the immersion freezing mode. Originally, these droplets were hypothesized to grow through expansion within updrafts. *This hypothesis was shown to correctly predict the location of elevated immersion freezing rates*. However, completed simulations also revealed that particles were nucleated via immersion freezing over downdrafts. The downdraft nucleation regions were shown to be the result of isobaric radiative cooling near the cloud top, which resulted in a colder and more humid environment. Despite ice particles nucleating throughout the upper portions of cloud layers, simulated radar reflectivity features maximum values in regions of ascent, similar to observations. This occurs because of the large volume of the particles growing in and falling out of the updrafts, many of which have been rimed during their extended lifetime within the super cooled liquid layer.

In addition to soluble mass fraction, *CCN insoluble mass type was also found to have a large influence on freezing via the immersion mode.* Droplets forming on aerosol particles containing insoluble fractions with high freezing efficiencies (e.g. illite, montmorillonite)

froze at smaller sizes than those containing particles with lower freezing efficiencies (e.g. kaolinite, soot). This effect was found to be more influential than that imposed by the aerosol soluble mass fraction.

There are several aspects of this study which can benefit greatly from improved measurement tools and methods as well as further theoretical study. Primarily, challenges remain in the correct retrieval of cloud properties. In particular, bimodal particle size distributions inside the mixed-phase cloud layer provide a challenging environment for many retrieval algorithms. The extent and impact of uncertainties in the data and retrieval methods are presented throughout this manuscript. The most notable uncertainties lie in the characterization of liquid droplet size and number density. Improved retrieval methods, potentially utilizing particle fall velocities, as well as additional instruments such as microwave radiometers and interferometers would aid in better characterization of cloud liquid. Additionally, improved spatial coverage through additional long-term observational sites as well as satellite measurements will aid in improving our understanding of differences observed in cloud properties among different Arctic locations. New active remote sensing platforms with improved measurement capabilities are being developed, and will aid in future findings about these clouds. Another instrument suite that would be of great assistance in the study of these cloud structures are in-situ sensors that can distinguish between ice nucleation types. A better understanding of the mechanisms responsible for ice formation would be of great use in improving our understanding of cloud lifetime. Finally, focused studies such as the recently completed Indirect and Semi-Direct Aerosol Campaign (ISDAC) will help to provide high resolution information useful understanding the processes involved in maintaining these clouds.

With regard to simulation, continued improvement in ice nucleation parameterizations is necessary. Commonly used current algorithms appear to over predict ice formation, and

are usually based on mid-latitude aerosol and cloud properties. Development of parameterizations designed specifically for high latitudes would likely have significant impacts on the simulation of mixed-phase cloud layers. Further studies of interest include the inclusion of contact nucleation as well as simulations which handle ice nucleus concentrations prognostically. These types of simulations can provide further insight into the evolution of spatial distributions of ice forming aerosols. Additionally, investigations addressing the variety of parameterizations of ice crystal growth rates and fall velocities are currently being completed, and should be pursued to determine the effect of the evolution of ice mass within simulations.

It is believed that this research will contribute to our understanding of mixed-phase cloud microphysics, and provide insight into one potential pathway for ice formation within these layers. In the end, it is likely a combination of nucleation mechanisms that contribute to ice production and maintenance of the balance of phases. This work shows that immersion freezing should be strongly considered amongst these mechanisms, and that future studies should evaluate any potential connections to immersion freezing in their results.

Bibliography

Abdul-Razzak, H., S. Ghan, and C. Rivera-Carpio, 1998: A parameterization of aerosol activation. 1: Single aerosol type. *J. Geophys. Res.*, **103**, 6123–6132.

Ackerman, S. and G. Stephens, 1987: The absorption of solar radiation by cloud droplets: An application of anomalous diffraction theory. *J. Atmos. Sci.*, **44**, 1574–1588.

Avramov, A. and J. Harrington, 2009: The influence of parameterized ice habit on simulated mixed-phase Arctic clouds. *J. Geophys. Res.*, **Submitted**.

Bernard, J. and C. Long, 2004: A simple empirical equation to calculate cloud optical thickness using shortwave broadband measurements. *J. Appl. Meteor.*, **43**, 1057–1066.

Bertram, A., T. Koop, L. Molina, and M. Molina, 2000: Ice formation in $NH_4 2SO_4$-H_2O particles. *J. Phys. Chem.*, **104**, 584–588.

Bigg, E., 1953: The formation of atmospheric ice crystals by the freezing of droplets. *Quart. J. Roy. Meteor. Soc.*, **79**, 510–519.

Bigg, E. and C. Leck, 2001: Cloud active particles over the central Arctic Ocean. *J. Geophys. Res.*, **106**, 32 155–32 166.

Blanchet, J.-P. and E. Girard, 1994: Arctic 'greenhouse effect'. *Nature*, **371**, 383–383.

Bohm, H., 1989: A general equation for the terminal fall speed of solid hydrometeors. *J. Atmos. Sci.*, **46**, 2419–2427.

Bromwich, D., J. Cassano, T. Klein, T. Heinemann, K. Hines, K. Steffen, and J. Box, 2001: Mesoscale modeling of katabatic winds over Greenland with the polar MM5. *Mon. Wea. Rev.*, **129**, 2290–2309.

Brownscombe, J. and N. Thorndike, 1968: Freezing and shattering of water droplets in free fall. *Nature*, **220**, 687–689.

Chen, J.-P. and D. Lamb, 1994: The theoretical basis for the parameterization of ice crystal habits: Growth by vapor deposition. *J. Atmos. Sci.*, **51**, 1206–1222.

Chen, Y., P. De Mott, S. Kreidenweis, D. Rogers, and D. Sherman, 2000: Ice formation by sulfate and sulfuric acid aerosol particles under upper tropospheric conditions. *J. Atmos. Sci.*, **57**, 3752–3766.

Clothiaux, E., T. Ackerman, G. Mace, K. Moran, R. Marchand, M. Miller, and B. Martner, 2000: Objective determination of cloud heights and radar reflectivities using a combination of active remote sensors at the ARM CART sites. *J. Appl. Meteor.*, **39**, 645–665.

Cotton, W., G. J. Tripoli, R. Rauber, and E. Mulvihill, 1986: Numerical simulation of the effects of varying ice crystal nucleation rates and aggreagation processes on orographic snowfall. *J. Clim. Appl. Meteor.*, **25**, 1658–1680.

Covert, D. and J. Heintzenberg, 1993: Size distributions and chemical properties of aerosol at Ny Alesund, Svalbard. *Atmos. Environ.*, **27**, 2989–2977.

Curry, J., J. Pinto, T. Benner, and M. Tschudi, 1997: Evolution of the cloudy boundary layer during the autumnal freezing of the Beaufort Sea. *J. Geophys. Res.*, **102**, 13 851–13 860.

Curry, J., W. Rossow, D. Randall, and J. Schramm, 1996: Overview of Arctic cloud and radiation characteristics. *J. Climate*, **9**, 1731–1764.

Curry, J., et al., 2000: FIRE Arctic clouds experiment. *Bull. Am. Meteorol. Soc.*, **81**, 5–29.

Cziczo, D. and J. Abbatt, 1999: Deliquescence, efflorescence and supercooling of ammonium sulfate aerosols at low temperature: Implications for cirrus cloud formation and aerosol phase in the atmosphere. *J. Geophys. Res.*, **104**, 13 781–13 790.

Daniel, J., et al., 2006: Cloud property estimates from zerith spectral measurements of scattered sunlight between 0.9 and 1.7 μm. *J. Geophys. Res.*, **111**, D16 208.

de Boer, G., E. Eloranta, and M. Shupe, 2009a: Arctic mixed-phase stratiform cloud properties from multiple years of surface-based measurements at two high-latitude locations. *J. Atmos. Sci.*, **Accepted for publication**.

de Boer, G., T. Hashino, and G. J. Tripoli, 2009b: A theory for ice nucleation through immersion freezing in mixed-phase stratiform clouds. *Atmos. Res.*, **In Review**.

de Boer, G., G. J. Tripoli, and E. W. Eloranta, 2008: Preliminary comparison of CloudSAT-derived microphysical quantities with ground-based measurements for mixed-phase cloud research in the Arctic. *J. Geophys. Res.*, **113**, D00A06, 10.1029/2008JD010029.

Deirmendjian, A., 1969: *Electromagnetic scattering on spherical polydispersions*. Elsevier, Amsterdam.

Del Genio, A., M.-S. Yao, W. Kovari, and K.-W. Lo, 1996: A prognostic cloud water parameterization for global climate models. *J. Climate*, **9**, 270–304.

Diehl, K., M. Simmel, and S. Wurzler, 2006: Numerical sensitivity studies on the impact of aerosol properties and drop freezing modes on the glaciation, microphysics, and dynamics of clouds. *J. Geophys. Res.*, **111**, 10.1029/2005JD005884.

Diehl, K. and S. Wurzler, 2004: Heterogeneous drop freezing in the immersion mode: Model calculations considering soluble and insoluble particles in the drops. *J. Atmos. Sci.*, **61**, 2063–2072.

Donovan, D. and A. van Lammeren, 2001: Cloud effective particle size and water content profile retrievals using combined lidar and radar observations I – Theory and examples. *J. Geophys. Res.*, **105**, 27 425–27 488.

Eloranta, E., 2005: High spectral resolution lidar. *Lidar: Range-Resolved Optical Remote Sensing of the Atmosphere*, K. Weitkamp, Ed., Springer-Verlag, 143–163.

Engvall, A.-C., R. Krejci, J. Ström, A. Minikin, R. Treffeisen, A. Stohl, and A. Herber, 2008: In-situ airborne observations of the microphysical properties of the Arctic tropospheric aerosol during late spring and summer. *Tellus*, **60B**, 392–404.

Flatau, P., G. J. Tripoli, J. Verlinde, and W. Cotton, 1989: The CSU-RAMS cloud microphysics module: General theory and code documentation. Colorado State University.

Fridlind, A., A. Ackerman, G. McFarquhar, G. Zhang, M. Poellot, P. De Mott, A. Prenni, and A. Heymsfield, 2007: Ice properties of single-layer stratocumuls during the Mixed-Phase Arctic Cloud Experiment: 2. Model results. *J. Geophys. Res.*, **112**, D24 202.

Girard, E., J.-P. Blanchet, and Y. Dubois, 2005: Effects of Arctic sulphuric acid aerosols on wintertime low-level atmospheric ice crystals, humidity and temperature at Alert, Nunavut. *Atmos. Res.*, **73**, 131–148.

Hallett, J. and S. Mossop, 1974: Production of secondary ice particles during the riming process. *Nature*, **249**, 26–28.

Hara, K., S. Yamagata, T. Yamanouchi, K. Sato, A. Herber, Y. Iwasaka, M. Nagatani, and H. Nakata, 2003: Mixing states of individual aerosol particles in spring Arc-

tic troposphere during ASTAR 2000 campaign. *J. Geophys. Res.*, **108 (D7)**, DOI: 10.1029/2002JD002 513.

Harrington, J. and P. Olsson, 2001: On the potential influence of ice nuclei on surface-forced marine stratocumulus dynamics. *J. Geophys. Res.*, **106**, 27 473–27 484.

Harrington, J., T. Reisin, W. Cotton, and S. Kreidenweis, 1999: Cloud resolving simulations of arctic stratus part II: Transition season clouds. *Atmos. Res.*, **51**, 45–75.

Hashino, T. and G. Tripoli, 2007: The spectral ice habit prediction system (ships). part I: Model description and simulation of the vapor deposition process. *J. Atmos. Sci.*, **64**, 2210–2237.

Hegg, D., R. Ferek, and P. Hobbs, 1995: Cloud condensation nuclei over the Arctic Ocean in early spring. *J. Appl. Meteor.*, **34**, 2076–2082.

Heintzenberg, J., C. Leck, W. Birmili, M. Wehner, M. Tjernström, and A. Weidensohler, 2006: Aerosol number-size distributions during clear and fog periods in the summer high Arctic: 1991, 1996 and 2001. *Tellus*, **58B**, 41–50.

Herman, G. and R. Goody, 1976: Formation and persistence of summertime Arctic clouds. *J. Atmos. Sci.*, **33**, 1537–1553.

Hobbs, P., L. Radke, J. Locatelli, D. Atkinson, C. Robertson, R. Weiss, F. Turner, and R. Brown, 1972: Field observations and theoretical studies of clouds and precipitation over the Cascade Mountains and their modifications by artificial seeding (1971-1972). Tech. rep., The University of Washington.

Hoffer, T., 1961: A laboratory investigation of droplet freezing. *J. Meteor.*, **18**, 766–778.

Hogan, R., P. Francis, H. Flentje, A. Illingworth, M. Quante, and J. Pelon, 2003a: Charac-

teristics of mixed-phase clouds. I: Lidar, radar and aircraft observations from clare '98. *Quart. J. Roy. Meteor. Soc.*, **129**, 2089–2116.

Hogan, R., A. Illingworth, E. O'Connor, and J. Poiares-Baptista, 2003b: Characteristics of mixed-phase clouds, part II: A climatology from ground-based lidar. *Quart. J. Roy. Meteor. Soc.*, **129**, 2117–2134.

Hogan, R., M. Mittermaier, and A. Illingworth, 2006: The retrieval of ice water content from radar reflectivity factor and temperature and its use in evaluating a mesoscale model. *J. Appl. Meteor. Climatol.*, **45**, 301–317.

Holz, R., 2005: Remote sensing of arctic cloud top altitudes using high spectral resolution measurements. Ph.D. thesis, University of Wisconsin - Madison.

IPCC, 2007: Climate change 2007: The physical science basis. Tech. rep.

Jiang, H., W. Cotton, J. Pinto, J. Curry, and M. Weissbluth, 2000: Cloud resolving simulations of mixed-phase arctic stratus observed during base: Sensitivity to concentration of ice crystals and large-scale heat and moisture advection. *J. Atmos. Sci.*, **57**, 2105–2117.

Kay, J., T. LEcuyer, A. Gettelman, S. G., and C. O'Dell, 2008: The contribution of cloud and radiation anomolies to the 2007 Arctic sea ice extent minimum. *Geophys. Res. Lett.*, **35**, L08 503.

Khvorostyanov, V. and J. Curry, 2004: The theory of ice nucleation by heterogeneous freezing of deliquescent mixed ccn. part I: Critical radius, energy, and nucleation rate. *J. Atmos. Sci.*, **61**, 2676–2691.

Klein, S., et al., 2005: ARM cloud parameterization and modeling working group - GCSS Polar Cloud Working Group model intercomparison.

Klein, S., et al., 2009: Intercomparison of model simulations of mixed-phase clouds observed

during the ARM Mixed-Phase Arctic Cloud Experiement. part I: Single layer cloud. *Quart. J. Roy. Meteor. Soc.*, **Accepted for publication**.

Koch, D. and J. Hansen, 2005: Distant origins of Arctic black carbon: A Goddard Institute for Space Studies ModelE experiment. *J. Geophys. Res.*, **110 (D4)**, DOI: 10.1029/2004JD005 296.

Koop, T., N. H.P., L. Molina, and M. Molina, 1998: A new optical technique to study aerosol phase transitions: The nucleation of ice from H_2SO_4 aerosols. *J. Phys. Chem.*, **102**, 8924–8931.

Korolev, A. and G. Isaac, 2000: Drop growth due to high supersaturation caused by isobaric mixing. *J. Atmos. Sci.*, **57**, 1675–1685.

Korolev, A., G. Isaac, and J. Hallett, 1999: Ice particle habits in Arctic clouds. *Geophys. Res. Lett.*, **26**, 1299.

Leaitch, W., R. Hoff, S. Menlnichuk, and A. Hogan, 1984: Some physical and chemical properties of the Arctic winter aerosol in northeastern Canada. *J. Clim. Appl. Meteor.*, **23**, 916–928.

Liljegren, J., 1994: Two-channel microwave radiometer for observations of total column precipitable water vapor and cloud liquid water path. *Fifth Symposium on Global Change Studies*, American Meteorological Society, Nashville, TN, 262–269.

Liu, Y., J. Key, R. Frey, S. Ackerman, and W. Menzel, 2004: Night time polar cloud detection with MODIS. *Remote Sens. Environ.*, **92**, 181–194.

Low, T. and R. List, 1982: Collision, coalescence and breakup of raindrops. Part II: Parameterization of fragment size distributions. *J. Atmos. Sci.*, **39**, 1607–1619.

Luke, E. and P. Kollias, 2007: A high resolution hydrometeor phase classifier based on analysis of cloud radar doppler spectra. 6A.2 pp.

Matrosov, S., 1999: Retrievals of vertical profiles of ice cloud microphysics from radar and IR measurements using tuned regressions between reflectivity and cloud parameters. *J. Geophys. Res.*, **104**, 16 741–16 753.

Matrosov, S., A. Korolev, and A. Heymsfield, 2002: Profiling cloud mass and particle characteristic size from doppler radar measurements. *J. Atmos. Oceanic Technol.*, **19**, 1003–1018.

Matrosov, S., M. Shupe, A. Heymsfield, and P. Zuidema, 2003: Ice cloud optical thickness and extinction estimates from radar measurements. *J. Appl. Meteor.*, **42**, 1584–1597.

McFarquhar, G., G. Zhang, M. Poellot, G. Kok, R. McCoy, T. Tooman, A. Fridlind, and A. Heymsfield, 2007: Ice properties of single-layer stratocumulus during the Mixed-Phase Arctic Cloud Experiment: 1. Observations. *J. Geophys. Res.*, **112**.

Meyers, M., P. De Mott, and W. Cotton, 1992: New primary ice-nucleation parameterizations in an explicit cloud model. *J. Appl. Meteor.*, **31**, 708–721.

Mitchell, D., 1996: Use of mass- and area-dimensional power laws for determining precipitation particle terminal velocities. *J. Atmos. Sci.*, **53**, 1710–1723.

Morrison, H. and J. Pinto, 2005: Mesoscale modeling of springtime Arctic mixed-phase stratiform clouds using a new two-moment bulk microphysics scheme. *J. Atmos. Sci.*, **62**, 3683–3704.

Morrison, H., M. Shupe, and J. Curry, 2003: Modeling clouds observed at SHEBA using a bulk microphysics parameterization implemented into a single-column model. *J. Geophys. Res.*, **108**, D8.

Morrison, H. and P. Zuidema, 2008: GCSS/WMO Cloud Modeling Workshop Arctic mixed-phase stratus model intercomparison. 20 pp.

Morrison, H., et al., 2009: Intercomparison of model simulations of mixed-phase clouds observed during the ARM Mixed-Phase Arctic Cloud Experiment, Part II: Multi-layered cloud. *Quart. J. Roy. Meteor. Soc.*, **Accepted for publication**.

Mossop, S., R. Cottis, and B. Bartlett, 1972: Ice crystal concentrations in cumulus and stratocumulus clouds. *Quart. J. Roy. Meteor. Soc.*, **98**, 106–123.

Ose, T., 1993: An examination of the effects of explicit cloud water in the UCLA GCM. *J. Meteor. Soc. Japan*, **71**, 93–109.

Paluch, I. and D. Lenschow, 1991: Stratiform cloud formation in the marine boundary layer. *J. Atmos. Sci.*, **48**, 2141–2158.

Pielke, R., et al., 1992: A comprehensive meteorological modeling system - RAMS. *Meteorol. Atmos. Phys.*, **49**, 69–91.

Pinto, J., 1998: Autumnal mixed-phase cloudy boundary layers in the Arctic. *J. Atmos. Sci.*, **55**, 2016–2038.

Pobanz, B., J. Marwitz, and M. Politovich, 1994: Conditions associated with large-drop regions. *J. Appl. Meteor.*, **33**, 1366–1372.

Portman, R., S. Solomon, R. Sanders, J. Daniel, and E. Dutton, 2001: Cloud modulation of zenith sky oxygen photon path lengths over Boulder, Colorado: Measurements versus model. *J. Geophys. Res.*, **106**, 1139–1155.

Prenni, A., M. Wise, S. Brooks, and M. Tolbert, 2001: Ice nucleation in sulfuric acid and ammonium sulfate particles. *J. Geophys. Res.*, **106**, 3037–3044.

Prenni, A., et al., 2007: Can ice-nucleating aerosols affect Arctic seasonal climate? *Bull. Am. Meteorol. Soc.*, **88**, 541–550.

Pruppacher, H. and J. Klett, 1997: *Microphysics of Clouds and Precipitation*. 2d ed., Kluwer Academic Publishers, Boston.

Rangno, A. and P. Hobbs, 2001: Ice particles in stratiform clouds in the Arctic and possible mechanisms for the production of high ice concentrations. *J. Geophys. Res.*, **106**, 15 065–15 075.

Rasmussen, R., I. Geresdi, G. Thompson, K. Manning, and E. Karplus, 2002: Freezing drizzle formation in stably stratified layer clouds: The role of radiative cooling of cloud droplets, cloud condensation nuclei, and ice initiation. *J. Atmos. Sci.*, **59**, 837–860.

Rogers, D., P. De Mott, and S. Kreidenweis, 2001: Airborne measurements of tropospheric ice-nucleating aerosol particles in the Arctic spring. *J. Geophys. Res.*, **106**, 15 053–15 063.

Shupe, M., 2007: A ground-based multisensor cloud phase classifier. *Geophys. Res. Lett.*, **34**, L22 809.

Shupe, M. and J. Intrieri, 2004: Cloud radiative forcing of the Arctic surface: The influence of cloud properties, sufrace albedo, and solar zenith angle. *J. Climate*, **17**, 616–628.

Shupe, M., P. Kollias, P. Persson, and G. McFarquhar, 2008a: Vertical motions in Arctic mixed-phase stratiform clouds. *J. Atmos. Sci.*, **65**, 1304–1322.

Shupe, M., S. Matrosov, and T. Uttal, 2006: Arctic mixed-phase cloud properties derived from surface-based sensors at SHEBA. *J. Atmos. Sci.*, **63**, 697–711.

Shupe, M., T. Uttal, and S. Matrosov, 2005: Arctic cloud microphysics retrievals from surface-based remote sensors at SHEBAs. *J. Appl. Meteor.*, **44**, 1544–1562.

Shupe, M., et al., 2008b: A focus on mixed-phase clouds: The status of ground-based observational methods. *Bull. Am. Meteorol. Soc.*, **87**, 1549–1562.

Smith, R., 1990: A scheme for predicting layer clouds and their water content in a general circulation model. *Q.J.R.M.S*, **116**, 435–460.

Tiedtke, M., 1993: Representation of clouds in large-scale models. *Mon. Wea. Rev.*, **121**, 3040–3061.

Tripoli, G. J., 1992: A nonhydrostatic mesoscale model designed to simulate scale interaction. *Mon. Wea. Rev.*, **120**, 1342–1359.

Turner, D., 2005: Arctic mixed-phase cloud properties from AERI lidar observations: Algorithm and results from SHEBA. *J. Appl. Meteor.*, **44**, 427–444.

Turner, D., 2007: Improved ground-based liquid water path retrievals using a combined infrared and microwave approach. *J. Geophys. Res.*, **112**, D15 204.

Turner, D., S. Clough, J. Liljegren, E. Clothiaux, K. Cady-Pereira, and K. Gaustad, 2007: Retrieving liquid water path and precipitable water vapor from the Atmospheric Radiation Measurement (ARM) microwave radiometers. *IEEE Trans. Geosci. Remote Sens.*, **45**, 3680–3690.

Turner, D. and R. Holz, 2005: Retrieving cloud fraction in the field-of-view of a high-spectral-resolution infrared radiometer. *IEEE Geosci. Remote Sens. Lett.*, **3**, 287–291.

Uttal, T., et al., 2002: Surface heat budget of the Arctic Ocean. *Bull. Am. Meteorol. Soc.*, **83**, 255–275.

Verlinde, J., et al., 2007: The Mixed-Phase Arctic Cloud Experiment. *Bull. Am. Meteorol. Soc.*, **88**, 205–221.

Wang, Z. and K. Sassen, 2002: Cirrus cloud microphysical property retrieval using lidar and

radar measurements. Part I: Algorithm description and comparison with in situ data. *J. Appl. Meteor.*, **41**, 218–229.

Wang, Z., K. Sassen, D. Whiteman, and B. Demoz, 2004: Studying altocumulus with ice virga using ground-based active and passive remote sensors. *J. Appl. Meteor.*, **43**, 449–460.

Widener, K. and K. Johnson, 2005: Millimeter Cloud Radar (MMCR) handbook. (tr-018).

Yamanouchi, T., et al., 2005: Arctic Study of Tropospheric Aerosol and Radiation (ASTAR) 2000: Arctic haze case study. *Tellus*, **57 (2)**, 141–152.

Young, K., 1974: A numerical simulation of wintertime, orographic precipitation: Part I. Description of model microphysics and numerical techniques. *J. Atmos. Sci.*, **31**, 1735–1748.

Yum, S. and J. Hudson, 2001: Vertical distribution of cloud condensation nuclei spectra over the springtime Arctic Ocean. *J. Geophys. Res.*, **106**, 15 045–15 052.

Zhou, J., E. Swietlicki, O. Berg, P. Aalto, K. Hämeri, E. Nilsson, and C. Leck, 2001: Hygroscopic properties of aerosol particles over the central Arctic Ocean during summer. *J. Geophys. Res.*, **106**, 32 111–32 123.

Zuidema, P., et al., 2005: An Arctic springtime mixed-phase boundary layer observed during SHEBA. *J. Atmos. Sci.*, **62**, 160–176.